A NONHYDROSTATIC MODELING ANALYSIS OF AN INTENSE MIDLATITUDE SQUALL LINE

by

Ming-Jen Yang

A dissertation submitted in partial fulfillment
of the requirements for the degree of

Doctor of Philosophy

University of Washington

1995

Approved by_____
(Chairperson of Supervisory Committee)

Program Authorized
to Offer Degree_____

Date_____

UNIVERSITY OF WASHINGTON

Date: 18 August 1995

We have carefully read the dissertation entitled
A nonhydrostatic modeling analysis of an intense
midlatitude squall line
submitted by
Ming-Jen Yang
in partial fulfillment of
Ph.D.
the requirements of the degree of
and recommend its acceptance. In support of this recommendation we present the following
joint statement of evaluation to be filed with the dissertation.

The U.S. Weather Bureau's Thunderstorm Project report of 1949 showed that most thunderstorms consist of "cells," which are pairs of up- and downdrafts. The first part of this dissertation shows that the cells of a thunderstorm are a gravity wave phenomenon. This original study eliminates inconsistencies in previous explanations of the cellular behavior of thunderstorms. The gravity wave theory accounts fully for the patterns and movements of cells within a storm.

An important feature of a line of thunderstorms (a "squall line") is the inflow of dry air from middle levels of the atmosphere. Usually this inflow is in the form of a concentrated jet directed into the storm from its trailing side. This study shows that the rear inflow jet's structure and intensity is closely related to the evaporation of falling rain—in particular, the raindrops which result from the melting of ice particles. A storm with no ice does not produce a widespread rear inflow jet, nor does a storm in which the precipitating ice particles are mainly heavy, rapidly falling hailstones. Only if the precipitating ice particles are in the form of less dense, more slowly falling snow does the storm develop a broad rear inflow jet.

This study also clarifies the way in which a squall line of thunderstorms alters the momentum (i.e. wind) of the large-scale atmospheric region in which the squall line occurs. Calculations show that the momentum field is modified primarily by the air motions in the precipitating part of the cloud. The precipitating region of a squall line typically consists of a leading "convective" region and a trailing "stratiform" region. The calculations of this study show that the effects of the storm on the large-scale momentum are produced at lower levels in the convective region and at higher levels in the stratiform region.

DISSERTATION READING COMMITTEE:

Doctoral Dissertation

University of Washington

Abstract

A Nonhydrostatic Modeling Analysis of an Intense Midlatitude Squall Line

by Ming-Jen Yang

Chairperson of the Supervisory Committee: Professor Robert A. Houze, Jr.
Department of Atmospheric Sciences

Nonhydrostatic modeling shows that the convective cells of a squall line, which occurred over Kansas and Oklahoma on 10-11 June 1985, behaves as gravity waves. In the simulation, the gust front generates a continuous low-level updraft. Updraft cells periodically break away from the gust-front updraft and move at their associated gravity-wave phase speeds. Linear theory shows that waves are trapped in the troposphere because of the strong decrease of Scorer parameter with height. Linear theory predicts the gravity-wave amplitudes, quadrature relations, and the gravity-wave periods. The stronger front-to-rear propagation mode dominates in the mature stage of the storm. The decrease of Scorer parameter with height encountered by the rearward propagating waves is a product of the storm circulation. The drop-off in Scorer parameter with height is a manifestation of the shear between ascending front-to-rear and descending rear-to-front flows of the squall-line system. The squall line produces an environment conducive to trapping rearward propagating gravity waves generated at the gust front.

Numerical experiments show that the rear inflow and related aspects of storm structure are sensitive to hydrometeor types, ice-phase microphysics, and the midlevel environmental humidity. Ice-phase microphysics is important for the model to produce realistic air motions and precipitation in the stratiform region. With the occurrence of heavy hailstones, there is no enhanced rear-to-front flow at the back edge of the storm. Evaporation is the most important latent cooling process determining the structure and strength of the descending rear inflow and the mesoscale downdraft. Latent cooling by melting snow enhances the strength of the rear-to-front flow at the back edge of storm and the intensity of mesoscale downdraft. Mesoscale downdraft is initiated above the 0°C level by sublimational cooling. With the environmental midlevel moisture reduced by half, mesoscale downdrafts are stronger, but the rear-to-front flow at the back edge of the system is much weaker. The descending rear inflow is thus partly a dynamical response to the latent cooling processes in the trailing stratiform part of a squall line.

The momentum budget of the squall line is investigated. The intense pressure gradient associated with the mesolow in the convective region produces the ascending front-to-rear flow. Over a 300-km-wide large-scale area in which the storm is embedded, momentum balance is determined mainly by the airflows in precipitation regions (both convective and stratiform). Pressure-gradient force together with the vertical flux convergence by standing eddies determine most of the large-scale momentum tendency. The contribution from convective region dominates at low levels, both convective and stratiform regions contribute significantly to net momentum tendency at midlevels, and the contribution from stratiform region is essential at upper levels.

TABLE OF CONTENTS

LIST OF FIGURES

LIST OF TABLES

ACKNOWLEDGMENTS

DEDICATION

This work is deciated to

my wife,

Kuan-Mei Lu,
(1964 –   )

whose charm enlightens my life,

and

my son,

Eric Yang,
(1995 –   )

whose smile brings me love and hope.

CHAPTER 1

INTRODUCTION

1.1 Historical review of previous observational studies

Squall-line systems are perhaps the best documented class of mesoscale convective systems (MCSs), which are defined as cloud systems that occur in connection with an ensemble of thunderstorms and produce contiguous precipitation areas ~100 km or more in horizontal scale in at least one direction (Houze 1993, pp. 334–335). Squall lines occur over the continents and oceans, in both midlatitude and Tropics. They substantially affect local weather and global climate owing to their wide geographical range, frequent occurrence, and their associated heavy precipitation. In Kansas and Oklahoma of the United States, for example, the majority of major rain storms exhibit some degree of squall-line organization during some part of their lifetime (Houze et al. 1990).

A common type of squall line is a sharply defined leading-line convection with trailing stratiform precipitation (Fig. 1.1). Since this kind of squall line is so sharply defined, it is more amenable to study and has been examined intensively in a variety of ways. Thus, at the time of this writing, more can be said about its dynamics than is possible for other forms of MCSs. It appears that many aspects of leading-line/trailing stratiform organization can also apply to other types of mesoscale organization (Houze 1993, pp 349).

Hamilton and Archbold (1945) described "disturbance lines" over Africa, which appeared to be similar to the leading-line trailing-stratiform squall-line system of Fig. 1.1. Newton (1950) used upper-air data to document the vertical structure of a squall-line system that formed along a surface cold front but then later propagated out into the warm-air sector of the midlatitude cyclone.

Fujita (1955) documented the patterns of the surface pressure perturbations associated with mature squall-line systems. Ligda (1956) examined the low-level radar-reflectivity echoes associated with midlatitude squall lines and identified the multicellular structure of the convective region, the reflectivity minimum behind the convective region,

and the trailing region of more moderate precipitation. Pedgley (1962) proposed a three-stage lifecycle of mesoscale convective systems and provided detailed analysis of the surface, cloud, lightning, and radar-reflectivity structure of lines of thunderstorms over England. Newton (1963) investigated squall-line's storm-relative flow patterns, including the descending rear inflow at the back edge of the system. Ludlam (1963) noted the importance of low-level wind shear in organizing convection associated with squall lines.

Zipser (1969) documented the structure of the unsaturated mesoscale downdraft, and Zipser (1977) showed that the sounding through the trailing stratiform precipitation region exhibited an "onion" or "diamond" shape as a result of subsidence warming and drying associated with unsaturated mesoscale downdraft. Houze (1977) provided a detailed quantitative study of the radar-reflectivity characteristics of a tropical squall-line system and found that the stratiform area (with a well-defined bright band at the melting level) accounted for about 40% of the total rainfall from the squall-line system.

Ogura and Liou (1980) used upper-air data from a dense sounding network to examine the kinematic structure of a midlatitude squall line. In that study, Ogura and Liou (1980) provided one of the earliest estimates of the mesoscale updraft in the trailing stratiform region which earlier was only suggested by the presence of an extensive trailing precipitating stratiform cloud. Leary and Houze (1980) studied the contribution of mesoscale motions to the mass and heat fluxes of a tropical squall line. For tropical squall lines observed during the GARP (Global Atmospheric Research Program) Atlantic Tropical Experiment (GATE), Barnes and Sieckman (1984) found that fast-moving squall lines had more cross-line shear than slow-moving squall lines. Gamache and Houze (1982, 1985) and Houze and Rappaport (1984) confirmed the existence of the mesoscale updraft above the mesoscale downdraft in a similar type of study for a tropical squall line during GATE. Bluestein and Jain (1985) classified midlatitude squall lines into four categories based on their geometry and observed modes of development. The hodographs of the wind field accompanying intense squall lines exhibit considerable variability, but a strong component of shear across the squall lines in lower troposphere is very common.

With the advent of Doppler radars, it became possible to document the internal structure of squall-line systems with more details. Heymsfield and Schotz (1985)

performed a dual-Doppler analysis to study the kinematic structure of the early stage of a squall-line system that may have consisted of a line of supercell storms rather than the more commonly observed multicell storms. Srivastava et al. (1986) performed an extended velocity-azimuth display (EVAD) analysis to provide a good estimate of the mesoscale updraft and downdraft speeds in the trailing stratiform precipitation region of a midlatitude squall-line system. Smull and Houze (1985, 1987a) used a dual-Doppler network to study the kinematic structure of the squall-line system discussed by Ogura and Liou (1980) and found a correlation between the perturbations in front-to-rear flow in the convective region and the location of intense convective updrafts. Roux (1988) also studied the kinematic structure of a tropical squall-line system observed using a dual-Doppler network; he took the dual-Doppler wind fields and applied a thermodynamic retrieval to estimate the effects of momentum transport and heating from the convective system on the larger-scale environment where the storm was embedded.

1.2 Historical review of previous modeling studies

In the past two decades, the understanding of squall-line systems has been aided greatly by numerical modeling efforts. The quasi-two-dimensional nature of squall lines has inspired many attempts to simulate them by means of two-dimensional models, beginning with Takeda (1971), Hane (1973), and Schlesinger (1973), and continuing with the work of Thorpe et al. (1982), Yoshizaki (1986), Dudhia and Moncrieff (1987), Dudhia et al. (1987), Nicholls (1987), Rotunno et al. (1988), Nicholls et al. (1988), Weisman et al. (1988), Redelsperger and Lafore (1988), Lafore and Moncrieff (1989), Fovell and Ogura (1988, 1989), Tao and Simpson (1989), and many others. Any two-dimensional slab-symmetric simulation is, in effect, modeling an infinitely long line of convective clouds since by definition no gradients in any variables are allowed along the line. Rotunno et al. (1988) showed that in spite of the restrictive nature of two-dimensional simulations, the basic features are well reproduced in two-dimensional models and that the selective use of such two-dimensional models is justified. To investigate the along-line variability of squall lines, three-dimensional modeling is necessary (Skamarock et al. 1994).

Thorpe et al. (1982) investigated the effects of different vertical wind profiles in the pre-squall environment on the mesoscale organization of convective systems. They found that the storm could be long-lived if the low-level wind shear was sufficient to

force the position of the gust front to remain near the forward edge of the convective cells, so the convergence along the gust front occurred over a deep enough layer and a long enough time to initiate new convection on the downshear side of the parent thunderstorm. Rotunno et al. (1988) extended the original work of Thorpe et al. (1982) to explain the importance of the low-level shear on the longevity of the squall-line system. Rotunno et al. (1988) found that an optimal state, defined as the condition in which the air impinging on the nose of the cold pool exits vertically at the top of the cold pool, existed when the horizontal vorticity associated with the environmental low-level wind shear exactly balanced the horizontal vorticity generated by the buoyancy gradients across the nose of cold pool. Therefore, as the storm matured, the horizontal vorticity generated by the cold pool eventually overwhelmed the horizontal vorticity associated with environmental low-level shear and the convective updrafts tilted in the upshear direction.

1.3 Case to be investigated—the 10-11 June 1985 squall line in PRE-STORM

The case chosen for this dissertation study is the 10-11 June 1985 squall line, which represents the archetypal leading-line trailing-stratiform precipitation squall-line system (Houze et al. 1990). The Oklahoma-Kansas Preliminary Regional Experiment for Stormscale Operational Research Meteorology—Central Phase (PRE-STORM) was conducted during May and June of 1985 to study mesoscale convective systems (see Cunning 1986 for a review). During PRE-STORM, a special rawinsonde network was established with two pairs of Doppler radars located within the network; three wind profilers were also added to the rawinsonde network and automated surface stations were deployed over most of Oklahoma and Kansas with a spacing of just 50 km. One of the primary objectives of PRE-STORM was to determine the kinematic structure of mesoscale convective systems and to determine the interactions between the convective systems and the larger-scale environment in which they are embedded. Of several MCSs that were observed in PRE-STORM, the squall line that occurred on 10-11 June 1985 has been the most thoroughly studied (A total of 40–50 papers have been published based on studies on this particular case!)

Among several observational studies of the 10-11 June 1985 storm, Smull and Houze (1987b) used single Doppler-radar data and Augustine and Zipser (1987) used wind profiler data to identify the "rear-inflow jet" in this storm. Rutledge et al. (1988)

presented an overview of the radar-echo evolution and used single Doppler-radar data to document the vertical air motions in the stratiform region. Houze et al. (1989) presented a sample of the dual-Doppler analysis of the horizontal and vertical motions in the storm. Johnson and Hamilton (1988) analyzed sounding and surface mesonet data to study the "wake low" that occurred at the back edge of this storm. Johnson et al. (1990) used the sounding data to diagnose vertical air motion at upper levels in the trailing-stratiform cloud. Zhang et al. (1989) simulated the 10-11 June storm with a mesoscale numerical weather prediction model (MM4) and used several of the aforementioned studies for verification of simulation results. The verification with available observational analysis was encouraging. Zhang and Gao (1989) used their simulation results to discuss rear inflow, surface wake low, and stratiform precipitation. Tao et al. (1993) examined the heat, moisture, and water budgets of the 10-11 June squall line with special emphasis on the sensitivity to longwave radiation.

Biggerstaff and Houze (1991a) produced a comprehensive analysis of the kinematics and precipitation structure of the mature phase of the 10-11 June 1985 storm by combining a series of dual-Doppler analyses with high-frequency rawinsonde, wind profiler, and surface mesonet data in a time-space composite study. Biggerstaff and Houze (1991b) discussed the midlevel vorticity structure of the 10-11 June 1985 squall line, and Biggerstaff and Houze (1993) further investigated the kinematics and microphysics of the transition zone of the 10-11 June storm.

Gallus and Johnson (1991) used the sounding data to discuss the heat and moisture budget of the 10-11 June squall line, and Gallus and Johnson (1992) further used the sounding data to discuss the momentum budget of 10-11 June storm. Gallus and Johnson (1995a, b) developed a dynamic version of the two-dimensional kinematic cloud model of Rutledge and Houze (1987) to investigate the effects of microphysics on circulation within the stratiform region of the 10-11 June squall line.

Braun and Houze (1994a) performed a retrieval analysis to discuss the generation mechanism of the transition zone and secondary maximum of radar reflectivity in the stratiform region of the 10-11 June squall line. Braun and Houze (1995c) discussed the moisture and heat budgets and the implications for potential vorticity production of the 10-11 June storm. Braun (1995) further used the NCAR/Penn State mesoscale model (MM5) to investigate the processes involved in the storm's initiation (the interaction of

an upper-level short-wave trough, lee-side troughing, and a previous mesoscale system), the role of ice-phase microphysics in sharpening the upper-level trough, the formation of negative potential vorticity by the squall system and its advection downstream to strengthen the upper-level jet.

1.4 Objectives of the dissertation study

The organization of clouds and precipitation of the 10-11 June 1985 squall line resembles closely the conceptual model shown in Figure 1.1. Important features include a gust front, marking the leading edge of advancing rain-cooled air, a multicellular convective line in which air from near the surface ascends through the troposphere, a broad mesoscale ascent produced by condensation and deposition, and a broad mesoscale descent produced by the evaporation and melting of hydrometeors falling from the stratiform clouds. An ascending front-to-rear flow transports hydrometeors rearward from the leading convective line to the trailing-stratiform region. A descending rear-to-front flow, also referred to as the rear inflow, enters the storm from the back edge and slopes downward toward the front of the squall line. A radar bright band is seen near the freezing level in the stratiform precipitation region.

One objective of this dissertation study is to investigate the multicellular structure during the mature phase of the 10-11 June squall line. To achieve this goal, high-resolution nonhydrostatic simulations of the 10-11 June squall line in both two and three dimensions are conducted. Chapter 2 discusses the multicellular structure of the 10-11 June storm from the viewpoint of gravity-wave dynamics, and a linear gravity-wave theory is present to explain the multicellular structure seen in the nonlinear simulation.

A descending rear inflow is an interesting flow feature that has been investigated by many studies (Smull and Houze 1987b; Fovell and Ogura 1989; Zhang and Gao 1989; Lafore and Moncrieff 1989; and many others). The rear-inflow jet is shown to play an important role in the evolution of long-lived squall-line system (Weisman 1992). Chapter 3 discusses the sensitivity of squall-line rear inflow and other related storm structure to hydrometeor types, ice-phase microphysics, and environmental humidity.

The organized deep convection in a squall-line MCS can have a substantial impact on the surrounding large-scale environment in which the squall line is embedded. Chapter 4 investigates the momentum budget of the 10-11 June squall line and discusses

the interaction between the squall-type MCS and its large-scale environment. In particular, Chapter 4 seeks to distinguish the roles played by the convective and stratiform regions of the storm in the overall momentum budget.
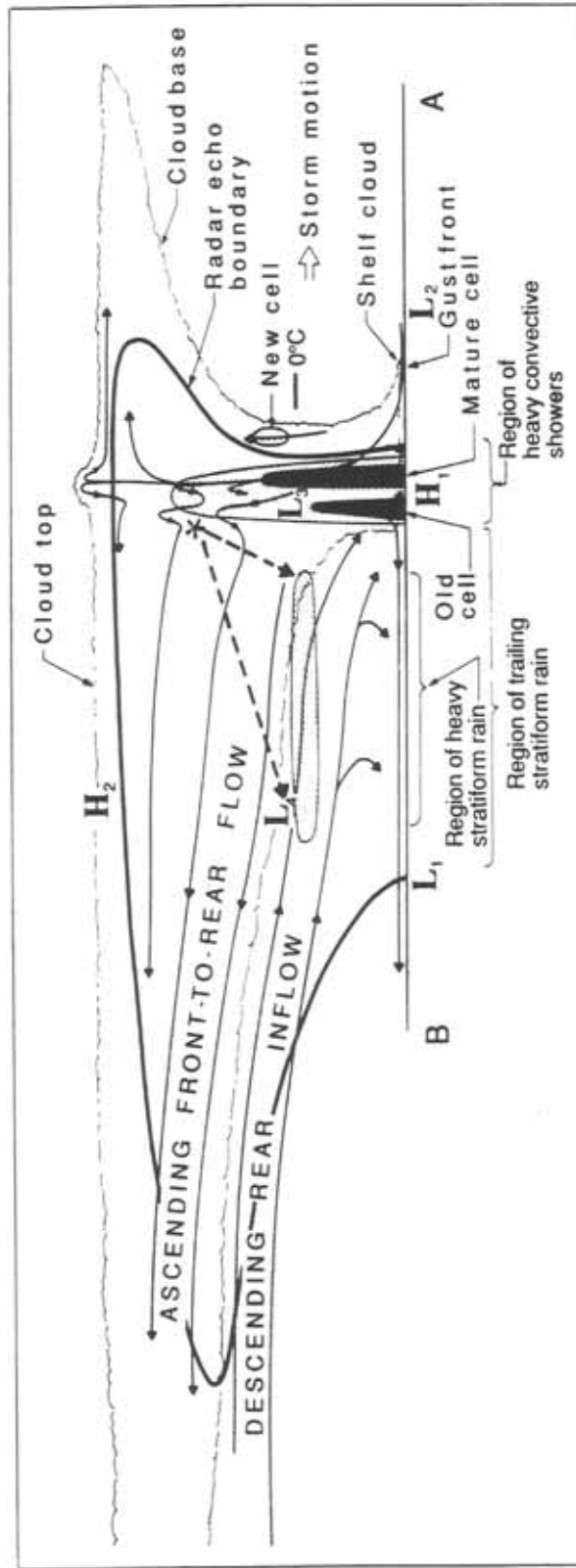
Fig. 1.1 Conceptual model of the kinematic, microphysical, and radar–echo structure of a convective line with trailing stratiform precipitation viewed in a vertical cross section oriented perpendicular to the convective line (and generally parallel to its motion). Intermediate and strong radar reflectivity is indicated by median and dark shading (from Houze et al. 1989).

CHAPTER 2

MULTICELLULAR STRUCTURE

2.1 Traditional understanding of multicells

The fundamental building block of thunderstorms is the "cell" (Byers and Braham 1949), which is characterized by a compact region of relatively strong vertical velocity and intense precipitation. In general, there are two kinds of cells—ordinary cells and supercells, and the majority of convective storms are composed of ordinary cells (Browning 1977; Weisman and Klemp 1984). Convective storms often consist of several ordinary cells at different stages of evolution. Byers and Braham (1949) identified three stages in the evolution of an ordinary cell: the cumulus stage (updraft alone), the mature stage (updraft and downdraft), and the dissipating stage (downdraft alone). The mature stage of a typical cell lasts ~15–30 min before giving way to the dissipating stage.

A multicell storm often has cells forming on a preferred side with each individual cell moving roughly parallel to the mean midtropospheric wind vector. The storm thus propagates discretely toward either the right or the left of the mean wind vector (Browning 1962; Marwitz 1972; Newton and Fankhauser 1975). Figure 2.1 shows a vertical cross section for a Colorado multicell hailstorm based on radar and aircraft data as synthesized by Browning et al. (1976). This vertical cross section, taken along the storm's direction of motion, shows a sequence of four ordinary cells (n-2, n-1, n, n+1) at different stages of evolution. Each cell goes through a similar life cycle, with new cells developing on the storm's forward flank (right side of figure) and old cells decaying on the rear flank (left side of figure). This schematic model can be interpreted in two ways: as an instantaneous view of a typical multicell storm with four cells at different stages of evolution, or as four stages in the evolution of an individual cell. The time interval between development of successive cells was ~15 min. The lifetime of each cell was less than 60 min.

Ordinary multicell storms are often characterized by the successive formation of "discrete" new cells; each cell is essentially independent from those previously existing (Marwitz 1972; Browning 1977; Wilhelmson and Chen 1982). However, Foote and Frank (1983) described another mode of multicell storm based on a triple-Doppler radar analysis. The individual cells in this storm (the middle panels in Fig. 2.2) were neither fully

independent to be considered as those in a classic multicell storm (the left panels in Fig. 2.2), nor sufficiently steady to be considered as a supercell (the right panels in Fig. 2.2). Foote and Frank (1983) called this behavior "weak evolution" in contrast with the classic or "strong evolution" multicell model, because the appearance of a cell's updraft is considered to be a small perturbation on an established, persistent updraft.

A squall line is a long-lived line of convective cells. It consists of laterally aligned cells which tend not to interfere disruptively with one another by competing for the same warm, moist environmental air. Individual cells within a squall line may be all ordinary cells, a mixture of ordinary cells and supercells, or all supercells. A vertical cross section taken perpendicular to the squall line often shows a series of convective cells at different stages of their evolution as shown in Fig. 2.1.

Fovell and Ogura (1988) investigated the multicellular structure of the 22 May 1976 Oklahoma squall line with a two-dimensional (2D) nonhydrostatic numerical model. Their simulated multicell storm reached a "quasi-equilibrium" state characterized by periodic production of new cells at the leading edge of the storm. Individual cells moved rearward relative to the gust front as they aged, transporting hydrometeors in their updrafts into the trailing portion of the storm. The multicellular behavior of the squall line was interpreted in terms of the new cells cutting off the moisture supply of the older cells. Fovell and Dailey (1995) further examined the temporal behavior of simulated 2D mature multicell-type storm through the experiments that varied the depth of vertical wind-shear layer. Their simulated storms oscillated in time with respect to updraft intensity and the generation of condensation and surface rainfall.

The objective of Chapter 2 is to discuss the multicellular structure of the 10-11 June 1985 PRE-STORM squall line from the viewpoint of *gravity-wave dynamics*. Most of Chapter 2 is based on Yang and Houze (1995a). The 10-11 June squall line has been investigated in several observational studies (e.g., Smull and Houze 1987b; Rutledge et al. 1988; Johnson and Hamilton 1988; Gallus and Johnson 1991; Biggerstaff and Houze 1991a and b; Gallus and Johnson 1992; Biggerstaff and Houze 1993; Braun and Houze 1994a, b, 1995a, b) and numerical studies (Zhang et al. 1989; Zhang and Gao 1989; Gao et al. 1990; Tao et al. 1993; Gallus and Johnson 1995a, b). None of these previous studies examined the gravity-wave structure excited by convection of the squall-line system, which is the theme of Chapter 2. 2D simulation results of the 10-11 June 1985 squall line with a

high-resolution nonhydrostatic cloud model will be analyzed in Section 2.3. A three-dimensional (3D) simulation will be presented in Section 2.4 to confirm the results found in the 2D simulation. A linear theory will be given in Section 2.5 and the results of linear theory will be discussed in Section 2.6 to explain how the multicellular structure of the squall line may be explained in terms of gravity waves generated at the gust front and trapped within the troposphere. Finally, Section 2.7 summarizes the main findings in Chapter 2.

2.2 Numerical model and initial conditions

2.2.1 Numerical model

The numerical model used in this dissertation study is the Klemp and Wilhelmson (1978) compressible nonhydrostatic cloud model, as modified by Wilhelmson and Chen (1982). Both 2D and 3D versions of the model are used. The x-coordinate is the cross-line direction and the y-coordinate is the along-line direction. The basic-state environment is assumed constant in time and horizontally homogeneous; large-scale variation, Coriolis force, surface drag, and radiation effects are neglected.

For the 2D simulation, the grid is stretched in both vertical (z) and cross-line (x) directions, in order to optimize the grid resolution. There are 62 grid points in the vertical; the model top is at 21.7 km, and the grid size (Δz) of the lowest layer is 140 m, while the grid size of the highest layer is 550 m. A rigid lid is used at the top and bottom of the domain. The implementation of horizontally stretched grids is similar to that of Fovell and Ogura (1988). The model uses 455 grid points in the horizontal, the central 315 of which comprise a fine mesh with a constant grid size of 1 km. A 2250-km-wide stretch grid is put on both sides of the fine mesh; the ratio between adjacent grid spacings is 1.075:1. The total horizontal domain size (fine mesh and stretched grids) is thus 4814 km. An "open" boundary condition described by Klemp and Wilhelmson (1978) with phase speed $c* = 30$ m s^{-1} is used to reduce the numerical reflection at the lateral boundaries. During the course of the simulation, the model domain translates with the storm so that the simulated storm is always within the fine mesh. A time-splitting scheme is used to provide numerical efficiency by treating the sound wave mode (2 s time step) and the gravity wave mode (6 s time step) separately (see Klemp and Wilhelmson 1978 for details).

2.2.2 Cloud microphysics

Microphysical bulk parameterization in the model is based on Lin et al. (1983). Five types of water condensate are included: cloud water, cloud ice, rainwater, snow, and hail. In the Lin et al. (1983) microphysical scheme, a hailstone is defined as a hail particle with a diameter of 5 mm or more, a density of 0.8 and 0.9 g cm^{-3}, and a fall speed between 10 and 40 m s^{-1} or more. The sensitivity of storm structure to the hydrometeor type (with and without hail stones) will be discussed in Section 3.3.1. The cloud droplets and ice crystals are assumed to be monodispersed and to have no appreciable fall speeds compared to air vertical velocity. The precipitating particles (rainwater, snow, and hail) are assumed to have exponential size distributions. Following Potter (1991), the density of water is used for snow's slope parameter (λ) of its size distribution function. Following Braun and Houze (1994a), no density correction factor is applied to the fall speed of snow. They note that there is no experimental evidence to support the inclusion of the density correction factor for the fall speed of snow, and they found that with the density factor included one obtains unreasonably large fall speeds at upper levels.

2.2.3 Initial conditions

The smoothed initial temperature and dew point profiles for the simulation are taken from the 2331 UTC 10 June 1985 sounding of Enid (END), Oklahoma (Fig. 2.3a). This sounding was taken at a location in the path of the bowed part of the 10–11 June squall line (Fig. 2.4), which passed this station 4 hours later. The 10-11 June squall line formed over western Kansas, where there was no sounding. The Enid sounding was far enough ahead of the squall line to be unaffected by the existing convection, yet not too far away to be completely unrepresentative of the initial environmental conditions. Extra moisture was added to the Enid sounding in the low levels in order to favor convection. Without the extra low-level moisture, the simulated storm died 2 hours after its initiation. This enhanced low-level moisture profile was based on the 2330 UTC 10 June 1985 sounding of Pratt, Kansas (the PTT station in Fig. 2.4). The convective available potential energy (CAPE, Moncrieff and Miller 1976; Weisman and Klemp 1982) calculated from this moisture-enhanced sounding is 3323 J kg^{-1}, which is higher than the average value of 2820 J kg^{-1} for springtime broken-line type squall lines in this region (Bluestein and Jain 1985).

Figure 2.3b shows the vertical profile of the smoothed initial wind components. The bulk Richardson number (Weisman and Klemp 1982; Bluestein and Jain 1985) calculated from the moisture-enhanced sounding and observed wind fields (including both the cross-line and along-line components) is 46.9, which is in the range of multicell storms (Weisman and Klemp 1982). A 5-km deep, 170-km long cold pool of $\Delta \theta' = -6\,°K$ and $\Delta q_v' = -4\,g\,kg^{-1}$ (in Fig. 2.5) was placed in the domain to initiate convection. This initial cold pool, which was prescribed as a negative potential temperature and moisture perturbation, was set to mimic the background cold air in the synoptic environment (Johnson and Hamilton 1988) and the cold air outflow by previous convection (Braun 1995). The characteristics of the cold pool were determined from the analysis of surface mesonetwork data (see Fig. 5 of Johnson and Hamilton 1988).

2.3 Two-dimensional simulation results

For the simulated 2D storm, the initial cold pool generates a convective cell, which leans downshear (ahead of the moving line) with height owing to the strong ambient wind shear. The development of convection follows a pattern similar to that described by Rotunno et al. (1988). By $t = 30$ min, a substantial burst of rainfall reaches the ground and the anvil outflow is mostly in the downshear direction. A sequence of cells, which develop along the leading edge of the cold pool, continue to lean downshear with height through 2 h. At $t = 2$ h, the updraft cells are vertically oriented, with anvil outflows more evenly distributed in the upshear and downshear directions. After $t = 2$ h, the simulated storm leans increasingly upshear (rearward) with height and cell redevelopment continues to occur at the leading edge as the precipitation-induced cold pool intensifies its strength. After $t = 5$ h, the width of the surface precipitation region increases with time and the cell production proceeds in a regular, periodic manner.

2.3.1 Mesoscale storm structure

After $t = 8$ h, the simulated 2D squall line reaches its mature stage and shows a qualitatively realistic structure when compared with observations. Figure 2.6a is the time sequence of surface rainfall rate during a one-hour period ($t = 10-11$ h) in the mature stage. It shows the continuous generation of intense precipitation cells at the leading edge and much weaker precipitation in the trailing stratiform region. Figure 2.6b displays the one-hour time-average surface rainfall rate, which shows the heavy precipitation in the

convective region (from $x = 20$ to 50 km), followed by weak rainfall in the transition zone (from $x = 0$ to 20 km) and a secondary rainfall maximum in the stratiform region (from $x = -90$ to 0 km). This surface rainfall rate field is in good agreement with the low-level radar reflectivity field (see Fig. 6 of Biggerstaff and Houze 1991a). Note that the gust front is fixed near $x = 50$ km.

Figures 2.7a and 2.8a depict time-averaged model output fields in the fine mesh during the same one-hour period ($t = 10$–11 h) at the mature stage. Time averaging is applied to each field over this one-hour period at a 2-min data interval, similar to Fovell and Ogura (1988). Thus convective-scale, transient wave-like perturbations are smoothed out, and only more steady mesoscale signatures are left. All fields are displayed in a coordinate translating at the gust-front propagation speed (12.2 m s^{-1} during the mature stage).

Figure 2.7a shows the storm-relative horizontal wind field (storm speed is determined as the gust-front propagation speed), which exhibits front-to-rear (FTR; negative) flows in mid-to-upper levels within the storm ($x = -90$ to 50 km) and in lower levels at the back edge of the storm ($x = -90$ to -60 km), and the rear-to-front (RTF; positive) flows in between. The RTF flow enters the system the rear as the rear inflow, and it penetrates downward and across the storm into the convective region ($x = 20$ to 50 km). The time-averaged model winds of the simulated 2D storm agree well with the along-line averaged wind field in Fig. 2.7b based on the dual-Doppler radar composite analysis of Biggerstaff and Houze (1993), although the simulated FTR jet is stronger than the "observed" one as a result of the exaggerated horizontal divergence by the restricted 2D geometry (Nicholls and Weissbluth 1988; Weisman 1992, personal communication). The length in the along-line direction included in the average of the observations is 60 km, which covers four to six convective cells, roughly the same number of precipitation cells included in the time average (see Fig. 2.6a) for the simulated 2D storm.

Figure 2.8a is the vertical velocity field of the simulated 2D storm, which shows an intense low-level updraft maximum, another one at midlevels in the convective region ($x = 20$ to 50 km), and much broader but weaker mesoscale updrafts and downdrafts in the stratiform region ($x = -90$ to 0 km). A downdraft also occurs in the upper levels in the transition zone ($x = 0$ to 20 km) in Fig. 2.8a, although it is too weak to show up with the 0.5 m s^{-1} contour interval. These features agree well with the along-line averaged vertical velocity field in Fig. 2.8b from the dual-Doppler radar composite analysis (Biggerstaff and

Houze 1993). In particular, the model successfully simulates the downward slope of mesoscale downdrafts toward the convective region. The simulation shows that the mesoscale updrafts are ahead (to the right) of the mesoscale downdrafts in the stratiform precipitation region ($x = -90$ to 0 km). This structure is also consistent with the radar composite analysis (Fig. 2.8b). The low-level updraft maximum at the gust front does not show up well in the radar composite analysis because the divergence in the boundary layer was not sampled well by radar as a result of beam geometry, the earth's curvature, and refraction of the radar beam by the ground.

2.3.2 Transient convective structure

The realistic structure of the time-averaged simulation results (Figs. 2.7a and 2.8a), when compared with the dual-Doppler radar composite analysis (Figs. 2.7b and 2.8b), gives us confidence to analyze the model results in more detail. The time averaging required to make the comparisons, however, smears out convective-scale phenomenon, which cannot be resolved by the dual-Doppler radar composite analysis but can be simulated with the high-resolution cloud model. These convective-scale, transient features are evident in instantaneous model outputs at $t = 11$ h (Figs. 2.9–2.12). The vertical velocity with the hatched rainwater field and shaded snow field in Fig. 2.9 displays the typical structure of a multicell storm, *i.e.*, a sequence of convective cells at different stages of their evolution. However, when the vertical velocity field is superimposed on other fields (like pressure perturbation p' in Fig. 2.10, storm-relative horizontal wind $u\text{-}c$ in Fig. 2.11, or potential temperature perturbation θ' in Fig. 2.12), a new interpretation of the multicellular structure can be obtained—*convective cells in a multicell storm are associated with gravity waves.*

In Fig. 2.10, low pressure perturbations p' (defined as the deviations from the initial value; indicated by letter L's) are located one quarter of a wavelength behind (to the left of) the updrafts (indicated by the heavy shading) at low levels ($z < 3.5$ km), but the minima p' are located one quarter of a wavelength ahead (to the right) of the updrafts in upper levels (7 km $< z <$ 13 km). This phase relationship can be seen clearly for the updraft located at $x = 13$ to 23 km. Although the heights of updraft centers for these convective cells (in Fig. 2.9) are different, their phase relationships with p' fields (Fig. 2.10) are the same. Above the tropopause ($z > 14$ km), however, low pressure perturbations are collocated with the downdrafts (indicated by the light shading). The 90°

phase shift between the p' and w fields in the lower troposphere creates a strong front-to-rear pressure gradient, that forces air parcels near the gust front to move rearward (see the low pressure p' centered at $z = 2.5$ km, $x = 45$ km in Fig. 2.10). Similarly in Fig. 2.11, the horizontal-wind maxima u (indicated by letter M's) are seen to be one quarter of a wavelength behind (to the left of) the updrafts in low levels ($z < 3$ km), but u-maxima are one quarter of a wavelength ahead (to the right) of updrafts in upper levels (7 km $< z < 13$ km). The updraft located at $x = 13$ to 23 km again shows the phase relationships between the w and u fields very clearly. The u-maxima are collocated with the downdrafts above the tropopause ($z > 14$ km). In Fig. 2.12, the maximum potential temperature perturbations θ' (defined as the deviation from the initial value; indicated by letter W's) are one quarter of a wavelength behind (to the left of) the updrafts in all levels, and this phase shift is more pronounced above the tropopause ($z > 14$ km). The distinct phase relationships among the w, p', u, and θ' fields indicate that the multicellular structure is possibly a gravity-wave phenomenon.

A similar phase relationship between w and u fields can also be found in the analysis of "nearly instantaneous" Doppler-derived wind fields for the 10-11 June 1985 squall line in Fig. 2.13. Figure 2.13a covers the rear part of the convective region and the trailing stratiform region with a clear "bright band" in the radar reflectivity field. Figure 2.13b shows that low-level horizontal-wind maxima at $x = 12$ km and $x = 48$ km are located with the updrafts to the right and downdrafts to the left (Fig. 2.13c), which is similar to the low-level configuration between simulated w and u fields displayed in Fig. 2.11.

Disturbances above the tropopause ($z > 14$ km) in Figs. 2.10–2.12 show a typical structure of vertically propagating gravity waves [cf. Fig. 4.1 of Durran (1990) or Fig. 6.6 of Gill (1982)]. For the rearward-moving mode (behind the gust front; $x < 50$ km), w is in phase with p', out of phase with u', and 90° ahead of θ' (w-maximum is ahead of θ'-maximum by one quarter of a wavelength). For the forward-moving mode (ahead of the gust front; $x > 50$ km), w is in phase with both u' and p', and 90° behind θ' (w-maxima is rearward of θ'-maximum by one quarter of a wavelength), although their amplitudes are too weak to show up for the contour intervals used in Figs. 2.10–2.12. The gravity waves above the tropopause are mechanically triggered by convective cells constantly impinging upon the tropopause (Fovell et al. 1992; Alexander et al. 1995).

2.3.3 Gravity-wave interpretation

Figure 2.14 is a time sequence of the vertical velocity field of the 2D simulation, which shows that the low-level convective updraft at the gust front ($x = 50$ km) is a persistent feature of the simulated mature-phase squall line. The occurrence of a persistent low-level updraft at the gust front is also found by Fovell and Ogura (1989) in their simulated Oklahoma multicell storm. Convective cells behind the low-level gust-front cell, on the other hand, are transient wave features. A new "gravity-wave" updraft G_1 first occurs near $x = 40$ km at $t = 644$ min. It forms by breaking away from the top of the low-level gust-front updraft, because of the strong front-to-rear pressure gradient associated with the $90°$ phase shift between the p' and w fields in low levels (see the low pressure at $x = 45$ km in Fig. 2.10). Once the convective cell is separated from the persistent gust-front updraft, it propagates rearward at its associated gravity-wave phase speed (to be shown in Figs. 2.15–2.16). The next gravity-wave updraft G_2 appears at the same location ($x = 40$ km) at $t = 656$ min, and the cycle repeats. The fact that the location of a new convective cell relative to the gust front is the same as for the old convective cell is also documented by Sanders and Emanuel (1977) for an Oklahoma squall line and by Fovell and Ogura (1988) for their simulated multicell storm. The period for the regeneration of gravity-wave updrafts is 12–14 min, which is the same as the generation period of precipitation cells in the surface rainfall rate field (Fig. 2.6a).

This behavior of the simulated multicell squall line provides a new dynamical interpretation of the multicellular structure of thunderstorms and squall lines. The traditional multicell model would suggest that the spreading cold outflow of an old cell enhances convergence, which then triggers the formation of a new cell. Once a new cell forms at the leading edge of the gust front, the supply of moisture and warm air to the older cell is cut off, causing it to dissipate (Wilhelmson and Chen 1982; Droegemeier and Wilhelmson 1985; Fovell and Ogura 1988). New cells thus form at the leading edge of the gust front in a "discrete" manner, according to this classic view of multicell storms (Chalon et al. 1976; Browning 1977). However, the time sequence of vertical velocity in Fig. 2.14 demonstrates that the gust-front updraft is a persistent feature, not a discrete or pulsating feature as implied by the classic multicell model; convective cells behind the gust front form by regularly breaking away from the top of a steady low-level gust-front updraft. The persistence or quasi-steadiness of the gust-front updraft cell fits the "weak evolution" characterization (middle panels in Fig. 2.2) of a multicell storm by Foote and Frank (1983),

in which convective cells were small perturbations upon a persistent, established updraft, although the Foote and Frank mode is a highly three-dimensional entity.

The animation of model outputs thus shows that *the so called "cut-off" process is actually a gravity-wave phenomenon which has not been shown before.* The gust front and its associated low-level convergence produce a nearly steady low-level, very intense updraft. As this updraft moves through the ambient stratified flow, it generates gravity waves as a result of release of latent heat. The updrafts of the gravity waves have a different propagation velocity than the gust-front updraft. A gravity-wave updraft therefore periodically breaks off from the top of the gust-front updraft and moves rearward through the storm as a discrete "cell". The "cut-off" process associated with the multicellular storm is thus seen to be not a discrete mechanism described by the traditional multicell model but rather a continuous process of wave generation by the persistent gust front.

The convective-cell trajectories in Fig. 2.15a are determined by tracking the motion of updraft centers from model output at 2-min intervals during a one-hour period ($t = 10$–11 h). The convective cells are identified when their associated updrafts have a closed vertical-velocity contour during this one-hour period. Cells 1–6 in Fig. 2.15a do not begin and end at the same time. The corresponding air-parcel trajectories in Fig. 2.15b, starting from the same points as the convective updraft-center trajectories in Fig. 2.15a, are computed by the method of Doty and Perkey (1993) from model wind fields at the same data resolution (2 min). The air-parcel trajectories in Fig. 2.15b begin and end at the same time as the convective-cell trajectories in Fig. 2.15a. All trajectories are displayed with respect to a storm-relative coordinate where the gust front is fixed at $x = 50$ km. The equivalent potential temperatures (θ_e) along the air-parcel trajectories are found to be conserved except in the highly transient convective region ($x = 20$ to 50 km). The maximum difference of θ_e along the trajectories is less than 2 K in the strong time-variant convective region. Thus, the air-parcel trajectory calculations are believed to be computed to a satisfactory degree of accuracy.

Comparison of the convective-updraft trajectories and their corresponding air-parcel trajectories shows that *the updraft cells move at velocities significantly different from the airflow in their near surroundings.* In the precipitation region ($x < 50$ km in Fig. 2.15) of the simulated mature-phase squall line, the convective updraft cells always propagate rearward relative to the gust front, regardless of the direction of the airflow in their near

environments. For example, convective-cell trajectory 4 in Fig. 2.15a moves rearward (to the left of figure). However, the corresponding air-parcel trajectory 4, starting from the same point in Fig. 2.15b, moves forward (to the right of figure) as part of the RTF airflow (see Figs. 2.7a and 2.11). Similarly, convective-cell trajectories 1 and 3 in Fig. 2.15a move rearward, but their corresponding air-parcel trajectories 1 and 3 in Fig. 2.15b change to move forward at later times. Although the air-parcel trajectories all start from the same points as the convective-cell trajectories, none of them end at the same point. Therefore, updraft cells that break away from the top of the low-level gust-front updraft do not move at mean airflow speeds as implied by the traditional multicell model (Browning 1977; Weisman and Klemp 1986).

Figure 2.16 shows the x-t plot of the w field at a height $z = 5.25$ km for the time period $t = 10$–11 h. This time-space plot of the vertical velocity field shows that the convective updraft cells are associated with gravity waves, which are initially forced at the leading edge of the storm ($x = 50$ km), and then propagate toward both sides of the leading edge but with a much stronger front-to-rear mode. The dominant front-to-rear propagation of gravity waves is the result of the persistent upshear tilt of leading-edge updrafts at the mature stage (Fovell et al. 1992; Alexander et al. 1995), when the cold pool intensifies and baroclinic vorticity generation at the leading edge of the cold pool dominates over the ambient horizontal vorticity in the low-level wind shear (Rotunno et al. 1988). The phase speeds of these gravity waves can be determined by the slopes of the constant phase lines (heavy solid lines) in Fig. 2.16. The steep slopes of the constant phase lines in the convective region ($x = 20$ to 50 km) imply slower phase speeds (storm-relative phase speeds are $c = -20$ to -25 m s^{-1}), and the flatter slopes of the constant phase lines in the stratiform region ($x < 20$ km) indicate faster phase speeds (storm-relative phase speeds are $c = -30$ to -40 m s^{-1}), as shown by the updraft-cell trajectories in Fig. 2.15a (like trajectories 5, 6). Chalon et al. (1976) in their analysis of observed radar echoes for a Colorado multicell hailstorm also found that convective cells moved slowly in their early stages and moved faster at their later stages. Therefore, it is clear from Figs. 2.15a and 2.16 that updraft cells move rearward with respect to the gust front at their associated gravity-wave phase speeds, not at surrounding airflow speeds.

Figure 2.17 is the z-t plot of the w field at $x = 18$ km (32 km behind the gust front) during the same time period. This height-time plot clearly shows that above the tropopause ($z > 14$ km), constant phase lines tilt horizontally, which is a property of a vertically

propagating gravity wave; below the tropopause ($z < 14$ km), constant phase lines are oriented vertically with no obvious horizontal tilt, which is a characteristic of evanescent or trapped waves. Thus the reversed quadrature relationship (90° phase shift) of the w and p' (or u) fields between the lower and upper troposphere (see Figs. 2.10–2.11) indicates a gravity wave structure different from those above the tropopause: *vertically trapped gravity waves*.

2.4   Three-dimensional simulation results

A 3D simulation was conducted to confirm the multicellular structure and gravity-wave phenomenon found in the 2D simulation. The domain size of the 3D simulation is 240 km × 60 km × 21.7 km, in x-, y-, and z-directions, respectively. The horizontal grid size is constant ($\Delta x = \Delta y = 2$ km) and vertical grids are stretched with finer resolution at low levels (31 points in the vertical; smallest $\Delta z = 199$ m, largest $\Delta z = 1201$ m). The coarse resolution in the 3D simulation, when compared with that of the 2D simulation ($\Delta x = 1$ km; smallest $\Delta z = 140$ m, largest $\Delta z = 550$ m), is due to the constraint of computer memory and CPU. An open boundary condition is used in the cross-line (x) direction, and a periodic condition is used in the along-line (y) direction. Convection is also initiated by a cold pool as shown in Fig. 2.5 with a maximum strength of $\Delta \theta' = -10$ °K and $\Delta q'_v = -6$ g kg^{-1} (the stronger cold pool is required for the coarser resolution in the 3D simulation). Small (< 0.5 K) random temperature perturbations were superimposed on the initial line cold pool. Ice-phase microphysics is included. All other conditions are the same as in the 2D case.

The 3D counterpart to the 2D storm develops in much the same way, except that with the extra degree of freedom, the storm evolves quickly into a line of three-dimensional cells. Figs. 2.18–2.20 show the 3D simulation result at $t = 5$ h, when the simulated squall line is in its developing stage. In Fig. 2.18a, the rainwater mixing ratio is contoured and shown with the storm-relative wind vector field (storm motion is again determined from the gust-front propagation speed, 7.22 m s^{-1} at $t = 5$ h). Three precipitation cells are associated with three strong convective updraft cells, each accompanied by weak downdrafts (in Fig. 2.18b). Some weak updrafts/downdrafts (magnitudes < 1 m s^{-1}) occurred both behind and ahead of the gust front, as in the 2D case (Fig. 2.9).

Figure 2.19 shows the w and p' fields at a low level ($z = 0.7$ km), while Fig. 2.20 shows the corresponding fields at an upper level ($z = 11.9$ km). At the low level (Fig. 2.19), three high-low couplets (H_1/L_1, H_2/L_2, and H_3/L_3) shown in insets A, B, and C are associated with three strong convective updraft cells (Fig. 2.18b) or three precipitation cells (Fig. 2.18a) just behind the gust front. High pressures are ahead of the updrafts with low pressures behind the updrafts. A similar phase relationship can be seen for other high-low couplets (H_4/L_4, H_5/L_5, and H_6/L_6) behind the gust front. The reverse quadrature relationship (high pressures are behind updrafts with low pressures ahead of updrafts) occurs in relation to updrafts ahead of the gust front (see H_7/L_7 and H_8/L_8). These low-level phase relationships are the same as those shown in the 2D simulation (Fig. 2.10). At the upper level (Fig. 2.20), the quadrature relationships between w and p' fields are opposite to those at the low level (Fig. 2.19), which is again the property of vertically trapped gravity waves (see Fig. 2.10). In Fig. 2.20, high pressures (like H_9, H_{10}, H_{11}, and H_{12}) are behind the updrafts, and low pressures (like L_9, L_{10}, L_{11}, and L_{12}) are ahead of the updrafts for updrafts behind the gust front; the reverse quadrature (see H_{13}/L_{13}) again occurs to updrafts ahead of the gust front.

The quadrature relationship between w and u fields in the 3D simulation (not shown) is also similar to that seen in the 2D simulation. Therefore, we conclude that, although different in details, there is no *essential* difference between the 2D and 3D simulations of the 10-11 June squall-line system for the multicellular structure and gravity-wave phenomenon.

2.5 Linear theory presentation of model gravity waves

In this section, we use the linear gravity-wave theory to explain the multicellular structure seen in the nonlinear numerical simulation. Since the 3D results in Section 2.4 show that the gravity-wave signatures are well represented in the 2D framework, the linear theory is also 2D in order to simplify the discussion. Following Bretherton (1966) and Durran (1989), the inviscid linear governing equations for a 2D internal gravity wave in a nonrotating flow in which a basic state only varies with height are

$$(\frac{\partial}{\partial t} + \overline{U}\frac{\partial}{\partial x})u' + w'\frac{d\overline{U}}{dz} = -c_p\overline{\theta}\frac{\partial \pi'}{\partial x} \tag{2.1}$$

$$\left(\frac{\partial}{\partial t}+\overline{U}\frac{\partial}{\partial x}\right)w'=-c_p\overline{\theta}\frac{\partial \pi'}{\partial z}+g\frac{\theta'}{\overline{\theta}} \tag{2.2}$$

$$\left(\frac{\partial}{\partial t}+\overline{U}\frac{\partial}{\partial x}\right)\theta'+\frac{\overline{\theta}}{g}N^2 w'=Q \tag{2.3}$$

$$\frac{c_v}{R\overline{\pi}}\left(\frac{\partial}{\partial t}+\overline{U}\frac{\partial}{\partial x}\right)\pi'+\left(\frac{\partial u'}{\partial x}+\frac{\partial w'}{\partial z}\right)-\frac{g}{c_s^2}w'=0 \tag{2.4}$$

where

$$N^2=\frac{g}{\overline{\theta}}\frac{d\overline{\theta}}{dz}, \quad c_s^2=\frac{c_p}{c_v}R_d\overline{T}=\gamma R_d\overline{T}, \quad \pi=\left(\frac{p}{p_o}\right)^{R_d/c_p} \tag{2.5}$$

Dependent variables in (2.1)–(2.4) are zonal wind u, vertical velocity w, nondimensional pressure π, potential temperature θ, where t is time, x is east-west coordinate, z is height, g is the magnitude of gravitational acceleration, N is the Brunt-Väisälä (buoyancy) frequency, c_p is the specific heat at constant pressure, c_v is the specific heat at constant volume, R_d is the gas constant for dry air, T is temperature, p_o is a constant reference pressure (1000 mb), and Q is the latent heating produced by convection. The basic-state variables $\overline{\rho}, \overline{\theta}$, $\overline{U}$, and $\overline{\pi}$ are functions of height (z); perturbations are denoted by primes; $u=\overline{U}+u'$, $w=w'$, $\pi=\overline{\pi}+\pi'$, $\theta=\overline{\theta}+\theta'$, and c_s is the basic-state sound speed.

In order to simplify the algebra, it is useful to remove the effect of the decrease in density with height by defining new variables (Bretherton 1966; Durran 1989):

$$\tilde{u}=\left(\frac{\overline{\rho}}{\rho_o}\right)^{1/2}u', \qquad \tilde{w}=\left(\frac{\overline{\rho}}{\rho_o}\right)^{1/2}w',$$

$$\tilde{\pi}=\left(\frac{\overline{\rho}}{\rho_o}\right)^{1/2}c_p\overline{\theta}\pi', \quad \tilde{\theta}=\left(\frac{\overline{\rho}}{\rho_o}\right)^{1/2}\frac{g}{\overline{\theta}}\theta', \quad \tilde{Q}=\left(\frac{\overline{\rho}}{\rho_o}\right)^{1/2}\frac{g}{\overline{\theta}}Q \tag{2.6}$$

where ρ_o is a constant reference density (surface density). In terms of these new variables, the governing equations become

$$\left(\frac{\partial}{\partial t}+\overline{U}\frac{\partial}{\partial x}\right)\tilde{u}+\tilde{w}\frac{d\overline{U}}{dz}=-\frac{\partial\tilde{\pi}}{\partial x} \tag{2.7}$$

$$\left(\frac{\partial}{\partial t}+\overline{U}\frac{\partial}{\partial x}\right)\tilde{w}=-\frac{\partial\tilde{\pi}}{\partial z}+\tilde{\theta}-\Gamma\tilde{\pi} \tag{2.8}$$

$$\left(\frac{\partial}{\partial t}+\overline{U}\frac{\partial}{\partial x}\right)\tilde{\theta}+N^2\tilde{w}=\tilde{Q} \tag{2.9}$$

$$\frac{1}{c_s{}^2}\left(\frac{\partial}{\partial t}+\overline{U}\frac{\partial}{\partial x}\right)\tilde{\pi}+\frac{\partial\tilde{u}}{\partial x}+\frac{\partial\tilde{w}}{\partial z}-\Gamma\tilde{w}=0 \tag{2.10}$$

where

$$\Gamma=-\frac{1}{2\overline{\rho}}\frac{d\overline{\rho}}{dz}-\frac{1}{\overline{\theta}}\frac{d\overline{\theta}}{dz}=\frac{1}{2\overline{\rho}}\frac{d\overline{\rho}}{dz}+\frac{g}{c_s{}^2} \tag{2.11}$$

Consider the case of an anelastic system only, *i.e.*, $c_s \rightarrow \infty$. Then the continuity equation (2.10) can be written in a simpler form,

$$\frac{\partial\tilde{u}}{\partial x}+\frac{\partial\tilde{w}}{\partial z}-\Gamma\tilde{w}=0 \tag{2.12}$$

Note that under the anelastic approximation (Wilhelmson and Ogura 1972), $\Gamma\approx-\frac{1}{2\overline{\rho}}\frac{d\overline{\rho}}{dz}$, and the continuity equation (2.12) can be rewritten in the traditional form for the anelastic continuity equation,

$$\frac{\partial}{\partial x}(\overline{\rho}u')+\frac{\partial}{\partial z}(\overline{\rho}w')=0$$

After some algebraic manipulation of (2.7)–(2.9) with the aid of (2.12) (see Appendix for a detailed derivation), we obtain a single equation for $\tilde{w}$,

$$\left(\frac{\partial}{\partial t}+\overline{U}\frac{\partial}{\partial x}\right)^2\left(\frac{\partial^2\tilde{w}}{\partial x^2}+\frac{\partial^2\tilde{w}}{\partial z^2}\right)-\frac{d^2\overline{U}}{dz^2}\left(\frac{\partial}{\partial t}+\overline{U}\frac{\partial}{\partial x}\right)\frac{\partial\tilde{w}}{\partial x}$$

$$-\left(\Gamma^2+\frac{d\Gamma}{dz}\right)\left(\frac{\partial}{\partial t}+\overline{U}\frac{\partial}{\partial x}\right)^2\tilde{w}-2\Gamma\frac{d\overline{U}}{dz}\left(\frac{\partial}{\partial t}+\overline{U}\frac{\partial}{\partial x}\right)\frac{\partial\tilde{w}}{\partial x}+N^2\frac{\partial^2\tilde{w}}{\partial x^2}-\frac{\partial^2\tilde{Q}}{\partial x^2}=0 \tag{2.13}$$

Note that some simplified versions of equation (2.13) have been used for the discussion of internal gravity waves (Scorer 1949; Sawyer 1960; Bretherton 1966; Durran 1990). Since $\overline{U}$, N^2, and Γ are functions of height, we can assume solutions for equation (2.13) of the form,

$$\tilde{w} = \text{Re}\left\{W(z)e^{ik(x-ct)}\right\}, \quad \tilde{Q} = \text{Re}\left\{H(z)e^{ik(x-ct)}\right\} \tag{2.14}$$

where Re means the real part of a complex variable, k is the wavenumber, and c is the phase speed. In (2.14), we assume that latent heating $\tilde{Q}$ is horizontally in phase with $\tilde{w}$, which is generally true for deep convection. Substitution of (2.14) into (2.13) leads to the so-called Taylor-Goldstein equation (with the inclusion of heating) which determines the vertical structure of W,

$$\frac{d^2W}{dz^2} + (\ell^2 - k^2)W = \frac{H}{(\overline{U} - c)^2} \tag{2.15}$$

where

$$\ell^2 = \frac{N^2}{(\overline{U} - c)^2} - \frac{d^2\overline{U}/dz^2 + 2\Gamma d\overline{U}/dz}{\overline{U} - c} - \frac{d\Gamma}{dz} - \Gamma^2 \tag{2.16}$$

ℓ^2 is called the Scorer parameter (Scorer 1949). Boundary conditions for (2.15) are assumed to be

$$W = 0, \quad z = 0 \tag{2.17}$$

$$\frac{dW}{dz} = -iMW, \quad z = z_T \tag{2.18}$$

where

$$M = \sqrt{\ell^2 - k^2} \quad \text{at } z = z_T \tag{2.19}$$

z_T is the top of the domain. Upper boundary condition (2.18) is a "radiation condition," that allows energy to propagate upward through the top of the domain (Lindzen 1974) without reflection.

Ground-relative wind $\overline{U}(z)$ in Fig. 2.21a, $N^2(z)$ in Fig. 2.21b, and Scorer parameter $\ell^2(z)$ in Fig. 2.21c are determined from the horizontally averaged profiles of a 70-km-wide region of the leading portion of the simulated 2D squall line at time $t = 11$ h ($x = -20$ to 50 km in Figs. 2.9–2.12). Storm-relative wind can be obtained by subtracting the storm propagation speed (12.2 m s^{-1}) from the ground-relative wind. Ground-relative phase speed $c = -20$ m s^{-1} (storm-relative phase speed is -32 m s^{-1}) is determined from a time-lapse display of model results with a data resolution of 2 min. Local horizontal wavenumber k is determined from the cell separation distance. For the region of $x = 10$ to 26 km in Figs. 2.9–2.12, k is found to be $-2\pi / (16 \text{ km})$. A negative wavenumber means FTR-moving waves. The smoothed latent-heating profile $H(z)$ (the average heating over half a wavelength) in Fig. 2.21d is determined from numerical model output at $t = 11$ h for that region ($x = 10$–26 km). For given k, c, $\Gamma(z)$, $\overline{U}(z)$, $N^2(z)$, and $H(z)$ we can use the method of Lindzen and Kuo (1969) to solve equation (2.15) for $W(z)$ numerically. Note that $W(z)$ is a complex variable because of the radiation condition (2.18). Therefore, from (2.14), $\tilde{Q}$ can be expressed in the form

$$\tilde{Q} = H \cos(kx - kct) \tag{2.20}$$

Then $\tilde{w}$ can be written in the form

$$\tilde{w} = \text{Re}W \cos(kx - kct) - \text{Im}W \sin(kx - kct) \tag{2.21}$$

where the real part (Re) and the imaginary part (Im) of $W(z)$ are determined from equations (2.15), (2.17), and (2.18). Hence, $\tilde{u}$ can be determined by substituting (2.21) into the continuity equation (2.12),

$$\begin{aligned}
\tilde{u} = &\frac{1}{k}\left[\Gamma \, \text{Re}W - \frac{d}{dz}(\text{Re}W) \right] \sin(kx - kct) \\
&+ \frac{1}{k}\left[\Gamma \, \text{Im}W - \frac{d}{dz}(\text{Im}W) \right] \cos(kx - kct)
\end{aligned} \tag{2.22}$$

$\tilde{\pi}$ can be determined by substituting (2.21) and (2.22) into the u-momentum equation (2.7),

$$\tilde{\pi} = -\frac{1}{k}\left[(\overline{U}-c)(\Gamma\,\mathrm{Re}W - \frac{d}{dz}\mathrm{Re}W) + \frac{d\overline{U}}{dz}\mathrm{Re}W\right]\sin(kx-kct)$$

$$+\frac{1}{k}\left[(c-\overline{U})(\Gamma\,\mathrm{Im}W - \frac{d}{dz}\mathrm{Im}W) - \frac{d\overline{U}}{dz}\mathrm{Im}W\right]\cos(kx-kct) \qquad (2.23)$$

and $\tilde{\theta}$ can be determined by substituting (2.20) and (2.21) into the thermodynamic equation (2.9).

$$\tilde{\theta} = \frac{H-N^2\mathrm{Re}W}{k(\overline{U}-c)}\sin(kx-kct) + \frac{-N^2\mathrm{Im}W}{k(\overline{U}-c)}\cos(kx-kct) \qquad (2.24)$$

2.6 Discussion

2.6.1 Linear theory result

Figure 2.22a shows the w and p' perturbation fields predicted by the linear theory for the region of $x = 10$–26 km at time $t = 11$ h, and Fig. 2.22b is the corresponding 2D numerical simulation result. Linear theory predicts the right strength ($\sim$7.9 m s^{-1}) of the updraft at the right level ($\sim$7.3 km), when compared with nonlinear numerical model output (Fig. 2.22b). Linear theory captures the strong vertical tilt of the phase line in the lower stratosphere (the tilt angle of the phase line from the vertical is 60.6° in Fig. 2.22a versus 72° in Fig. 2.22b). Linear theory shows that low pressure perturbations are to the left of the updrafts at low levels (for low pressures p' at $x = 13$–15 km, $z < 7$ km) and to the right of the updrafts at upper levels (for low pressures p' at $x = 21$–23 km, 7 km $< z <$ 14 km), which are also seen in the nonlinear numerical model result. Thus the phase relationship between the p' and w fields is well predicted by linear theory. The amplitude of pressure perturbation p' is somewhat underpredicted at low levels (predicted $p' = -4.3$ mb versus simulated $p' = -5.1$ mb for the low centered at $z = 3$ km, $x = 13$ km) and slightly overpredicted at upper levels (predicted $p' = 1.2$ mb versus simulated $p' = 1.0$ mb for the high centered at $z = 13$ km, $x = 13$ km). However, these discrepancies are minor. The results demonstrate that the multicellular structure is basically controlled by linear gravity-wave dynamics.

Figure 2.23a displays the w and u fields predicted by the linear theory for the same region at $t = 11$ h, and Fig. 2.23b is the corresponding numerical model result. Again, linear theory predicts the phase relationship between the w and u field very well. The amplitude of the u-maximum is underpredicted at low levels (predicted $u = 9.5$ m s^{-1} versus simulated $u = 12.9$ m s^{-1} for the maximum centered at $z = 1.7$ km, $x = 13$ km), and slightly underpredicted at upper levels (predicted $u = 15.2$ m s^{-1} versus simulated $u = 17.2$ m s^{-1} for the maximum centered at $z = 14$ km, $x = 23$ km).

In general, the predicted gravity-wave perturbations of w, u, and p' by linear theory are in somewhat better agreement with the numerical simulation results in the lower stratosphere ($z > 14$ km) than in the troposphere ($z < 14$ km), where nonlinear effects and turbulent mixing are more likely to be important. Nevertheless, the success of linear theory in portraying the cell structure seen in the nonlinear numerical simulation lends confidence to the dynamical explanation of the multicellular structure as a gravity-wave phenomenon.

2.6.2 Characteristics of trapped waves in the simulated squall line

At the leading-convective portion of the simulated squall line, the dominant horizontal wavelengths are $\lambda = 16$ to 20 km and storm-relative phase speeds are $c = -20$ to -25 m s^{-1}, so the main gravity wave periods in this region are $T = \lambda/c = 10.7\text{-}16.7$ min, which are the same as the generation periods of precipitation cells (11–17 min) at the mature stage (see Fig. 2.6a). Similar horizontal wavelengths (determined as cell separation distances) were also found by Dudhia et al. (1987) for their two-dimensional simulations of a long-lived west African squall line, although their cellular development periods were much longer. In the trailing stratiform region, the gravity waves become more diffuse with weaker amplitudes, and their wavelengths become longer ($\lambda = 25\text{-}35$ km) with increasing phase speeds (storm-relative phase speeds are $c = -30$ to -40 m s^{-1}). We can use the dispersion relationship to explain why gravity waves in the stratiform region have longer wavelengths than in the convective region. The horizontal phase-speed c_x and group velocity c_{gx} for 2D internal gravity waves with a constant mean flow $\bar{u}$ are,

$$c_x = \bar{u} \pm \frac{N}{\sqrt{k^2 + m^2}}$$

$$c_{gx} = \bar{u} \pm \frac{Nm^2}{(k^2 + m^2)^{3/2}}$$

where m is the vertical wavenumber [equation (7.44) of Holton 1992]. For areas behind the squall-line gust front, waves propagate westward relative to the mean flow, so we choose minus sign. The increase of phase speed c_x with increasing horizontal wavelength (decreasing horizontal wavenumber k) is a characteristic of the dispersive internal gravity waves. The reason why the wavelengths of gravity waves differ between the convective and stratiform regions is probably because of the difference of group velocity. To be specific, since $\bar{u}$ is usually negative behind the gust front, c_{gx} becomes more negative for smaller k (longer horizontal wavelength). That is, the group velocity for the long wave is faster than that of the short wave. Then some time after the initiation of waves near the gust front, wave packets associated with long waves would travel farther away from the gust front than those of short waves. Therefore, gravity waves in the stratiform region (farther away from the gust front) have longer horizontal wavelength than those in the convective region (close to the gust front).

The multicellular squall line shows a nice wave train of updraft cells and the significant quadrature relationship between w and p' (u, or θ') fields. The amplitudes of convective cells are well predicted by the linear gravity-wave theory. The generation periods of these convective cells are the same as the gravity-wave periods. It is clear from these three facts that the convective cells behind the gust front are very likely to be transient gravity-wave features.

For a mature squall line, the generation of gravity waves and their associated convective cells by the forced lifting of warm air over the cold pool may be similar to the generation of gravity waves by the forced lifting of air over a mountain. Once buoyancy oscillations are triggered at the leading edge of the cold pool, they are further modulated by the latent heating associated with convective cells. The constant rearward propagation of convective cells within the storm is due to the westward (FTR) phase speeds of their associated gravity waves.

The quadrature relationship (90° phase shift) between w and p' (or u) fields in low levels can also be seen in the simulated Oklahoma squall line on 22 May 1976 by Fovell and Ogura (1988; see their Figs. 8 and 10). Fovell and Ogura (1989) further investigated the effects of low-level wind shear on the simulated mature-phase multicell storms. They defined a "quasi-equilibrium" state as the repetitive multicellular development, and the "quasi-equilibrium" state was achieved for a very wide range of wind shear intensities.

The average period between successive cellular development in their study was relatively constant (17 min), which suggested the existence of a "fundamental oscillation" common to the simulated multicell storms. This relatively constant period of cellular development might be the wave period of the trapped gravity waves in their simulated storms.

2.6.3 Trapping mechanisms

According to equation (2.15), the vertical structure of the gravity waves depends on the relative magnitude of the Scorer Parameter (ℓ^2) and the horizontal wavenumber. If $\ell^2 > k^2$, then the wave oscillates in z with vertical wave number $\sqrt{\ell^2 - k^2}$, i.e., it is a vertically propagating wave. If $\ell^2 < k^2$, then the solution decays with height (since the solution must be bounded), i.e., it is an evanescent or trapped wave.

Trapping of gravity waves in the troposphere is not a result of the strong static stability in the lower stratosphere. This point can be demonstrated in Fig. 2.24a, which shows the linear theory result when the stratosphere is removed by using a constant tropospheric value of $N = 1.1 \times 10^{-2}$ s^{-1} for $z \geq 10$ km. In this case, waves still show the typical trapped-wave phase relationships between w and p' fields in the troposphere (see w and p' fields in Fig. 2.10). The reason for the waves to be trapped in the mid-to-upper levels (6 km $< z <$ 13 km) is the strong decrease of Scorer parameter (ℓ^2) with height, analogous to trapped lee waves (Durran 1990). Recalling the definition of the Scorer parameter in (2.16), it can be seen from Figs. 2.21a–c that the decrease of Scorer parameter with height in mid-to-upper levels (6 km $< z <$ 13 km) results from both an increase of wind speed ($\overline{U} - c$) and a decrease of static stability (N) with height. Curvature of mean flow and other effects indicated in the definition of the Scorer parameter contribute very little to the trapping mechanism in the mid-to-upper levels.

Waves are also trapped in low levels (0 $< z <$ 6 km). This low-level trapping mechanism is further investigated in Fig. 2.24b, in which the rigid-lid ground is replaced by an open radiation condition at the lower boundary condition but using the same Scorer parameter profile in Fig. 2.21c. Instead of being trapped, waves in low levels in Fig. 2.24b show a downward-propagating structure. Note that in the low level ($z <$ 4.5 km), waves show an opposite phase relationship between w and p' fields (constant phase line tilts rearward with decreasing height; w is out of phase with p') compared to waves in the lower stratosphere (constant phase line tilts rearward with increasing height; w is in phase

with p'). This opposite phase relationship with the upward propagating waves in the stratosphere ($z > 14$ km) indicates that waves in the lower levels ($z < 4.5$ km) for the open lower-boundary case propagate downward. Therefore, the downward-propagating waves destructively interfere with upward-propagating waves reflected from the ground so that there is no vertical tilt of the phase line. Thus, waves are trapped in low levels ($0 < z < 6$ km) because of the rigid ground.

The trapping mechanism determined from the vertical profile of the Scorer parameter also applies to the internal gravity waves within the oceanic thermocline (Lighthill 1978). The role of the Scorer parameter $\ell^2(z)$ in determining the waves' vertical structure for the atmospheric internal gravity waves is similar to that of $N^2(z)$ for the oceanic internal gravity waves. Lighthill (1978) indicated that oceanic internal gravity waves might be trapped within the thermocline region when $N^2(z)$ had a substantial vertical gradient (see his Figure 74), which was similar to the vertical profile of Scorer parameter in Fig. 2.21c.

Since the vertical variation of $N^2(z)$ in the troposphere ($z < 14$ km) is not as strong as that of $\overline{U}(z)$ (see Figs. 2.21a–b), the Scorer parameter is strongly dependent on $\overline{U}(z)$. The strong peak of the Scorer parameter is due to the reverse vertical shear of $\overline{U}(z)$, as a result of RTF flows in upper and lower levels and FTR flows at midlevels. Initially, trapped gravity waves only occur in a narrow area near the convective region. The reverse wind shear associated with RTF and FTR jets is more evident as the storm becomes well developed and mature, and the vertical peak of the Scorer parameter is also more pronounced with a wider trapped gravity-wave area. *The evolution of the Scorer parameter is thus a feedback interaction between gravity waves and the storm in which they are embedded.* The integral effect of the convective cells (by their associated pressure perturbations) determines the mean wind profile in the cells' surrounding environment, while the Scorer parameter implied by the mean wind profile determines the vertical characteristics of the convective cells' gravity waves—vertically propagating or trapped.

2.6.4 Other trapped waves associated with convection

Kuettner et al. (1987) found internal gravity waves in the free troposphere above a convectively active planetary boundary layer. These waves, commonly referred to as "convection waves," usually occur in a synoptic condition that favors active convection in

the boundary layer and considerable vertical wind shear ($> 3 \times 10^{-3}$ s^{-1}) through the lower to middle troposphere. These convection waves are excited when the shallow convection in the presence of shear penetrates into the stable layer above the convective boundary layer. To some extent, the mechanism is similar to the orographic forcing of gravity waves. From the analysis of aircraft data, Kuettner et al. (1987) found that the convection waves had wavelengths of 5–15 km, vertical wind amplitudes of ± 1–3 m s^{-1}, and a vertical extension of at least 9 km.

Gage et al. (1989) documented the observation of convection waves measured by a VHF wind-profiling Doppler radar on 29 June 1985 during the PRE-STORM project. These convection waves were formed as a result of strong surface heating and considerable vertical wind shear above the boundary layer. An analysis of the wave event indicated that these convection waves were trapped in the troposphere owing to the influence of background wind shear.

Hauf (1993) reported aircraft observations of convection waves over southern Germany. The convection waves were forced by shallow moist convection penetrating into an overlaying shear layer centered around the boundary-layer top, and were trapped in midtropospheric levels by a layer of reduced stability aloft. The same trapped-wave phase relationships between w, p', and θ' as those shown in Figs. 2.9–2.12 are displayed in his Fig. 7. The measurements showed that convection waves represented a typical fluid-dynamical mode of a daytime troposphere, and they existed in a vertically propagating mode and a trapped mode.

The "convection waves" of Kuettner et al. (1987), Gage et al. (1989), and Hauf (1993) are forced by shallow convection penetrating into an overlying shear layer. The gravity waves in this study are of larger amplitudes ($\Delta w = \pm 2$–10 m s^{-1}) and have longer wavelengths ($\lambda = 16$–20 km). However, the trapping mechanisms for these gravity waves are similar; that is, they are both trapped in the midtroposphere because of strong vertical wind shear and reduced stability aloft.

2.6.5 Wave generation and maintenance mechanisms

Powers (1994) discussed several wave generation mechanisms for mesoscale gravity waves: convective instability, shear instability, and geostrophic adjustment. Although the gravity waves in our cloud model simulation are of smaller convective scale

(λ = 10–50 km), compared to a much longer mesoscale scale (λ = 50–350 km) studied by Powers, similar wave generation and maintenance mechanisms may be also operating in convective-scale gravity waves within the squall-line system.

Convective instability occurs when static stability (N^2) is reduced. Figure 2.25 shows the calculated square of Brunt-Väisälä frequency N^2 at $t = 11$ h for the 2D storm. In the calculation, $N^2 = N_d^2$ for RH (relative humidity) < 100%, and $N^2 = N_m^2$ for RH $\geq$ 100%, where N_d^2 is the square of *dry* Brunt-Väisälä frequency given in (2.5) and N_m^2 is the square of *moist* Brunt-Väisälä frequency determined from equation (36) of Durran and Klemp (1982). It is clear from Fig. 2.25 that for a substantial portion of the region of upward air motion, air is saturated (RH $\geq$ 100%), so the environment in this region is unstable for gravity-wave oscillations (hatched area for $N^2 < 0$). On the other hand, within most of the cold pool and the stratosphere ($z > 14$ km), the environment is very stable for gravity wave propagation (shaded area for high static stability). Therefore, convective instability plays a significant role in the generation of these simulated gravity waves (Figs. 2.9–2.12).

Figure 2.26 shows the Richardson number at $t = 11$ h for the simulated 2D storm. In the calculation, Richardson number R_i is defined as follows,

$$R_i = \begin{cases} R_{id} & , \text{ RH} < 100\% \\ R_{im} & , \text{ RH} \geq 100\% \end{cases}$$

where

$$R_{id} = \frac{N_d^2}{(\frac{\partial u}{\partial z})^2} , \quad R_{im} = \frac{N_m^2}{(\frac{\partial u}{\partial z})^2}$$

In Fig. 2.26, Richardson number is in the range of $0.25 < R_i < 1.0$ within the convective updrafts (since $N_m^2 < 0$), along the top of cold pool (strong shear between the ascending front-to-rear flow aloft and descending rear-to-front flow below), and near cloud top (strong wind shear across the cloud top). Thus, shear instability could be also one of the wave generation mechanisms. It is possible that waves of Kelvin-Helmholtz variety induced by shear instability may occur (when $R_i < 0.25$). However, the resolution is not

fine enough to determine if the simulated gravity waves are associated with Kelvin-Helmholtz waves.

Since the Coriolis force is not included in the simulation and our simulated gravity waves are of convective scale (λ = 10–50 km), we discard the possibility that geostrophic adjustment contributes to wave generation.

The next question is: once waves are generated, how do they maintain themselves to propagate horizontally for long distances. According to Powers (1994), wave-CISK (Conditional Instability of the Second Kind; see Lindzen 1974) and ducting (Lindzen and Tung 1976) are two possible wave maintenance mechanisms for the mesoscale gravity waves he investigated. Thus, we would like to examine these two mechanisms in our simulated convective-scale gravity waves.

Wave-CISK is a mechanism in which latent heat released in convection is capable of forcing the waves which in turn serve to organize the convection. This mechanism usually occurs in a situation when the entire depth of the troposphere is conditionally unstable and surface air is warm and moist. In order to confirm whether wave-CISK mechanism is operating to maintain the simulated gravity waves, a numerical experiment NLHT that turns on the latent heating/cooling processes only in a 30-km-wide region near the gust front and turns off latent heating/cooling processes elsewhere. The NLHT run restarts from the history file of the 2D control storm at t = 9 h. Figure 2.27 shows the result of NLHT run at t = 10.5 h (1.5 h after the deletion of latent heating/cooling). It is clear that in the regions without latent heating/cooling proceses (x < 10 km and x > 40 km in Fig. 2.27), the gravity-wave amplitudes in the NLHT run are much weaker than in the control run (Fig. 2.10). Thus, the simulated gravity waves are indeed maintained by the wave-CISK mechanism.

Furthermore, in the NLHT run, there are more waves propagating in the vertical and less waves are trapped. In particular, gravity waves are trapped within the troposphere ($0 < z < 14$ km) in the control run (Fig. 2.10). In the NLHT run, however, waves are trapped only in the 30-km-wide region near the gust front where the latent heating/cooling processes are turned on (10 km < x < 40 km in Fig. 2.27). The reason is because without the latent heating/cooling, the pressure perturbation within the storm is reduced; as a result, the vertical wind shear of horizontal wind is decreased. Then the vertical gradient of the

Scorer parameter is reduced, so fewer waves are trapped, and more waves are propagating in the vertical. Therefore, once waves are generated, the simulated gravity waves are further maintained by the wave-CISK mechanism to propagate rearward and forward for long distances.

The ducting mechanism discussed by Lindzen and Tung (1976) requires a presence of a stable layer acting as a wave duct beneath a less-stable (or unstable) upper layer. From Fig. 2.25, this condition holds within the storm in general; the low-level air in the cold pool is highly stable (see Fig. 2.12 and the shaded area in Fig. 2.25), and the midlevel warm air is unstable as a result of release of latent heat (hatched area in Fig. 2.25). Lindzen and Tung (1976) further indicate that the concurrence of critical levels (levels at which the horizontal wind speed equals to the gravity-wave's phase speed) and low Richardson number ($R_i < 0.25$) in the upper less-stable layer for optimal ducting. It is clear from Fig. 2.26 that the critical levels occur in the low-Richardson-number regions ($R_i < 1.0$), but only in a small portion ($x = 30$–50 km). Therefore, the "static" components of the ducting mechanism—a lower stable layer and an upper less-stable layer—can exist over broad areas. In contrast, the "dynamic" components of the ducting mechanism—sufficient shear (strictly for $R_i < 0.25$, or loosely for $R_i < 1.0$) and critical levels—are only available over a small area. Similar results are also found in Powers (1994) in his simulated mesoscale gravity waves. The static effect seems to play a more important role in ducting waves in the lower stable cold pool than the effects of shear and critical level.

Therefore, once convection is initiated near the gust front, convective instability and/or shear instability contribute to the generation of the simulated gravity waves. Wave-CISK and ducting may both support and maintain the simulated convective-scale gravity waves. However, because of the strong sensitivity of wave amplitudes to latent heating/cooling and the weakness of the wave duct, wave-CISK may contribute more to the wave maintenance.

2.7 Summary

The traditional view of a multicell storm is as follows. It has been thought of as a cluster of short-lived single cells in which the cold air outflows from each cell combine to form a large gust front; the convergence along its leading edge being generally strongest in the direction of storm motion. This convergence is envisaged to trigger new cell

development along the gust front. The old cell dissipates when a new cell appears ahead of it along the gust front and "cuts off" the old cell's supply of moisture and buoyant air. Each individual cell within a multicell storm is assumed to go through such a life cycle and move roughly with the mean wind. What is meant by "triggering" and "cutting off" has remained unclear.

Two-dimensional and three-dimensional simulations of a midlatitude squall line in this chapter, using a high-resolution nonhydrostatic convection-resolving model, suggests that the multicellular structure with a squall line can be interpreted physically in terms of gravity waves generated by convection. Time-lapse display of model output demonstrates that *the process conventionally interpreted as the "cut-off" of old cells is actually a gravity-wave phenomenon.* Once the precipitation-induced cold pool is strong enough, there is a low-level updraft *continuously* generated at the leading edge of cold pool, which propagates at the speed of a density current. *Updraft cells behind this low-level leading edge updraft are transient gravity-wave features;* they form by periodically breaking away from the top of the low-level gust-front updraft, and they propagate rearward at phase speeds of gravity waves, not at the mean airflow speeds, as implied by the classic multicell model.

The persistence of the gust-front updraft fits the "weak evolution" mode of the multicell model of Foote and Frank (1983). The domination of front-to-rear propagation of gravity waves (as opposed to rear-to-front propagation) is due to the persistent upshear tilt of convective cells at the mature stage when the cold pool intensifies and baroclinic vorticity generation at the leading edge of the cold pool dominates over the ambient horizontal vorticity in the low-level wind shear (Rotunno et al. 1988; Fovell et al. 1992; Alexander et al. 1995).

Figure 2.28 is a schematic of the gravity-wave structure within a multicellular squall line, based on the 2D simulation results at $t = 11$ h of the 10-11 June 1985 PRE-STORM squall line. Convective cells in the troposphere exhibit a quadrature relationship between the w and p' (or u) fields, which indicates they are vertically trapped gravity waves. This phase relationship between the w and u fields in low levels is confirmed by the wind fields derived from Doppler radar observations. The gravity waves excited by the continuous low-level lifting at the gust front are trapped in the mid-to-upper troposphere because of a strong decrease of Scorer parameter with height as a result of strong vertical wind shear

and the decreased static stability aloft. A similar trapping mechanism was indicated by Gage et al. (1989) and Hauf (1993) for shallow trapped convection waves. Waves are also trapped in low levels because of the rigid flat ground. Trapped gravity waves only occur in a narrow area near the convective region initially; as the storm becomes well developed with stronger FTR and RTF jets, producing a stronger decrease of Scorer parameter with height, the trapped-wave area is wider.

Although most of the gravity waves associated with convective cells are trapped in the troposphere, some strong waves can "leak" through the troposphere and reach the stratosphere. Once waves pass into the highly stratified stratosphere, they have the typical structure of vertically propagating gravity waves—w is in phase with p', out of phase with u', and 90° ahead of θ' in the rearward mode, whereas w is in phase with both p' and u', and 90° behind θ' in the forward mode. The gravity waves in the lower stratosphere are mechanically forced by strong convective cells constantly impinging upon the tropopause in the convective region, as explained by Fovell et al. (1992) and Alexander et al. (1995).

Linear theory explains the multicellular structure inferred from the nonlinear numerical simulation. Linear theory predicts the amplitudes of w, p', and u' perturbations, the phase relationships between these variables, and the strong vertical tilt of the constant phase line in the lower stratosphere. Linear theory thus gives a dynamical framework for thinking about multicellular thunderstorm structure as a gravity-wave phenomenon.

The basic characteristics of these trapped tropospheric gravity waves are wavelengths (λ) of 16–20 km, storm-relative phase speeds (c) of –20 to –25 m s⁻¹, and periods ($T = \lambda/c$) of 10.7–16.7 min, which are consistent with the generation periods of precipitation cells at the mature stage in the leading portion of the storm. In the trailing stratiform region, the amplitudes of these gravity waves become weaker, but their wavelengths become longer ($\lambda = 25$–35 km) with faster phase speeds (storm-relative phase speeds are $c = -30$ to –40 m s⁻¹), in accordance with the dispersion relationship for internal gravity waves.

Once the precipitation-induced cold pool is strong enough to initiate convection continuously at the gust front, latent heating/cooling further contributes to the generation of gravity waves. Shear may also contribute to wave generation as in Kelvin-Helmholtz waves, but the definite role of shear instability needs to be confirmed in a future simulation

with much finer resolution. Wave-CISK and ducting may both support and maintain the simulated convective-scale gravity waves. However, because of the strong sensitivity of wave amplitudes to latent heating/cooling and the weak effectiveness of the wave duct, wave-CISK may contribute more to the wave maintenance.

This gravity-wave explanation for the multicellular structure of thunderstorms and squall lines furthers our understanding of thunderstorm dynamics. The conventional interpretation of new cells being advected (in the storm-relative sense) rearward and "cut off" from their moisture supply is inconsistent with the realistic model simulation in two respects. The low-altitude updraft cell at the gust front is continuous; its mover is advected rearward. The pulse of vertical velocity that breaks off from the gust-front updraft moves rearward at a wave propagation speed, not at the speed of the air. The gravity-wave interpretation of cells does not suffer these inconsistencies.

The different characteristics (wavelengths, phase speeds) of the gravity waves between the convective and stratiform region may explain why convective momentum transport has different characteristics in the convective and stratiform regions of a squall line with a trailing stratiform region (Gallus and Johnson 1992; Yang and Houze 1992; see also Section 4.5.3). The gravity-wave interpretation also may be useful for the parameterization of multicell-type convective systems in large-scale models.
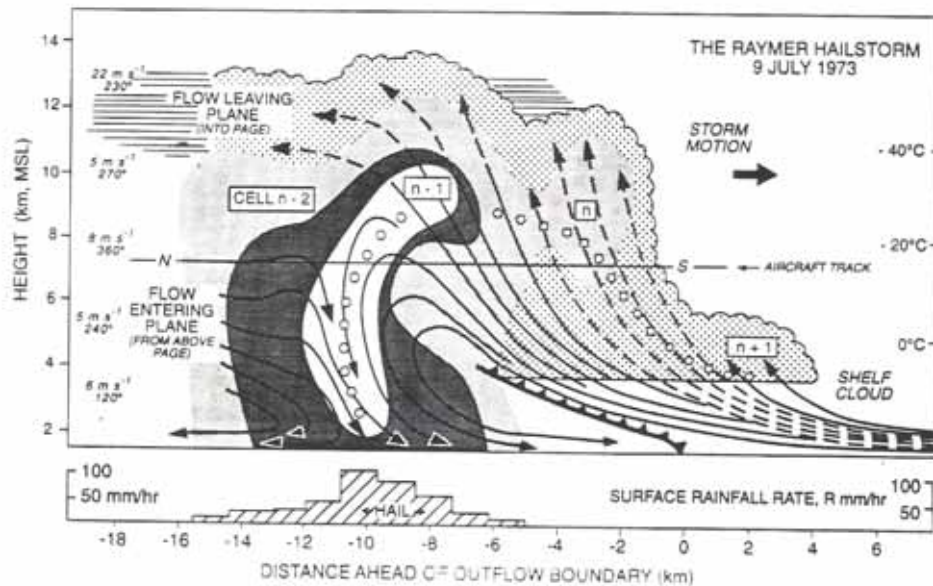
Fig. 2.1 Schematic model of a multicell storm in northern Colorado showing a vertical section along its direction of motion. Thick lines are smoothed streamlines of flow relative to the moving storm; they are broken on the left side of the figure to represent flow into and out of the plane and on the right side of the figure to represent flow remaining within a plane a few kilometers closer to the reader. Lightly stippled shading: extent of cloud; darker grades of shading: radar reflectivity of 35, 45, and 50 dBZ; open circles: trajectory of a hailstone during its growth from a small particle. Right: temperature scale; temperature of a parcel lifted from the surface. Left: environment winds relative to the storm based on soundings behind the storm. Surface rainfall rates averaged over 2-min intervals during the passage of the storm are plotted at the bottom of the figure (from Browning et al. 1976).
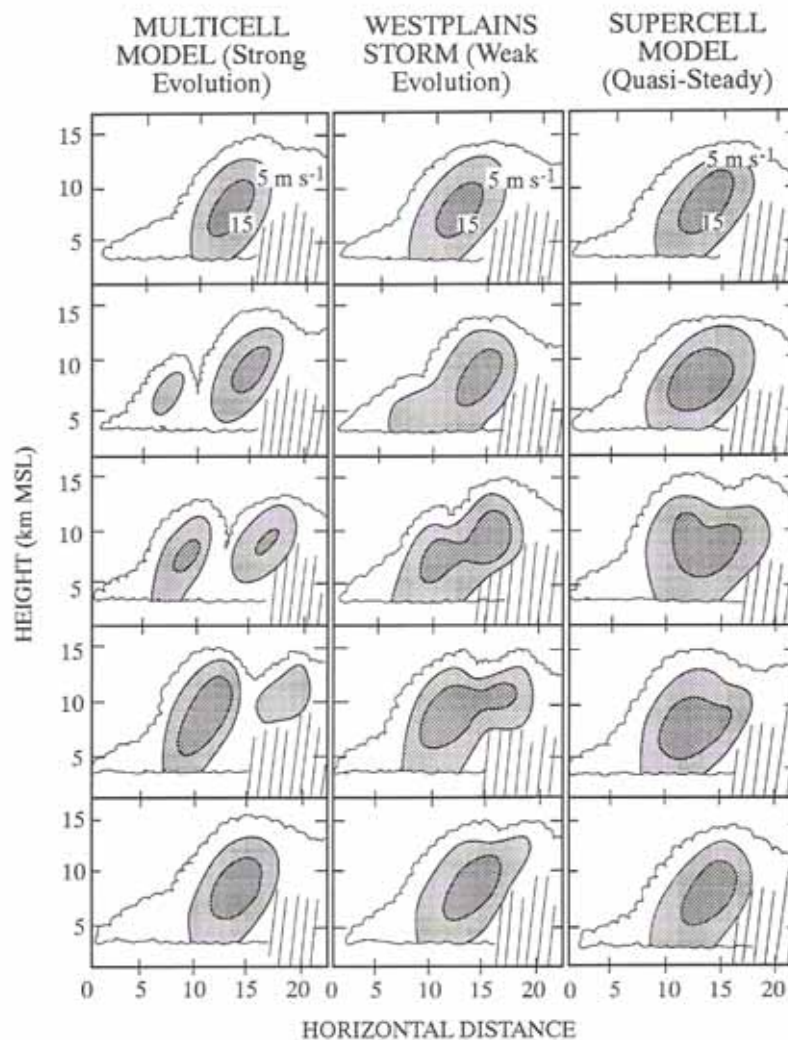
Fig. 2.2 Schematic diagram showing updraft evolution for three different storm models. Contours represent isotachs of vertical wind speed. Time between successive frames, moving down the figure, is 3–5 min. Vertical velocity of updraft greater than 15 m s^{-1} is heavily shaded, and vertical velocity of updraft between 5 and 15 m s^{-1} is lightly shaded (from Foote and Frank 1983).
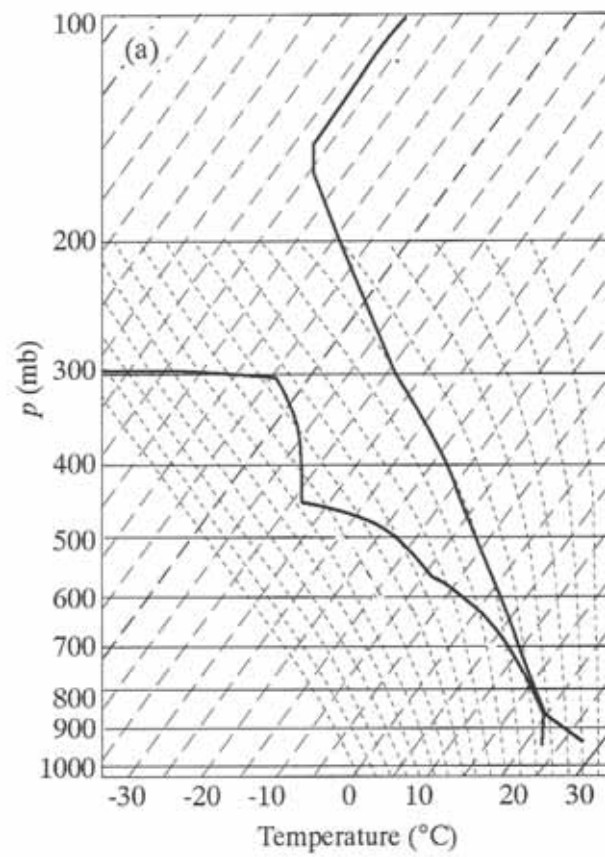
Fig. 2.3 (a) Temperature and dewpoint soundings of Enid, Oklahoma on 2331 UTC 10 June 1985.
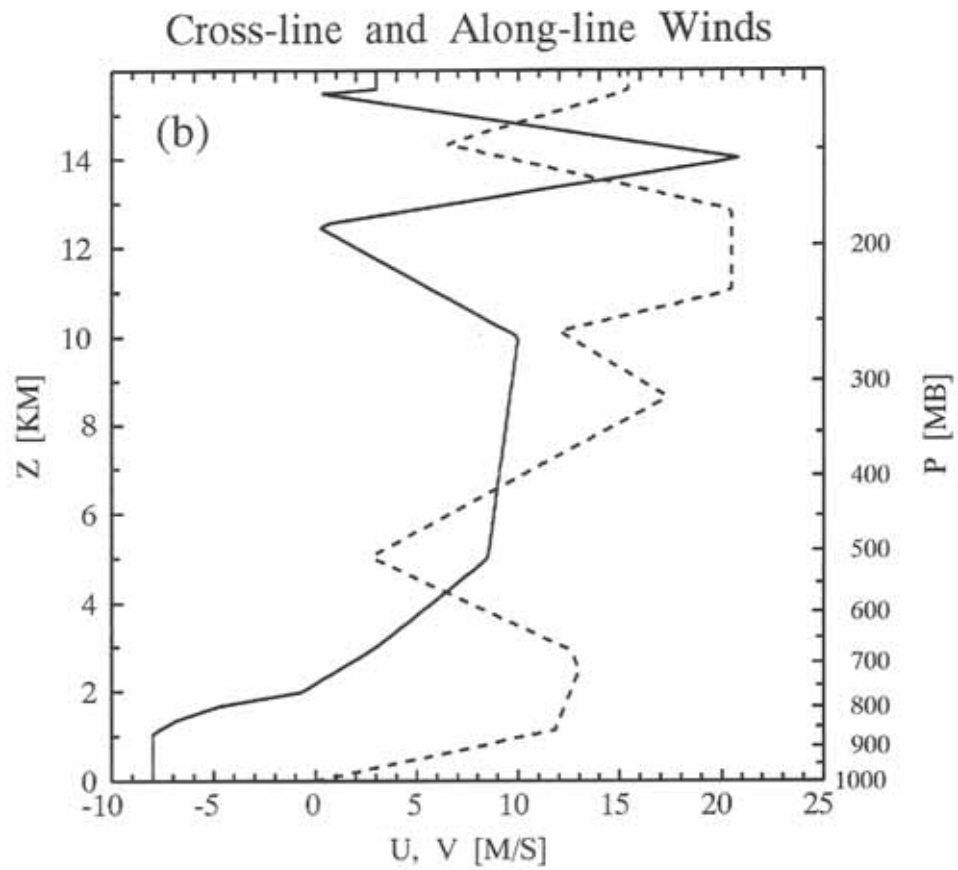
Fig. 2.3 (b) The ground–relative wind of Enid, Oklahoma on 2331 UTC 10 June 1985. Solid line is the cross–line component, and the dashed line is the along–line component.
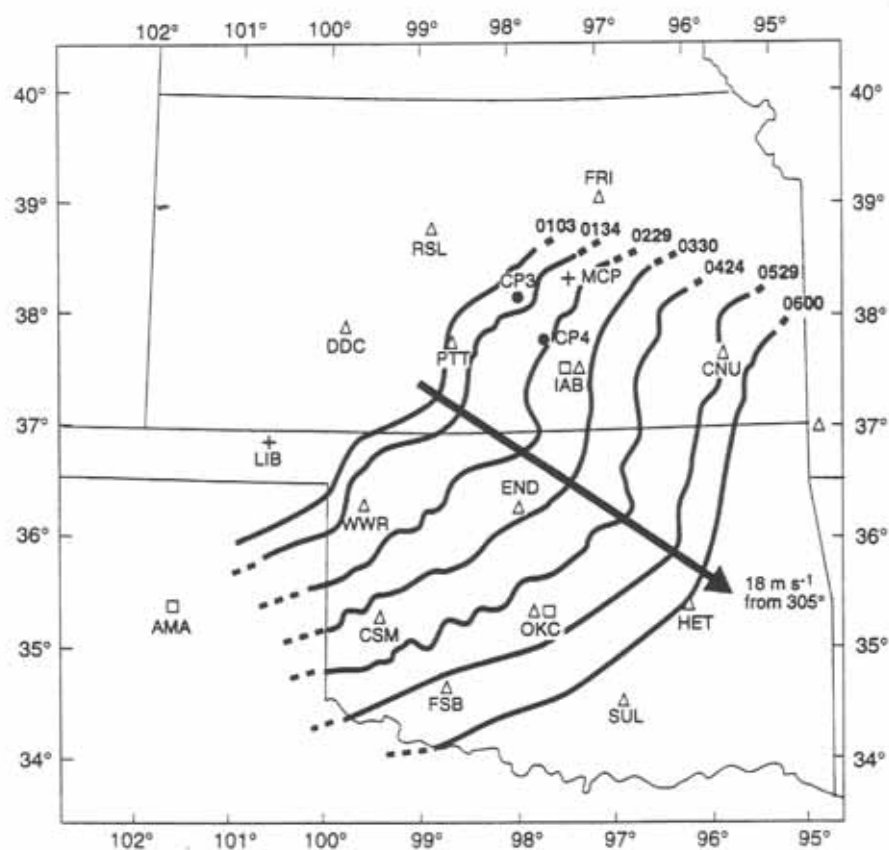
Fig. 2.4 Isochrones of leading edge of the 10–11 June 1985 squall line. Dashes indicate that the true end of the squall line extends beyonds that shown. The heavy, straight arrow shows the location of the squall line center as a function of time (from Biggerstaff and Houze 1991a).
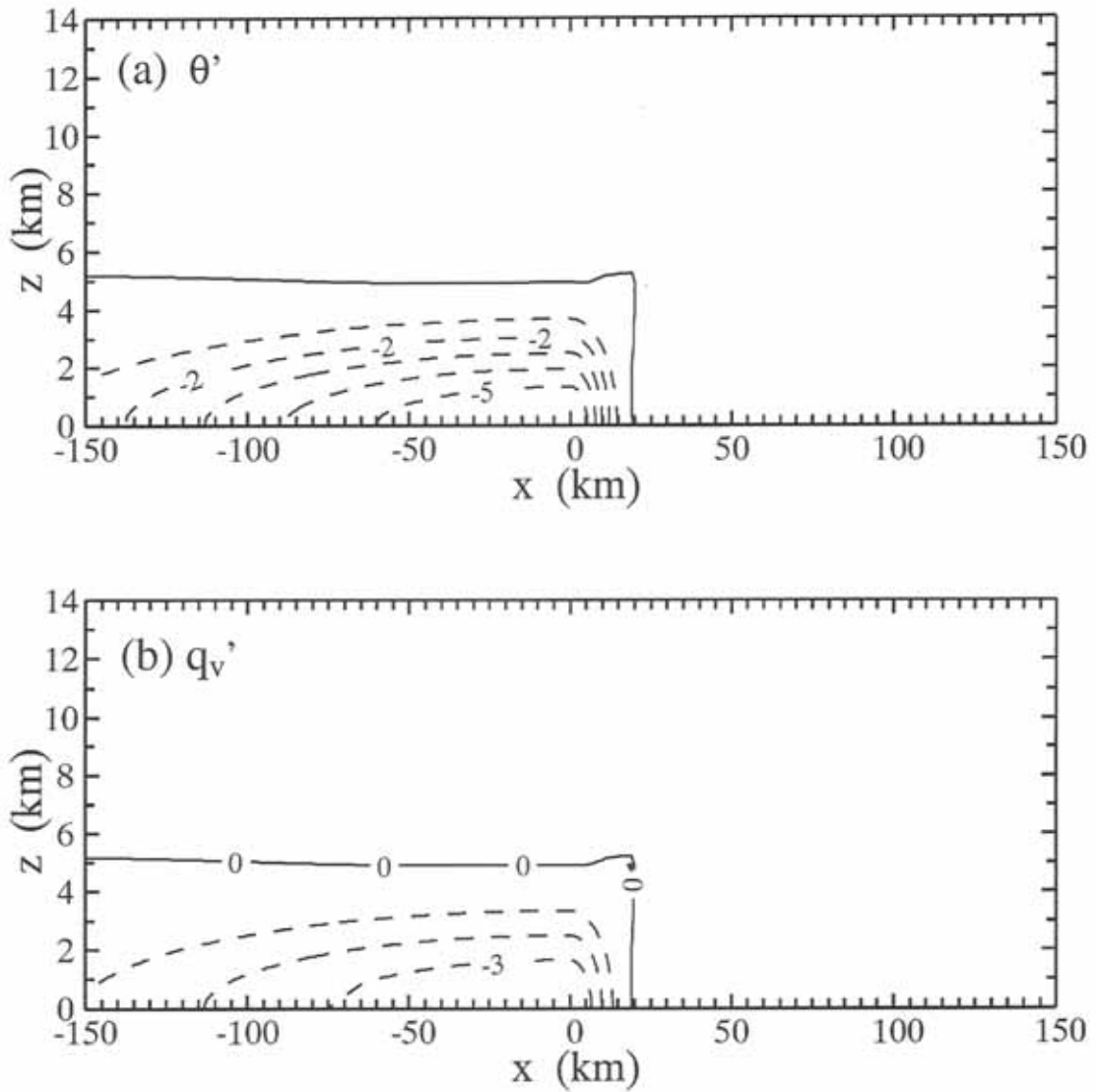
Fig. 2.5 (a) Potential temperature perturbation (with a contour interval of 1 K) and (b) water vapor mixing ratio perturbation (with a contour interval of 1 g kg^{-1}) of the cold pool used to initiate convection. Negative fields are dashed.
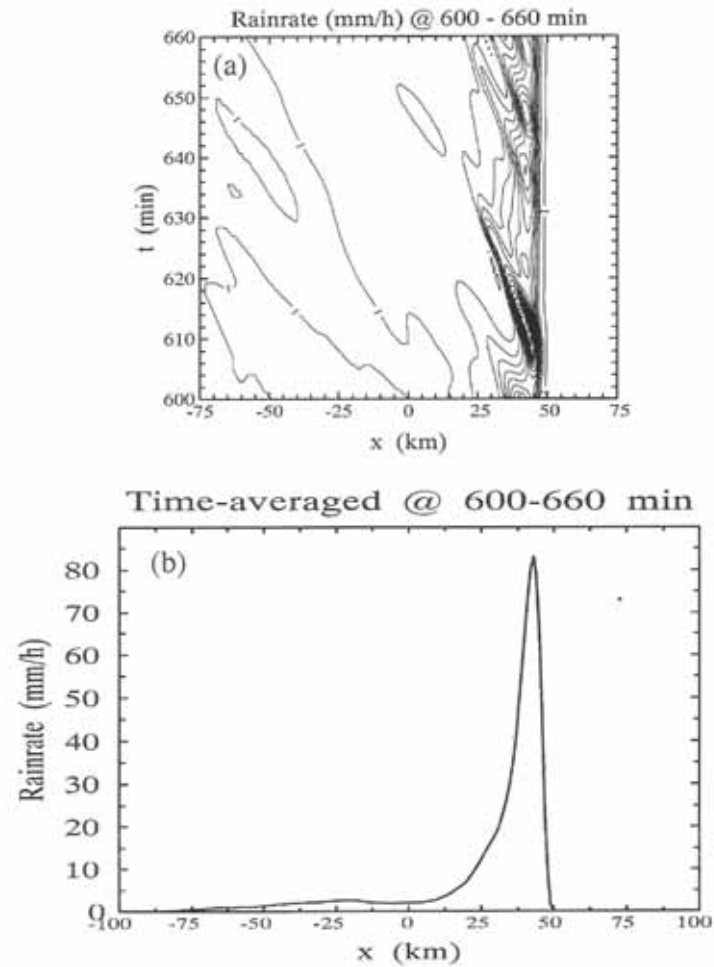
Fig. 2.6 (a) Time history of surface rainfall rate during a 1–h period (600–660 min) and (b) the 1–h–averaged surface rainfall rate at the mature stage of the simulated 2D storm. Contour lines in (a) start from 1 mm h^{-1}, with an interval of 10 mm h^{-1}. It is displayed in a storm–relative coordinate system moving at a speed of 12.2 m s^{-1} relative to the ground.

U-Cgust (m/s) @ 600-660 min
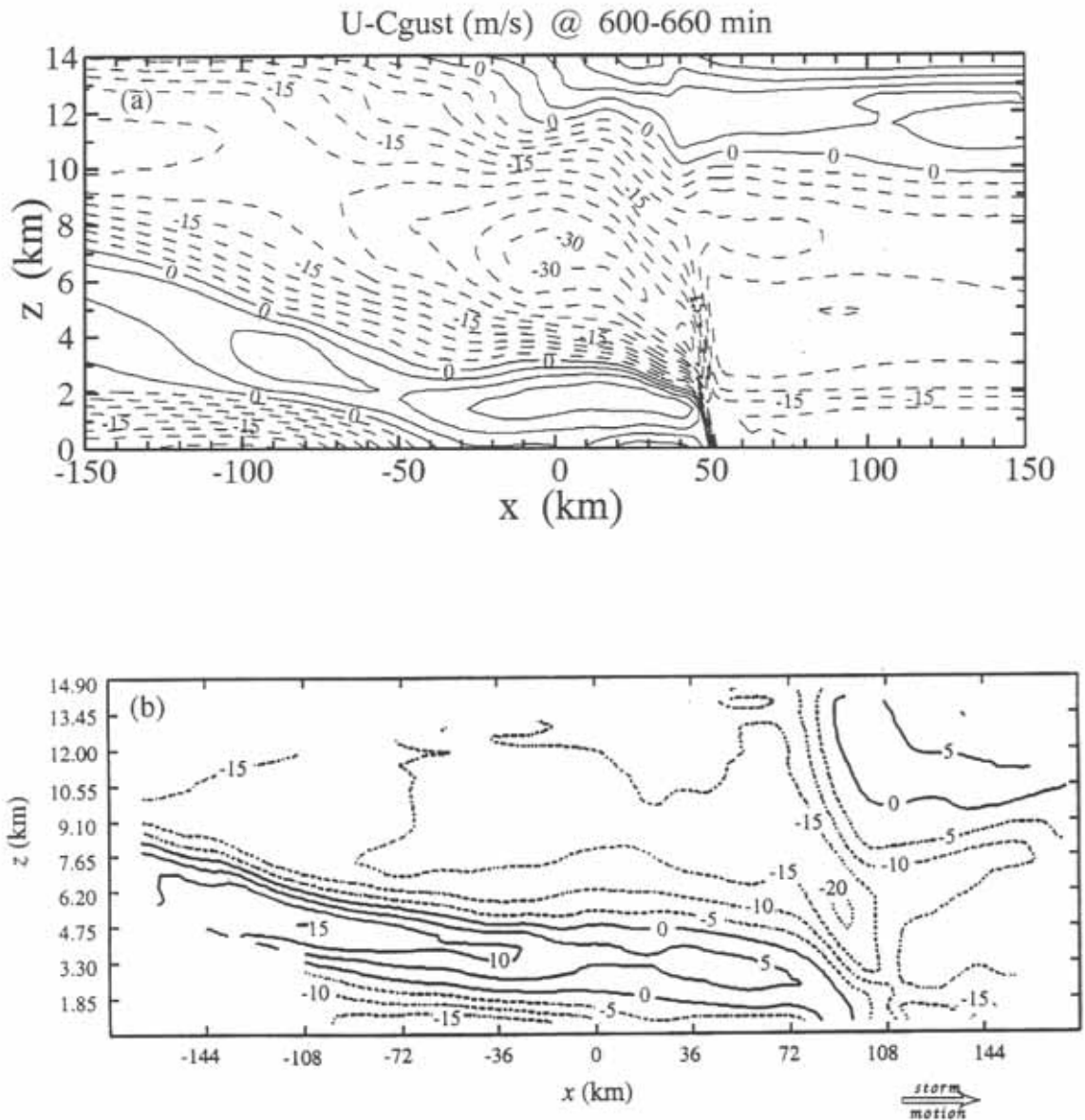
Fig. 2.7 (a) Time–averaged storm–relative cross–line wind field (with a contour interval of 3 m s^{-1}) of the 2D storm and (b) the along–line–averaged cross–line wind field (with a contour interval of 5 m s^{-1}) based on the dual–Doppler radar analysis (Biggerstaff and Houze 1993). Solid lines are rear–to–front (positive) flows, and dashed lines are front–to–rear (negative) flows.
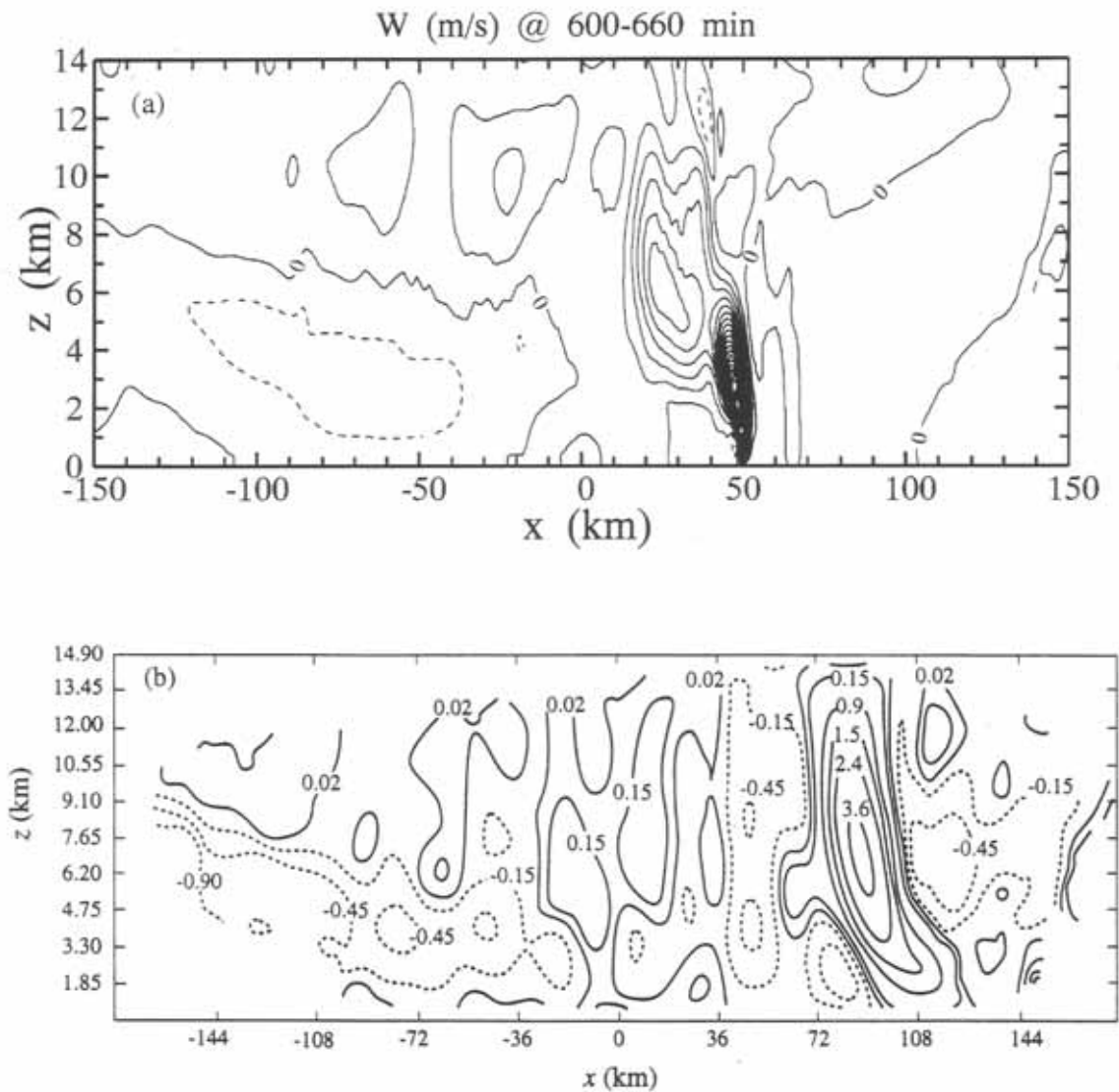
Fig. 2.8 (a) Time–averaged vertical velocity field (with a contour interval of 0.5 m s^{-1}) of the 2D storm and (b) the vertical velocity field based on the dual–Doppler radar analysis (Biggerstaff and Houze 1993). Vertical velocity in (b) is contoured at 3.6, 2.4, 1.5, 0.9, 0.15, 0.02, –0.15, –0.45, –0.9 m s^{-1}. The positive field is in solid lines and negative field is dashed.
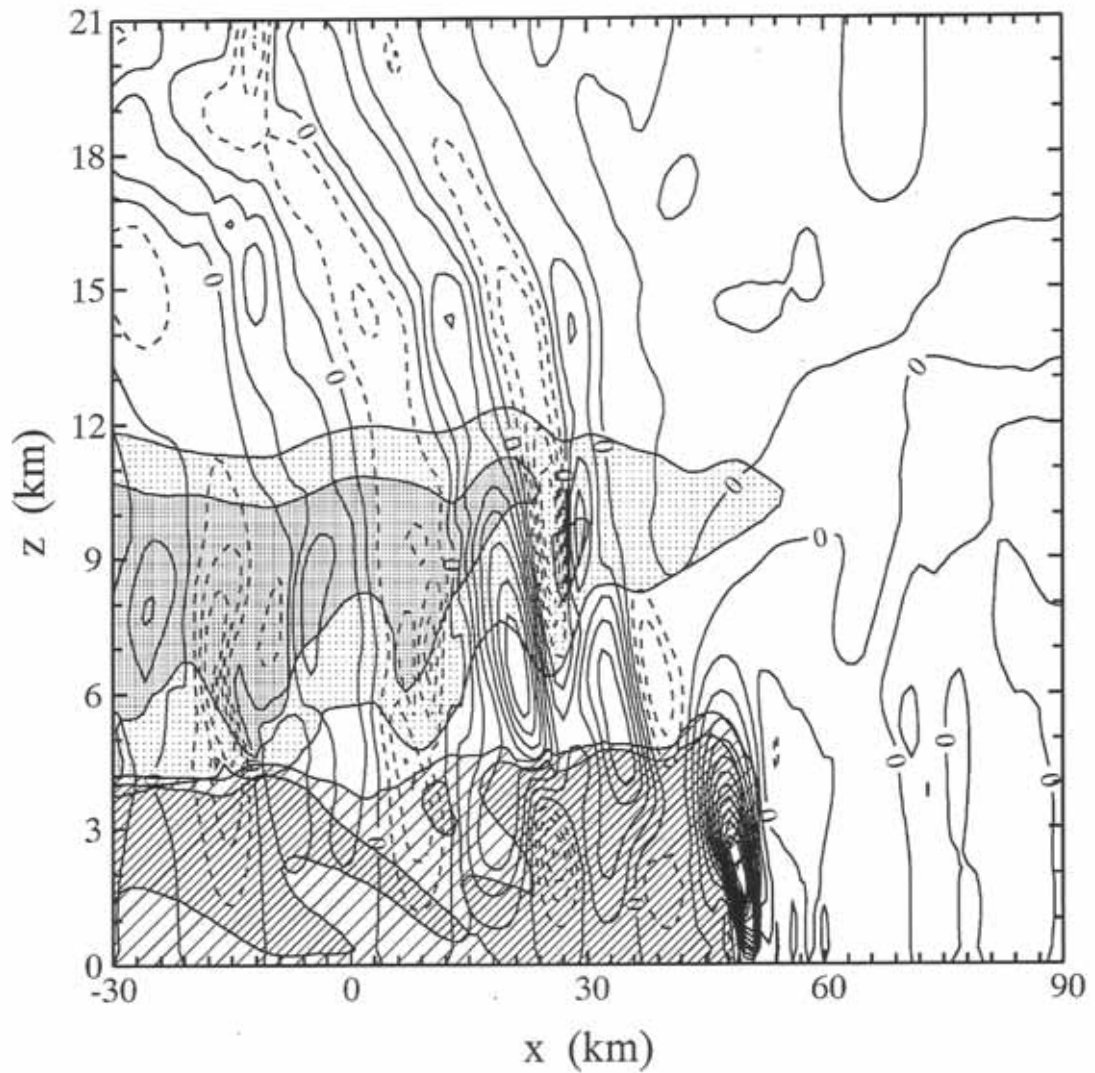
Fig. 2.9 Vertical velocity (with a contour interval of 1 m s^{-1}) of the simulated 2D storm at $t = 11$ h. The positive field is in solid lines and the negative field is dashed. Snow mixing ratio greater than 2 g kg^{-1} is lightly shaded, and snow mixing ratio greater than 4 g kg^{-1} is heavily shaded. Rainwater mixing ratio greater than 0.1 g kg^{-1} is lightly hatched, and rainwater mixing ratio greater than 0.3 g kg^{-1} is heavily hatched. The gust front is near $x = 50$ km.
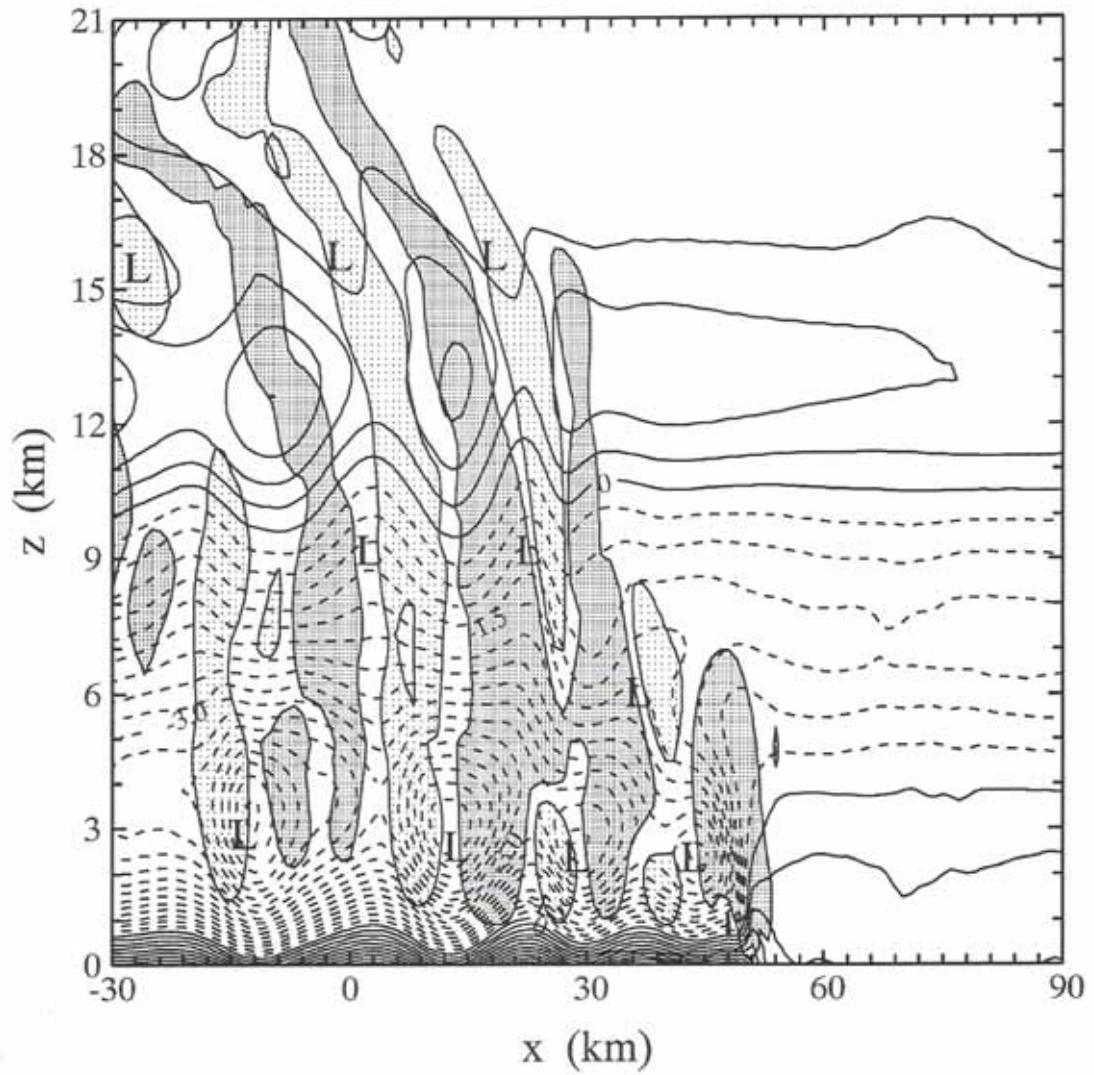
Fig. 2.10 Pressure perturbation (with a contour interval of 0.3 mb) of the simulated 2D storm at $t = 11$ h. The positive field is in solid lines and the negative field is dashed. Vertical velocity of updraft greater than 1 m s^{-1} is heavily shaded, and vertical velocity less than -1 m s^{-1} is lightly shaded. A letter of L denotes a region of low pressure. The detailed vertical velocity structure can be seen in Fig. 2.9.
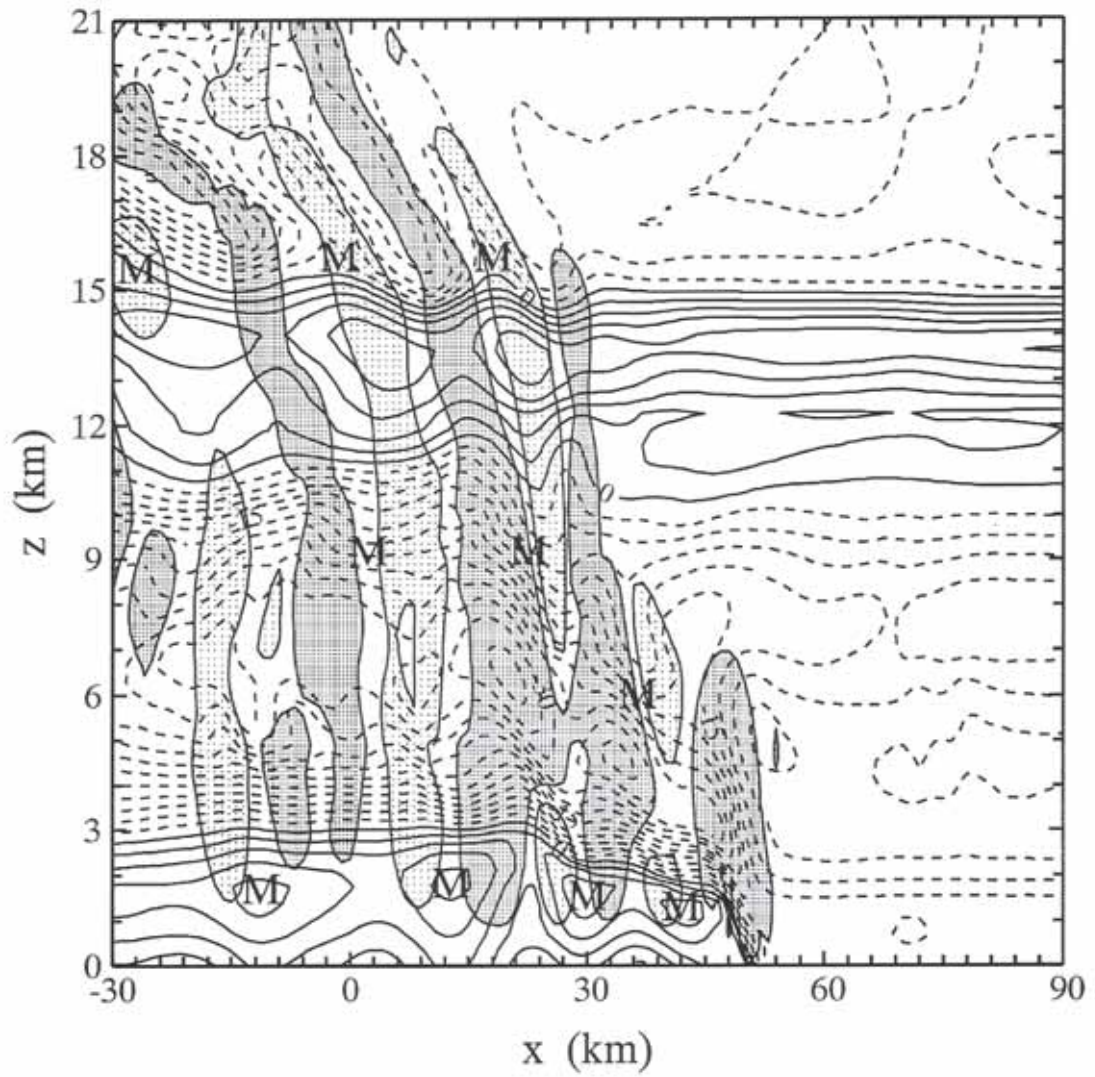
Fig. 2.11 As in Fig. 2.10 except for storm–relative horizontal wind (contour interval is 3 m s^{-1}). A letter M denotes a region of horizontal wind maximum.
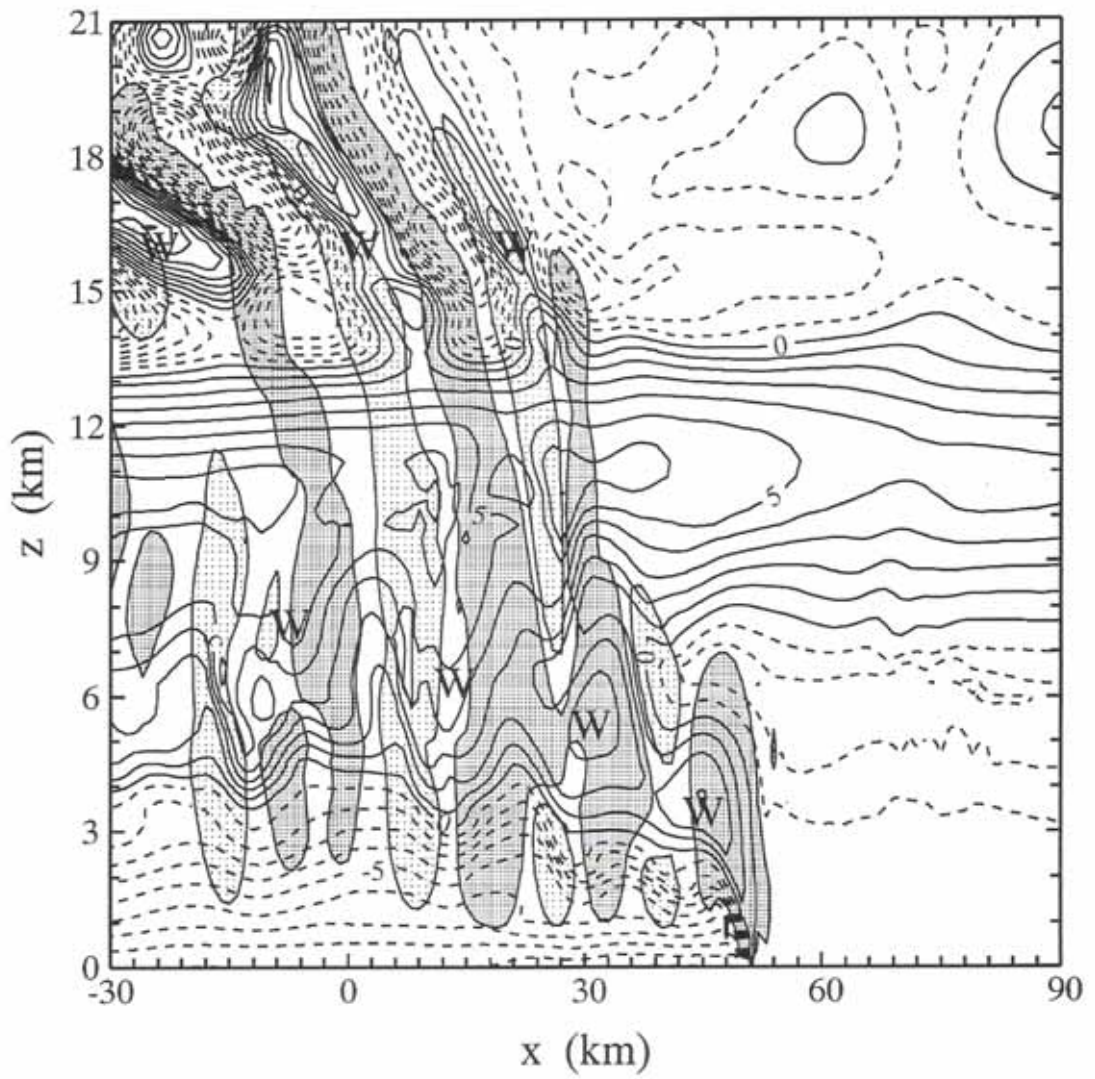
Fig. 2.12 As in Fig. 2.10 except for potential temperature perturbation (contour interval is 1 K). A letter W denotes a region of warm air.
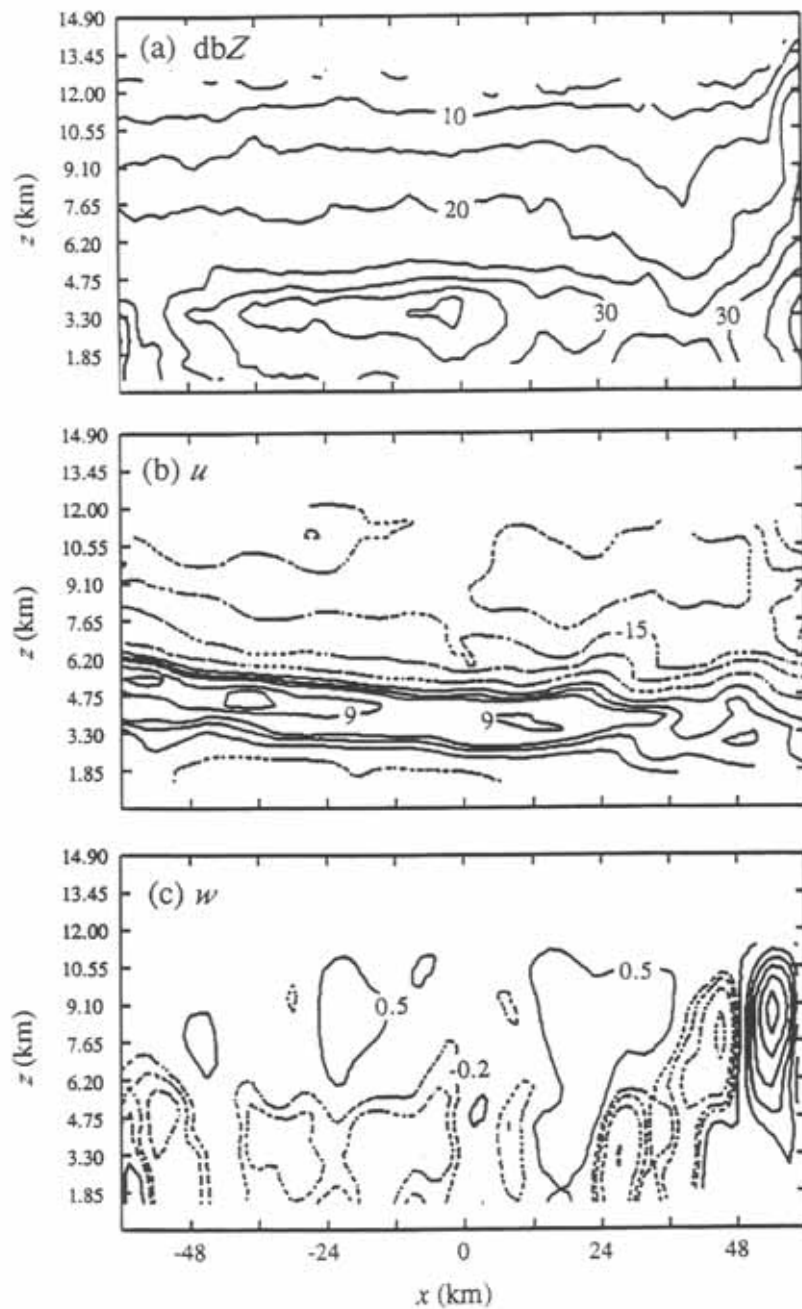
Fig. 2.13 (a) Dual–Doppler radar analysis showing radar reflectivity (dBZ), (b) storm–relative horizontal wind, and (c) vertical velocity at 0345 UTC 11 June 1985. Contours of reflectivity field in (a) starts from 5 dBZ with a contour interval of 5 dBZ; storm–relative horizontal wind field in (b) is contoured at –21, –18, –15, –6, 0, 3, 5, 9, and 12 m s^{-1}; vertical velocity field in (c) is contoured at –2, –1, –0.5, –0.2, 0.5, 2, 3, 4, 5, and 6 m s^{-1}. The positive field is in solid lines and the negative field is dashed.
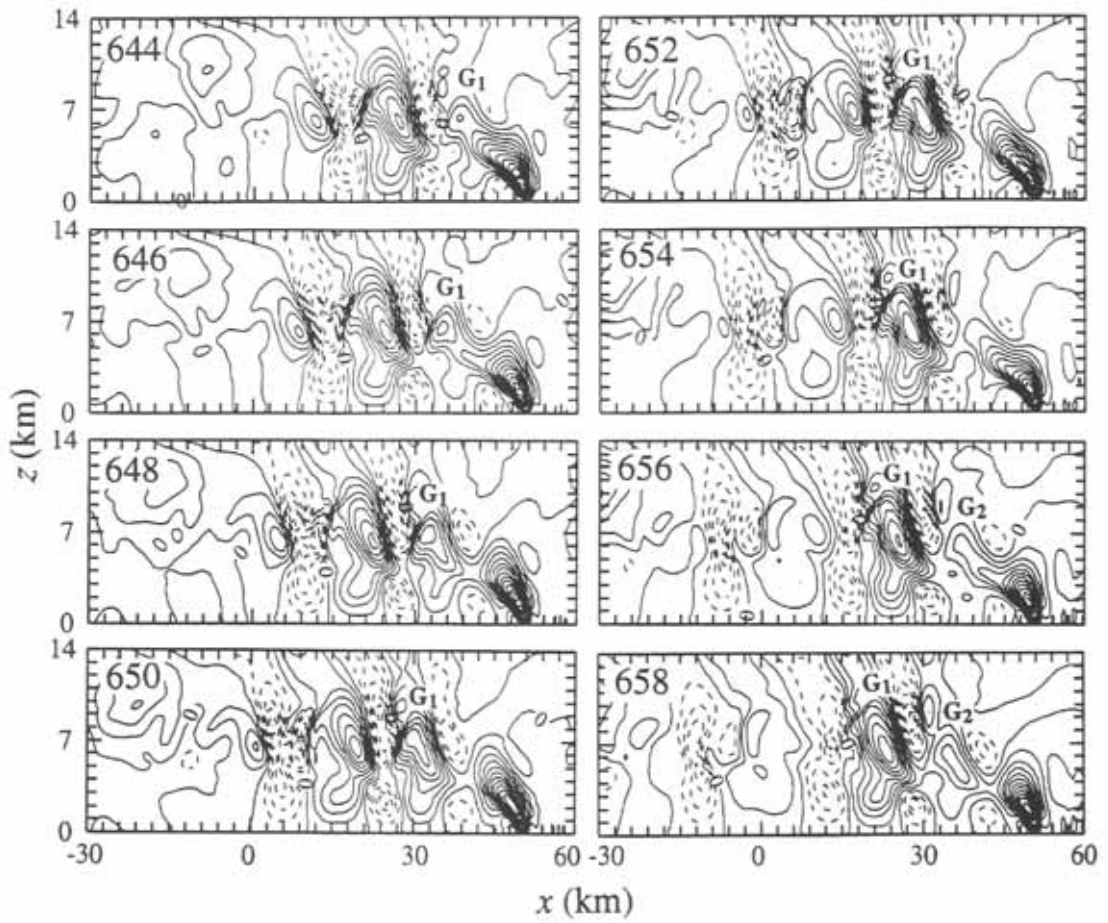
Fig. 2.14 Instantaneous vertical velocity contoured every 1 m s^{-1}, with negative value dashed for the 2D simulated storm. Panels are at 2–min intervals starting at $t = 644$ min. Gravity wave updrafts are denoted by G_1 and G_2.
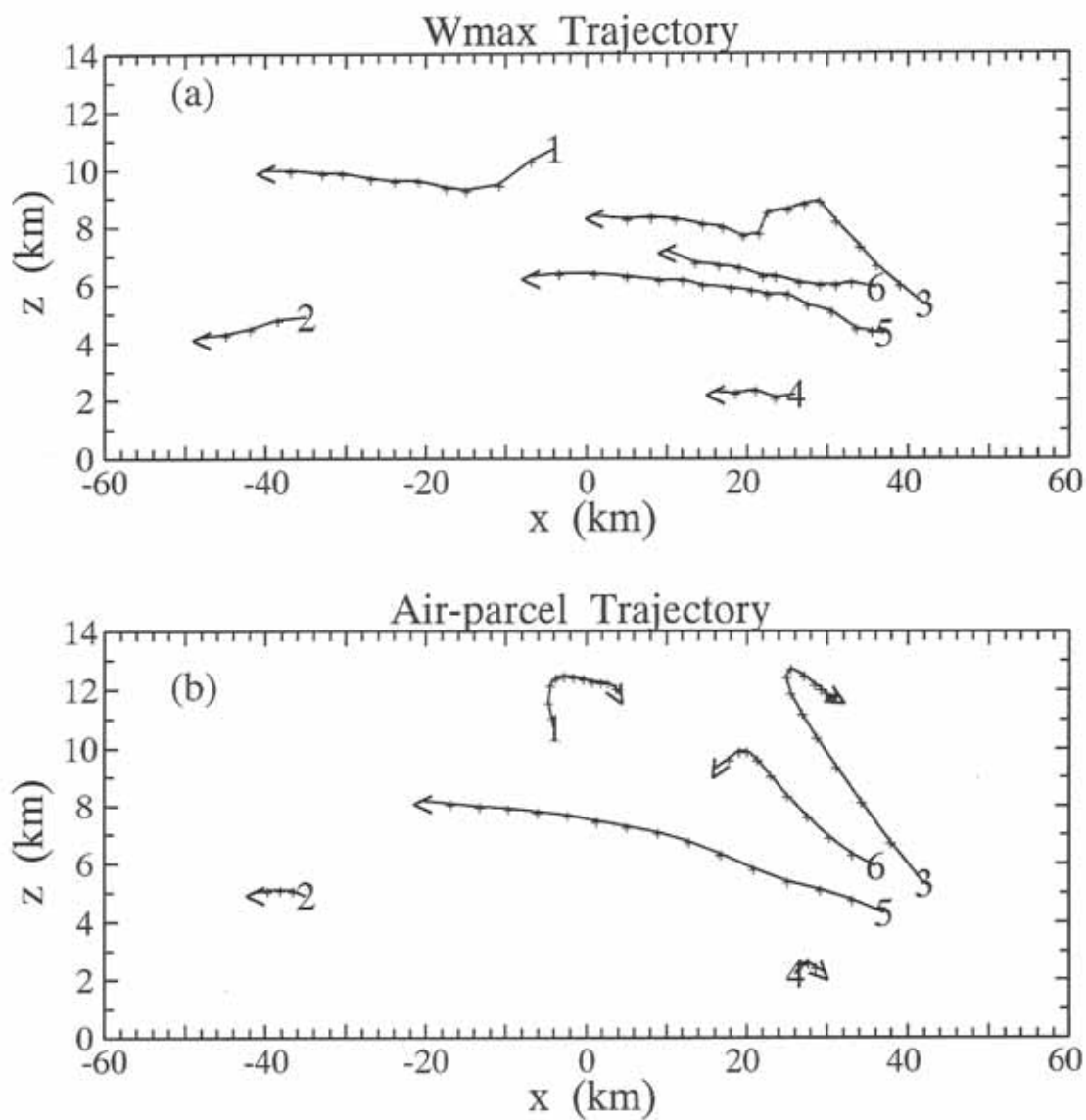
Fig. 2.15 (a) Convective cell (defined by the updraft center) trajectories and (b) the air–parcel trajectories starting from the same beginning points as the convective cell trajectories in (a) during the time period $t = 10$–11 h. Each cross (+) along the trajectories represents the position of an updraft center or an air parcel every 2 min. The arrowhead at the endpoint of each trajectory indicates its direction.
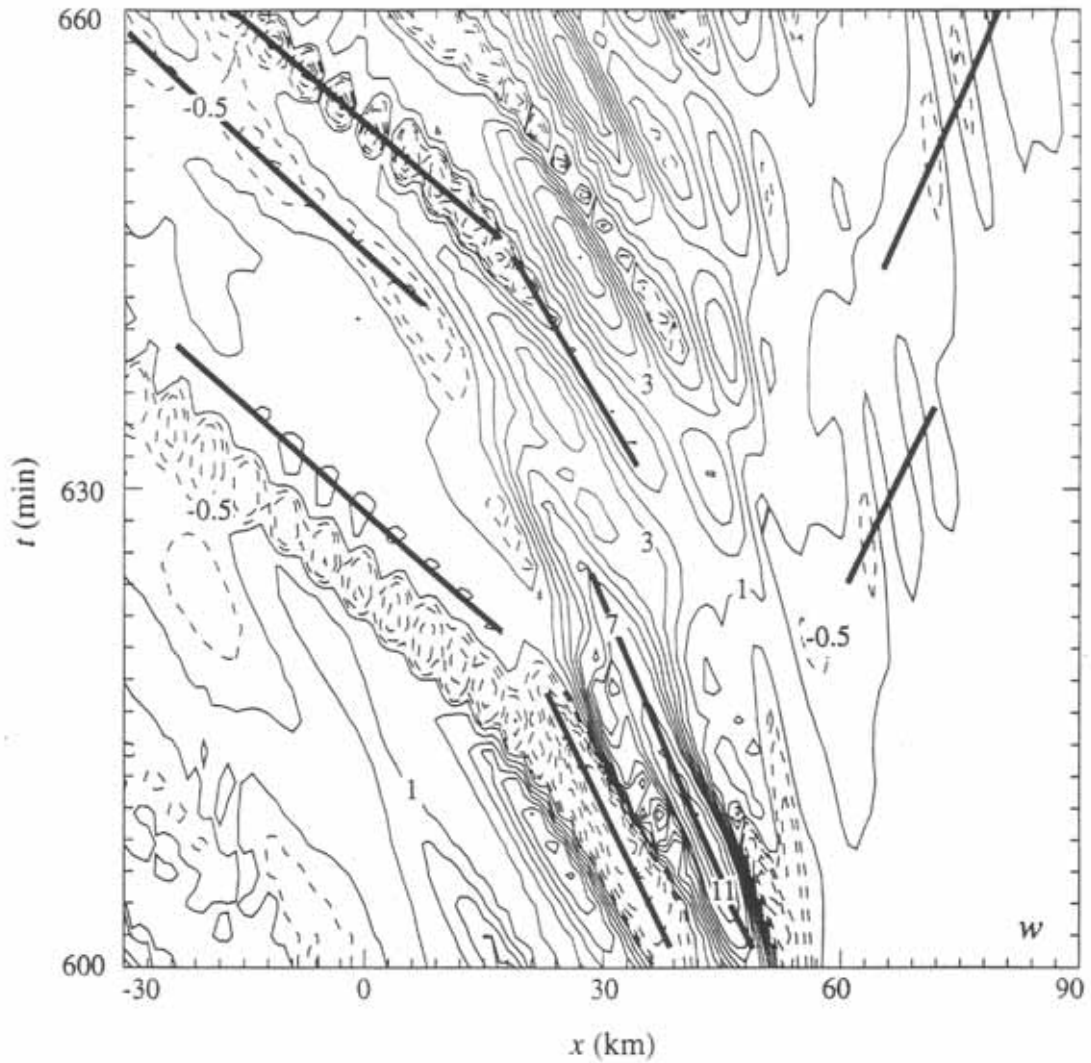
Fig. 2.16 Time–space plot of vertical velocity of the simulated 2D storm at $z =$ 5.25 km for the time period $t = 10$–11 h. Vertical velocity is contoured at –6, –4, –3, –2, –1, –0.5, 0, 1, 2, 3, 4, 5, 6, 7, 9, and 11 m s^{-1}. The positive field is in solid lines and the negative field is dashed. Heavy solid lines are some representative constant phase lines.
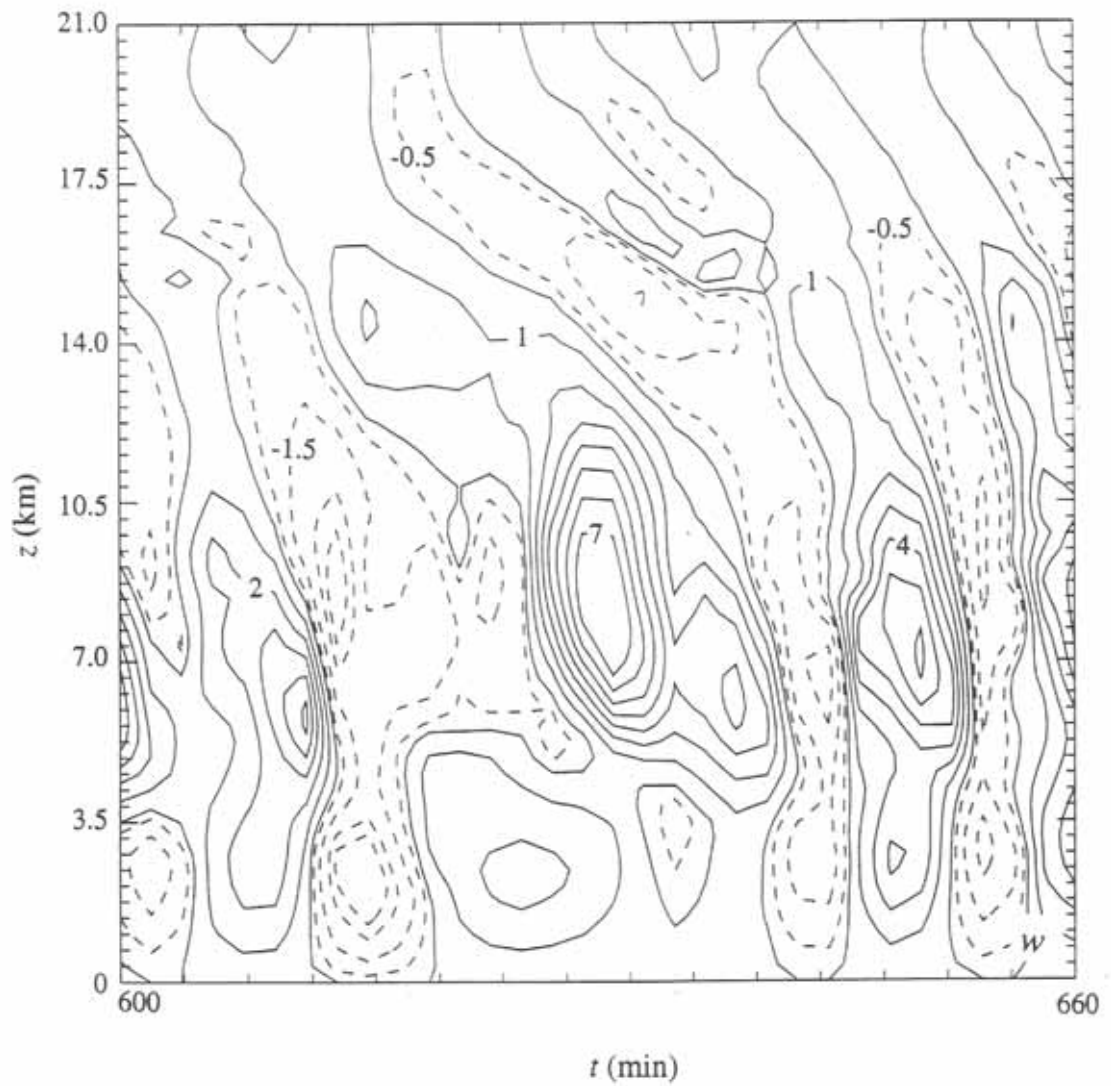
Fig. 2.17 Height–time plot of vertical velocity of the simulated 2D storm at $x =$ 18 km for the time period $t = 10$–11 h. Vertical velocity is contoured at –6, –4, –3, –1.5, –0.5, 0, 1, 2, 3, 4, 5, 6, 7, and 9 m s^{-1}. The positive field is in solid lines and the negative field is dashed.
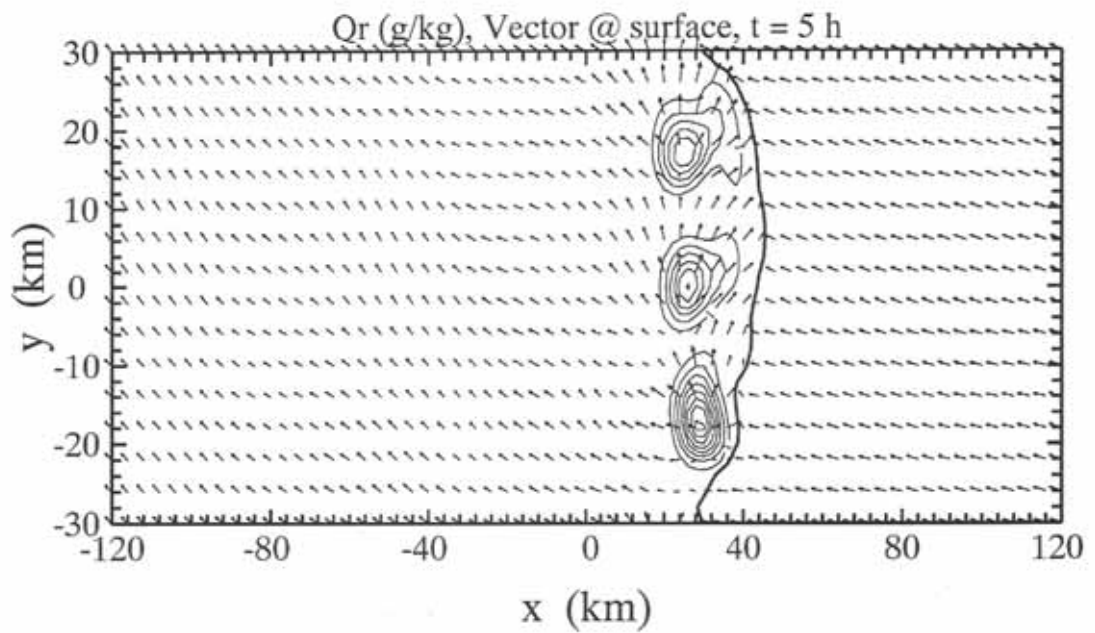
Fig. 2.18 (a) Surface rainwater mixing ratio and storm–relative wind vector for the simulated 3D storm. Contours of rainwater in (a) start at 1 g kg^{-1} with a contour interval of 1 g kg^{-1}. Wind vectors in (a) are plotted at every other grid point (4 km in x and y directions) and are drawn relative to a storm propagation speed of 7.22 m s^{-1}. A distance of two grid points (4 km) represents a vector magnitude of 30 m s^{-1}. The heavy line is the surface gust front denoted by $\theta' = -1$ K contour.
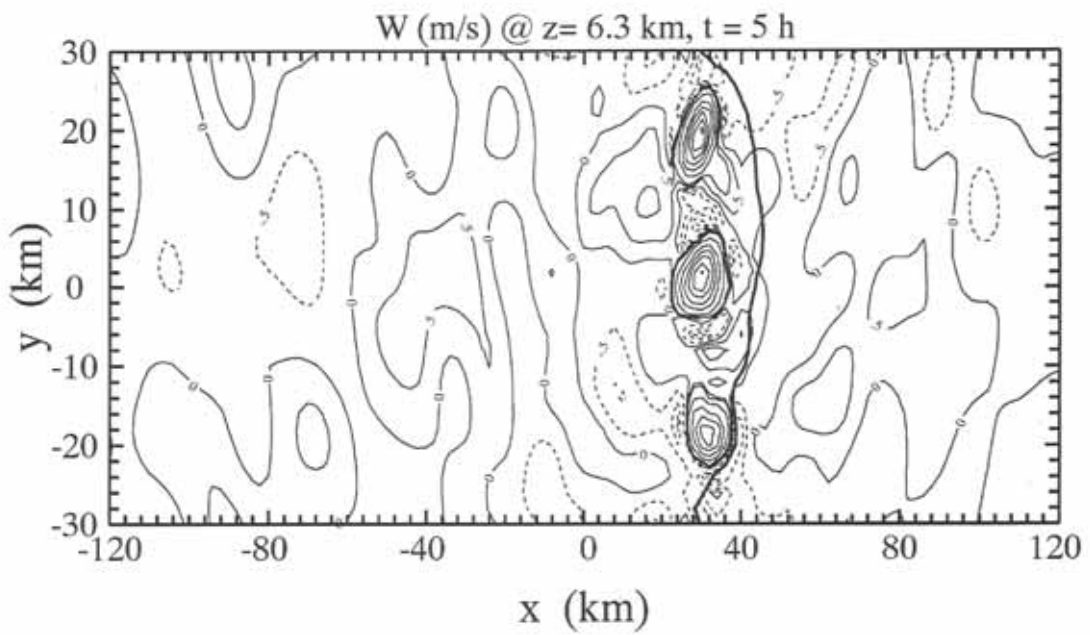
Fig. 2.18 (b) Vertical velocity at $z = 6.3$ km at $t = 5$ h for the simulated 3D storm. Vertical velocity is contoured at $-2, -1.5, -1, -0.5, 0, 0.5, 1, 3, 7, 11, 15, 19$, and 23 m s^{-1}. The positive field is in solid lines and the negative field is dashed. The heavy line is the surface gust front determined by $\theta' = -1$ K contour.
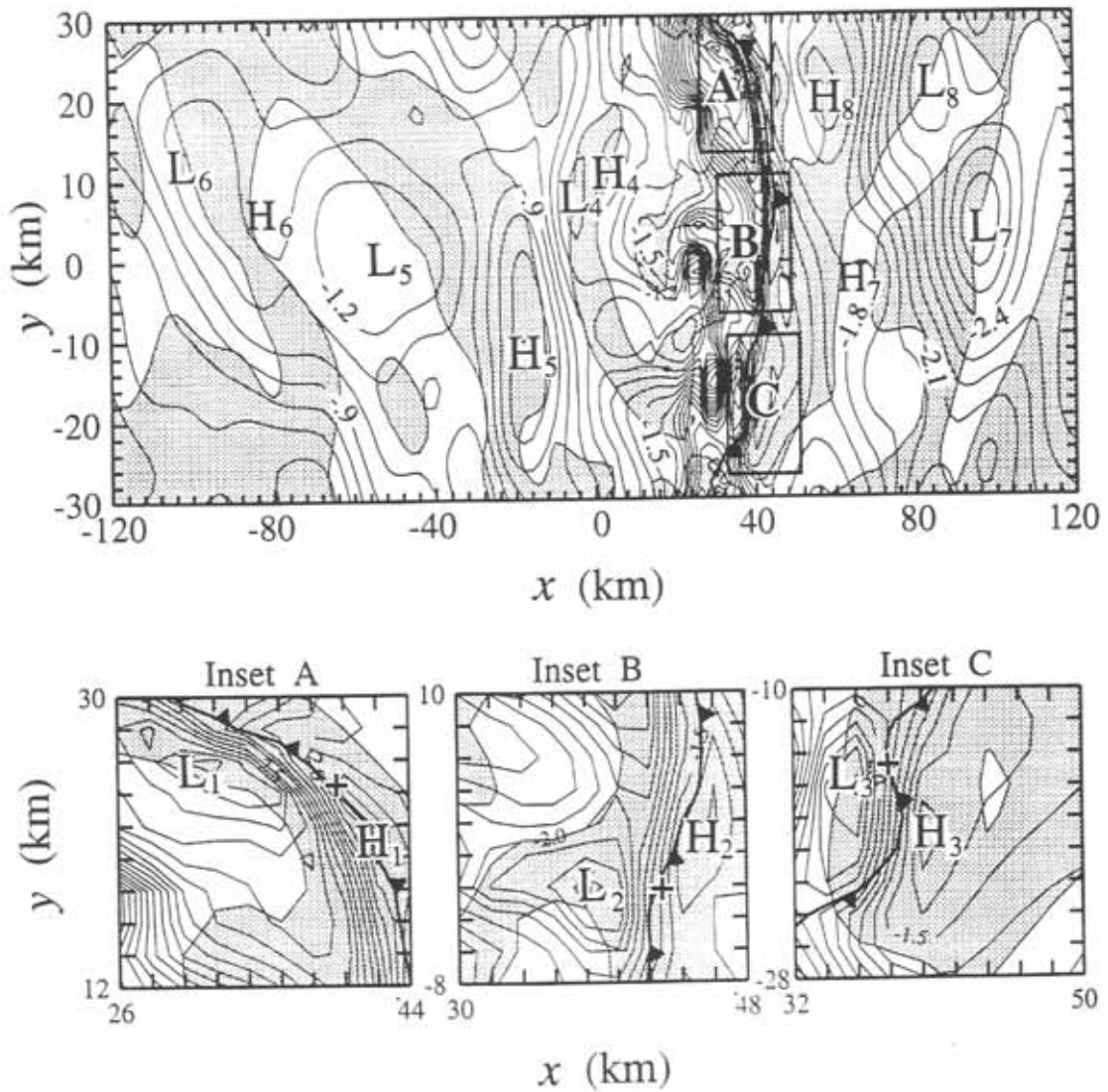
Fig. 2.19 Pressure perturbation p' at $z = 0.7$ km (with a contour interval of 0.1 mb), $t = 5$ h for the simulated 3D storm. The negative field is in solid lines and the areas of updrafts are shaded. The solid barbed line is the surface gust front determined by the $\theta' = -1$ K contour. Letters H or L denote regions of high and low pressures. Insets A, B, and C highlight the w/p' phase relationships for regions with size of 18 km x 18 km surrounding three strong convective cells near the gust front. Updraft center in each inset is indicated by a cross.
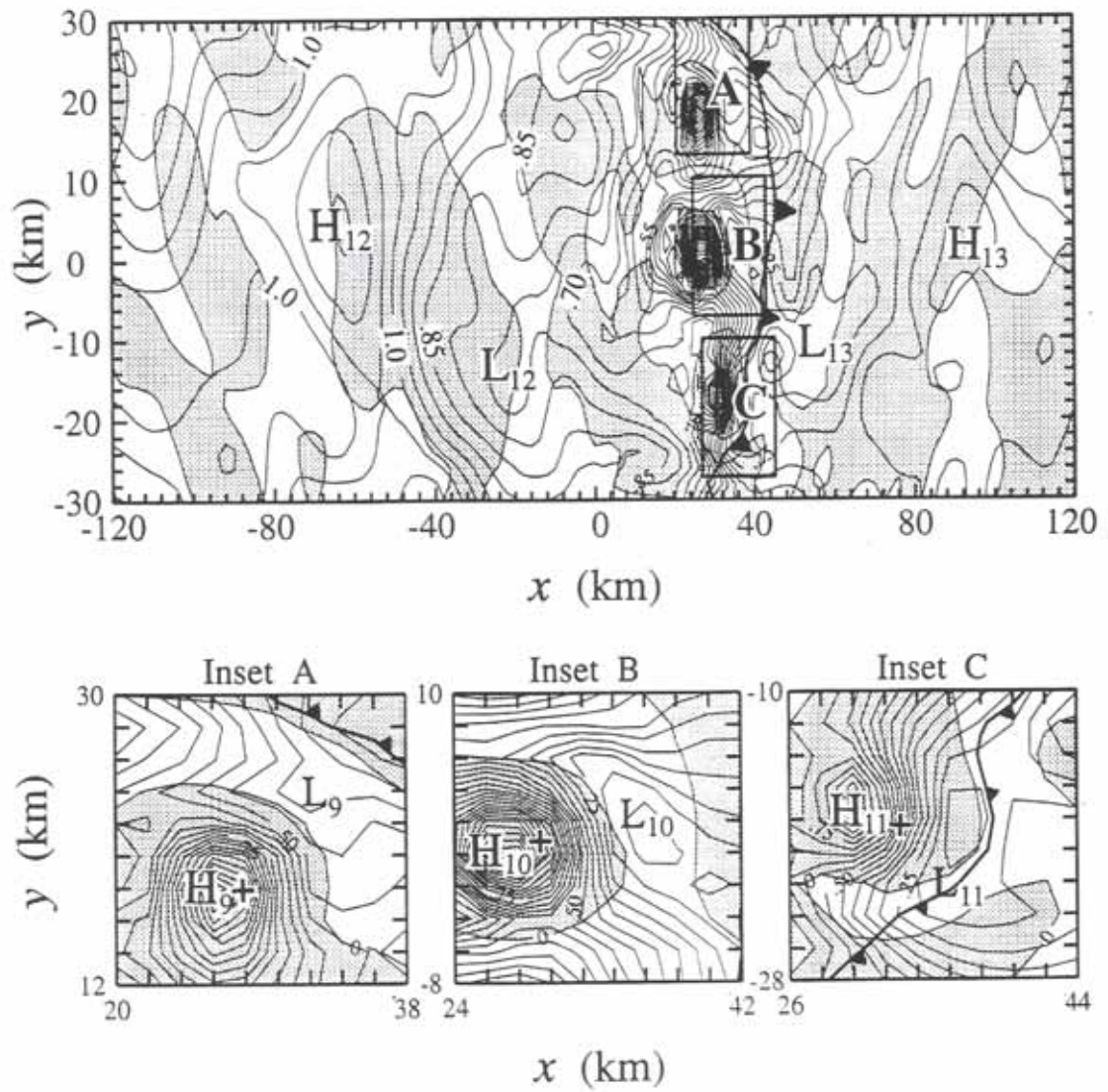
Fig. 2.20 As in Fig. 2.19 except for $z = 11.9$ km level (with a contour interval of 0.05 mb). The positive field is in solid lines.
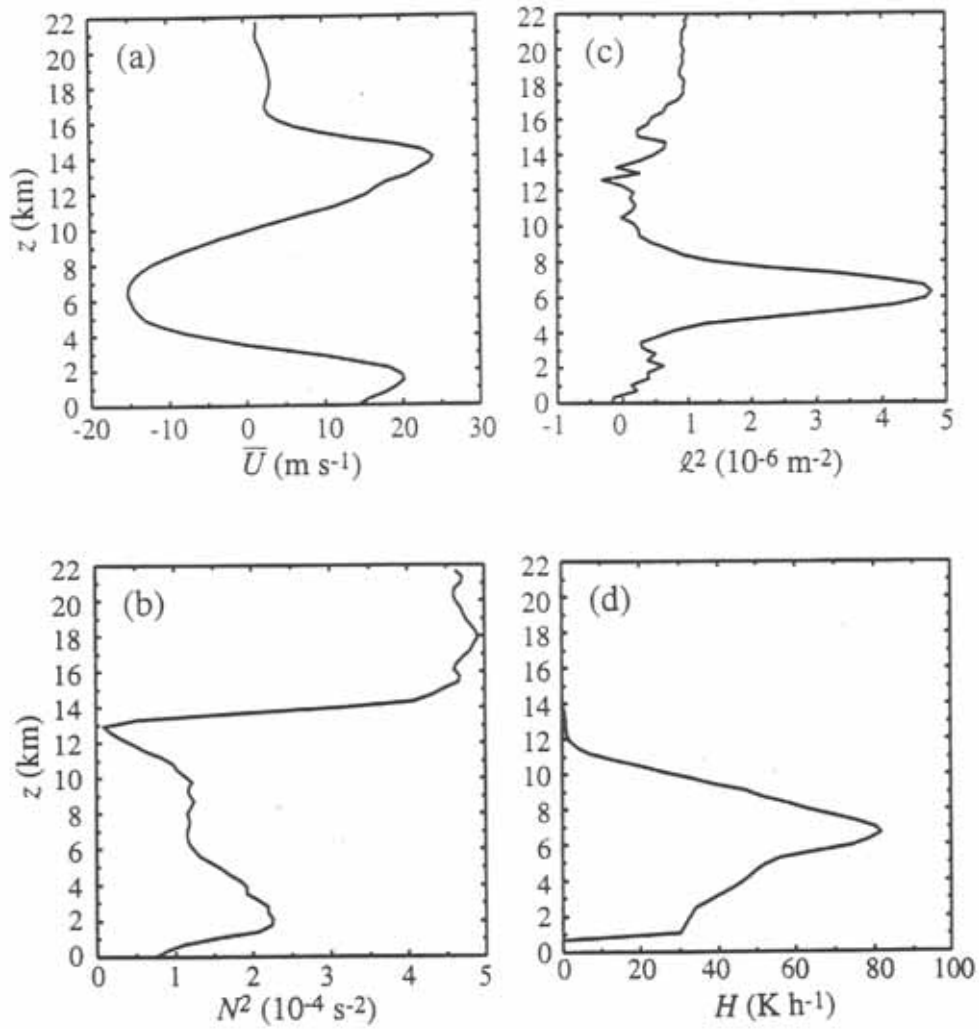
Fig. 2.21 (a) Vertical profiles of ground–relative wind $U(z)$, (b) $N^2(z)$, (c) Scorer parameter $l^2(z)$ averaged horizontally over a 70–km–wide region ($x = -20$ to 50 km), and (d) the smoothed latent heating $H(z)$ for the region $x = 10$ to 26 km for the simulated 2D storm at $t = 11$ h.

Linear Theory

Numerical Model
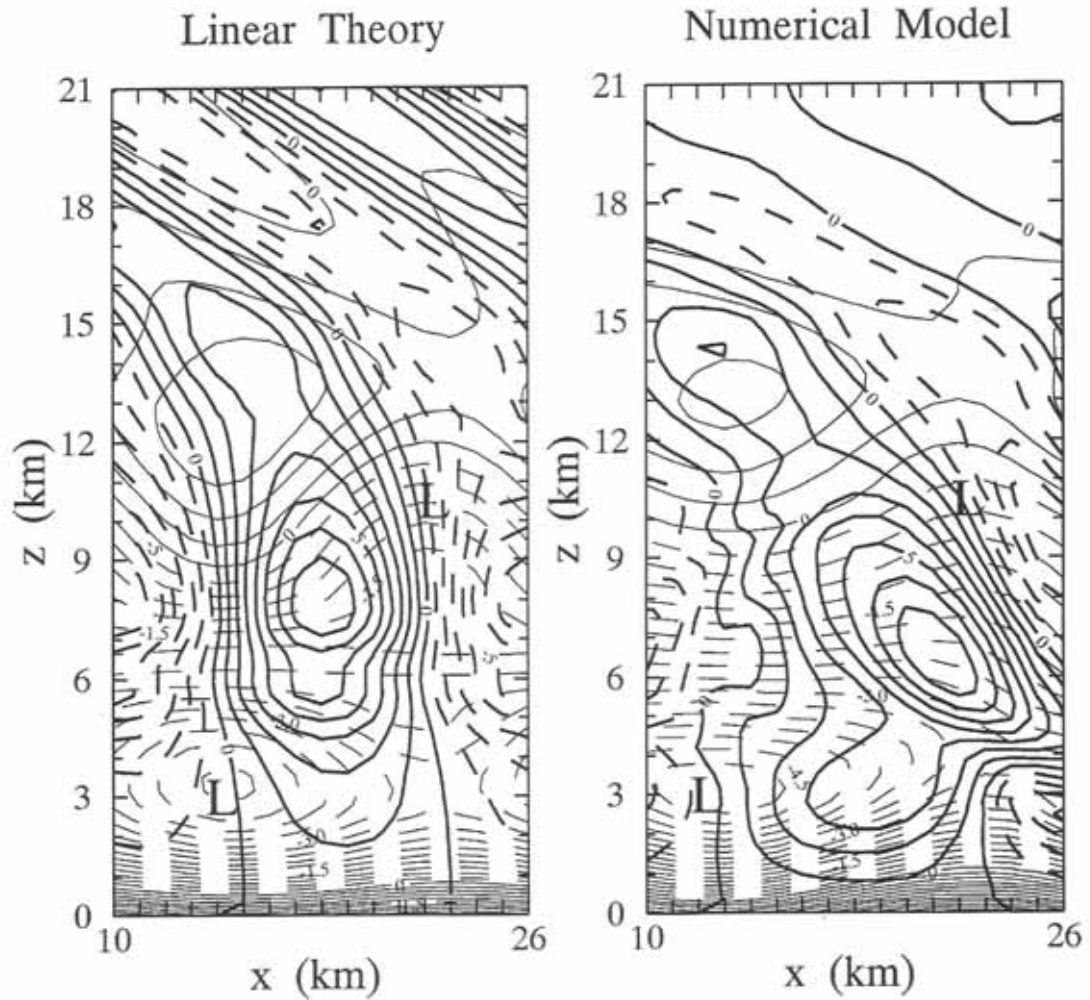
Fig. 2.22 (a) Vertical velocity (thick line) and pressure perturbation (thin line) fields predicted by linear theory and (b) determined from the 2D simulation for $x = 10$–26 km at $t = 11$ h. Contour interval is 1 m s^{-1} for vertical vecocity and 0.3 mb for pressure perturbation; the positive field is in solid lines and the negative field is dashed. A letter L denotes a region of low pressure.
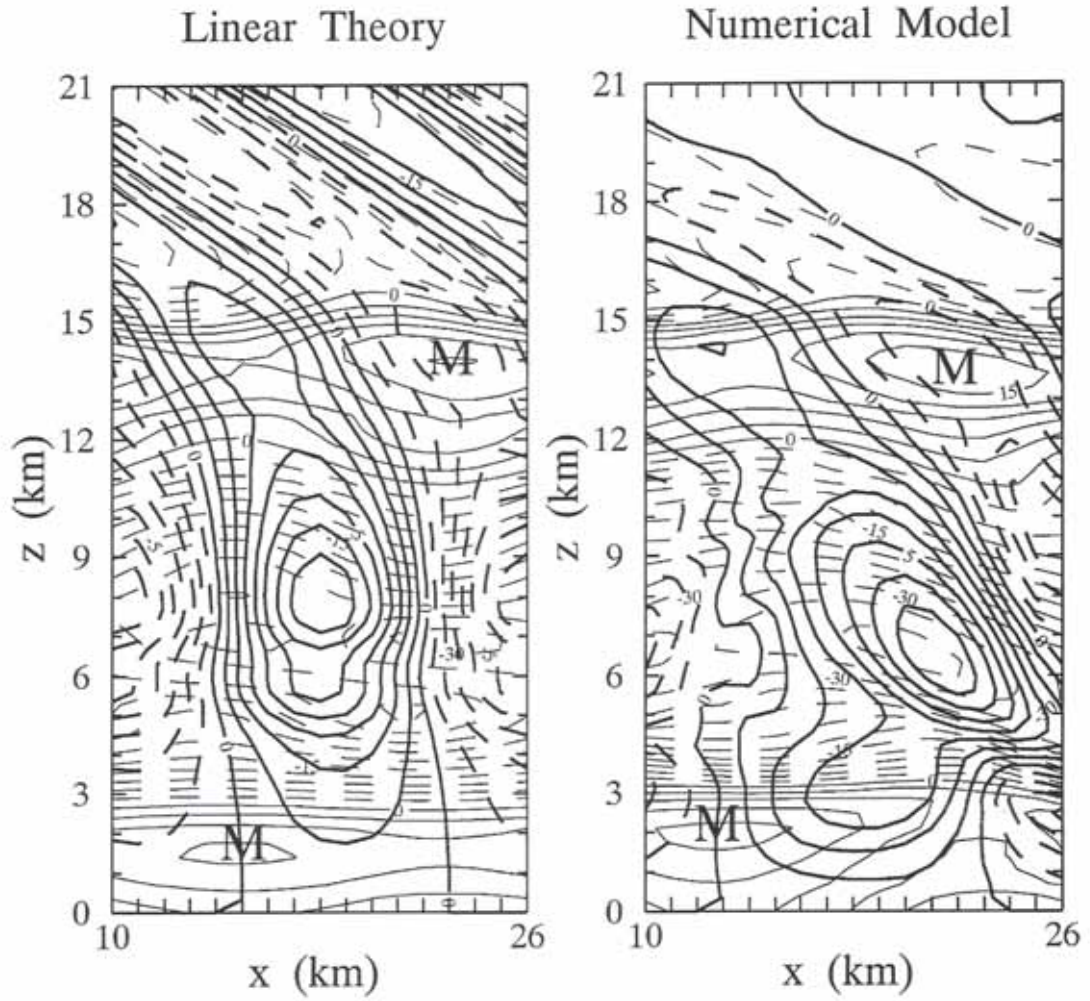
Fig. 2.23 As in Fig. 2.22 except for vertical velocity (thick line) and storm–relative horizontal wind (thin line). Contour interval is 1 m s^{-1} for vertical velocity and 3 m s^{-1} for storm–relative horizontal wind. A letter M denotes a region of horizontal wind maximum.

No Tropopause   Open Lower BC
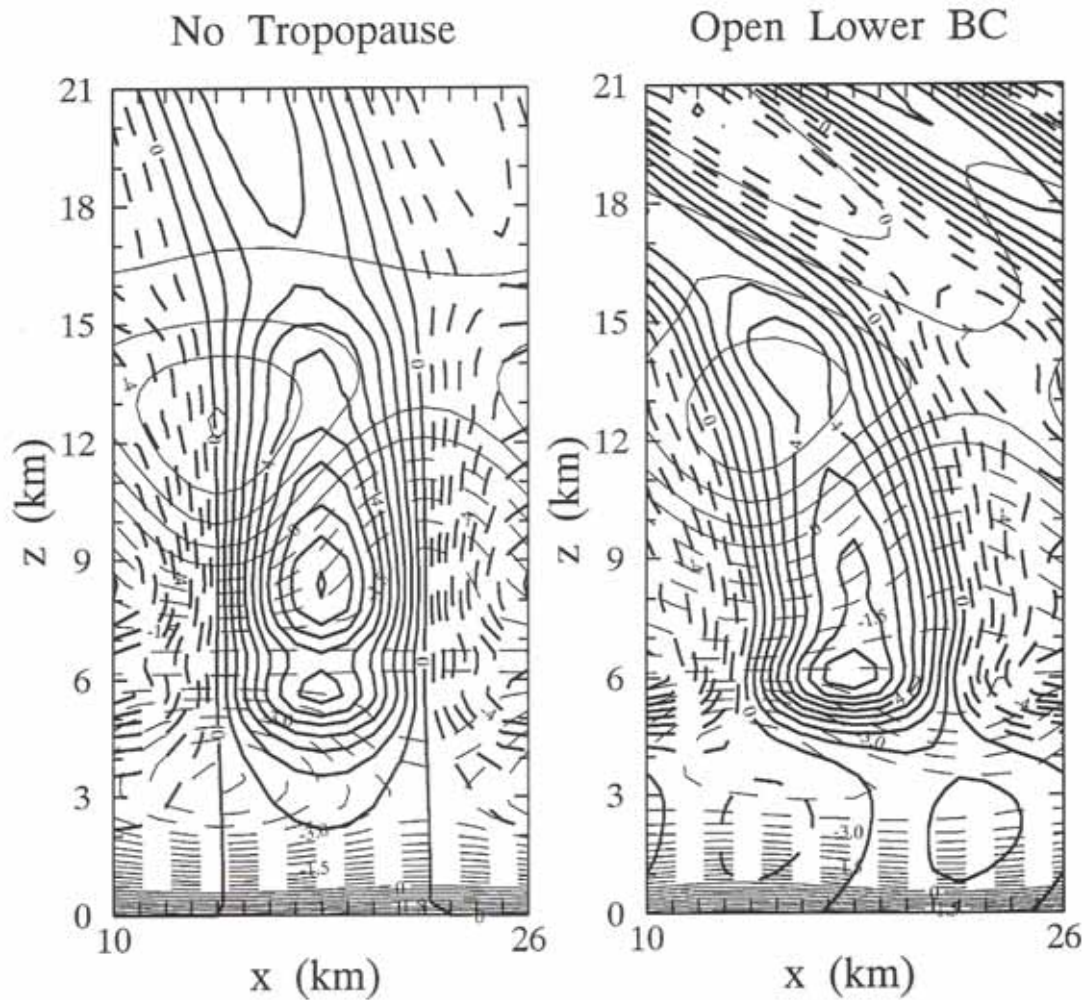
Fig. 2.24 Vertical velocity (thick line) and pressure perturbation (thin line) fields predicted by linear theory for (a) the no–tropopause case and (b) the open lower–boundary case for $x = 10$–26 km and $t = 11$ h. Contour interval is 0.8 m s^{-1} for vertical velocity and 0.3 mb for pressure perturbation; the positive field is in solid lines and the negative field is dashed.
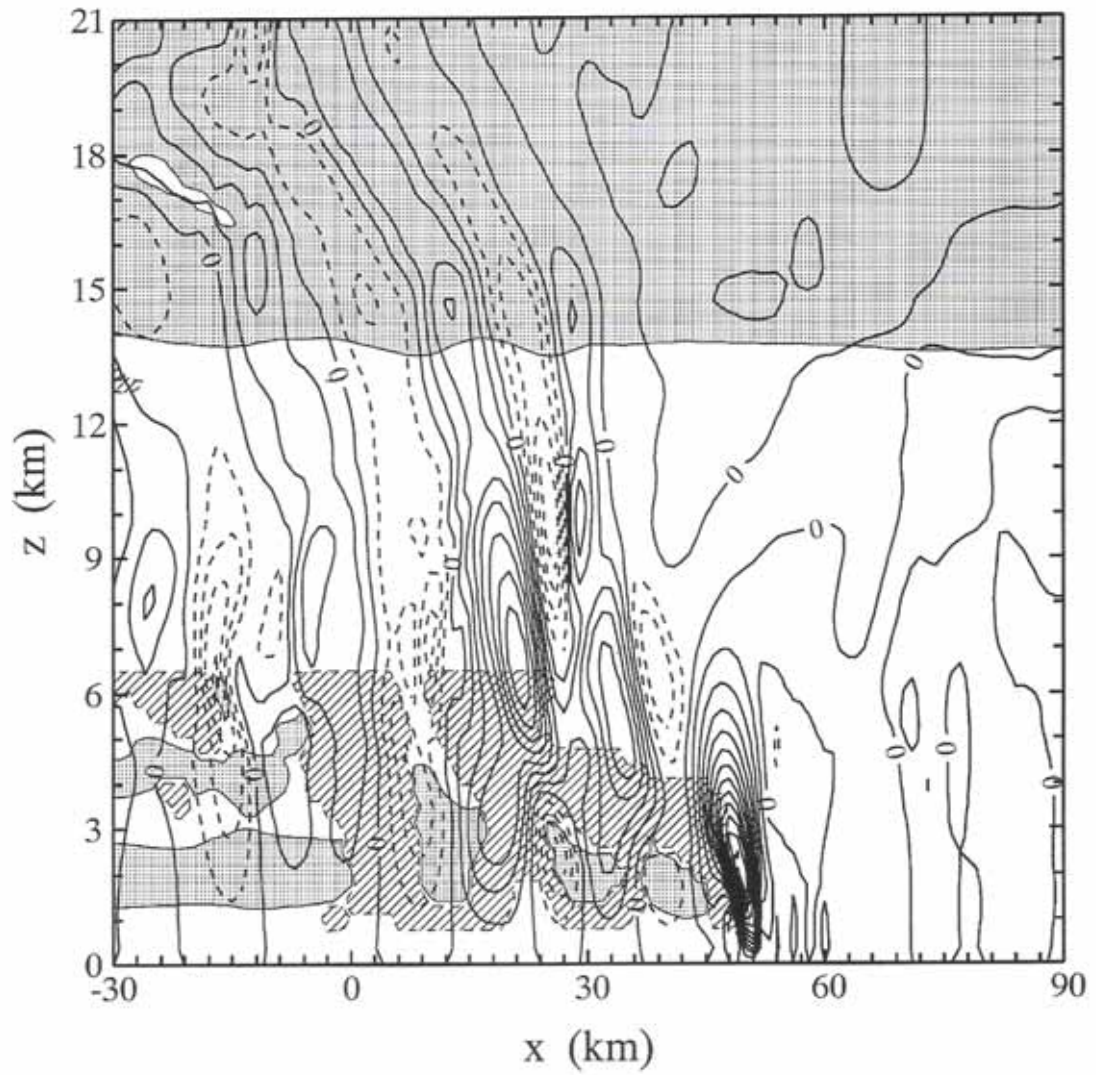
Fig. 2.25 Vertical velocity (with a contour interval of 1 m s^{-1}) and N^2 of the simulated 2D storm at $t = 11$ h. The positive field is in solid lines and the negative field is dashed. Region of $N^2 > 2 \times 10^{-4}$ s^{-2} is shaded and region of $N^2 < -0.1 \times 10^{-4}$ s^{-2} is hatched.
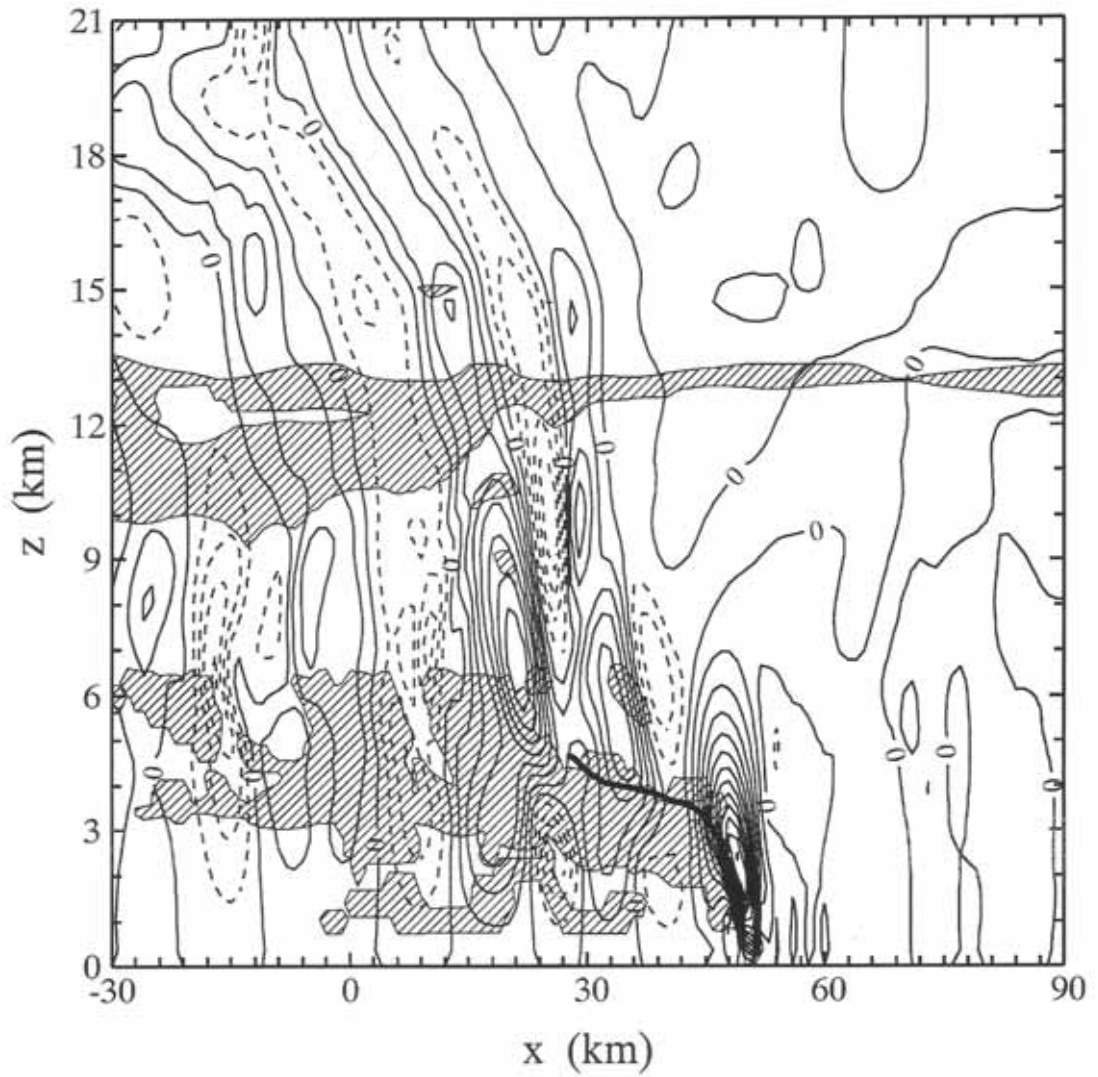
Fig. 2.26 Vertical velocity (with a contour interval of 1 m s⁻¹) and Richardson number R_i of the simulated 2D storm at $t = 11$ h. The positive field is in solid lines and the negative field is dashed. Region of $R_i < 1.0$ is hatched. Heavy outline is the critical level.
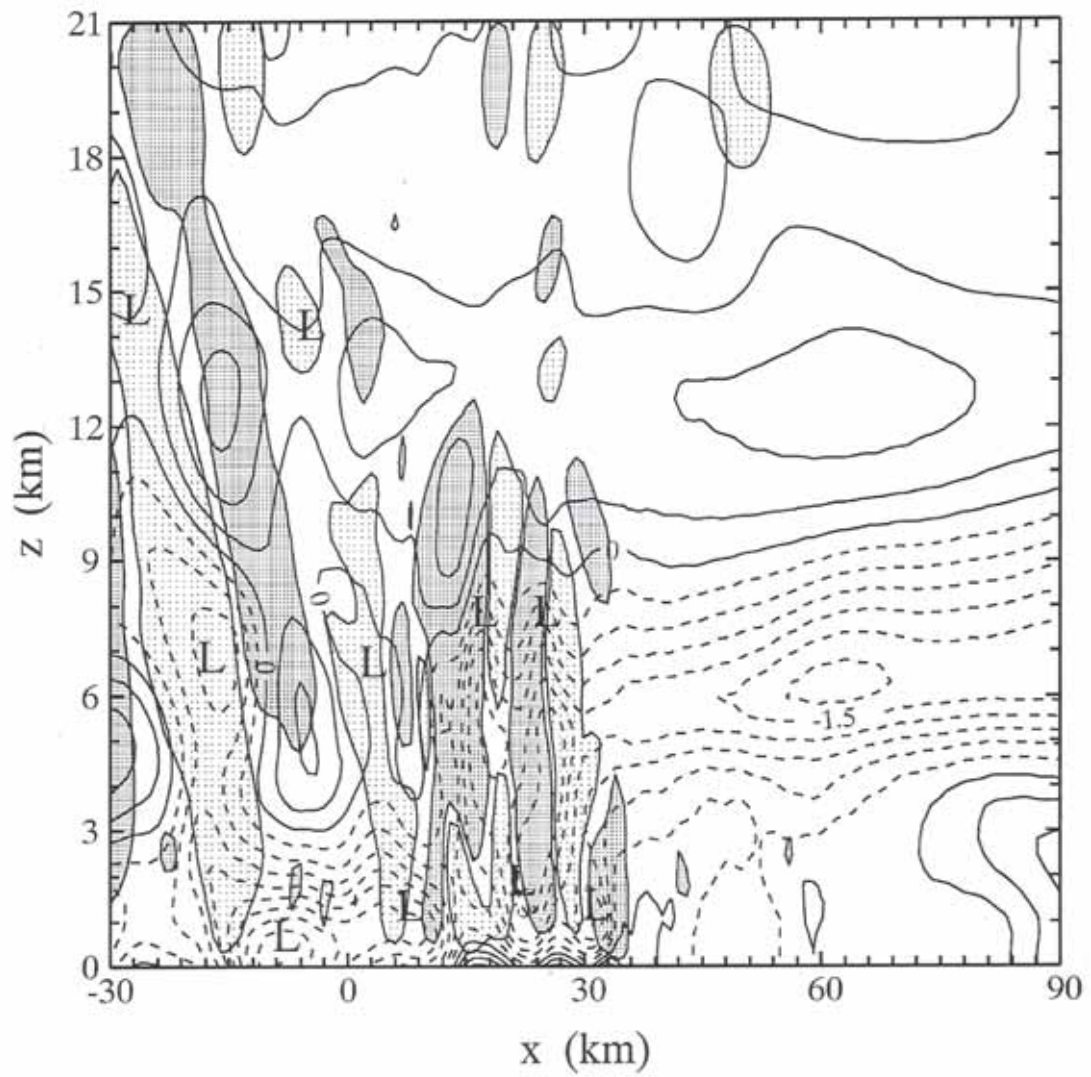
Fig. 2.27 As in Fig. 2.10 except for the NLHT run at $t = 10.5$ h. The gust front is near $x = 34$ km.
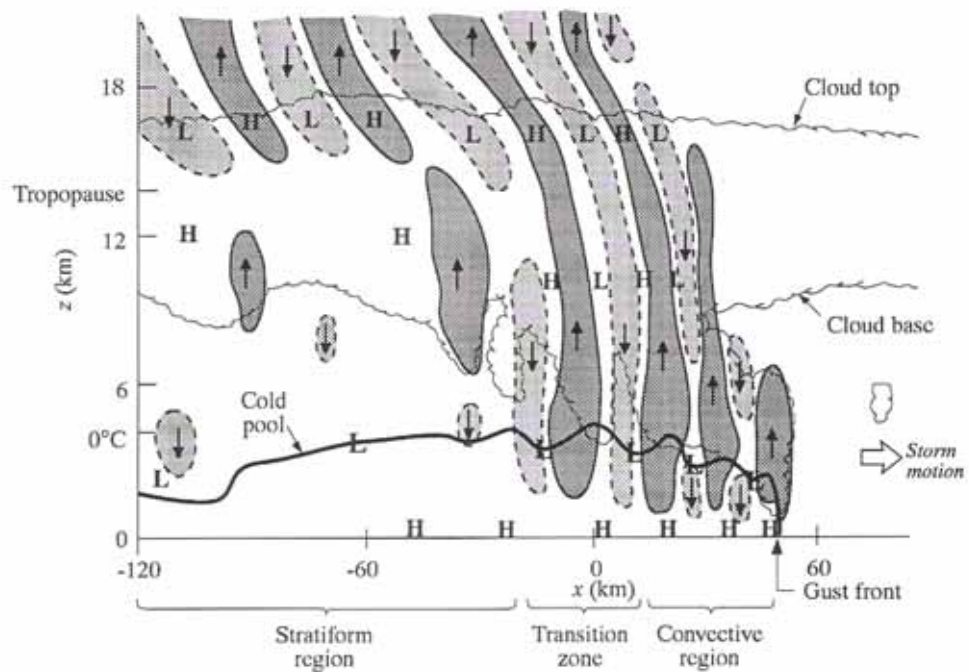
Fig. 2.28 Schematic model of the gravity–wave structure for a mature–stage multicellular squall line based on 2D simulation results at $t = 11$ h. Updraft greater than 1 m s^{-1} are heavily shaded, and downdrafts less than -1 m s^{-1} are lightly shaded. Heavy line is the cold pool outline defined by the $\theta' = -1$ K contour; cloud shield is defined by the 0.5 g kg^{-1} contour of nonprecipitating hydrometeor mixing ratio ($q_c + q_i = 0.5$ g kg^{-1}; q_c is the cloud water mixing rtatio and q_i is the cloud ice mixing ratio). A letter L or H denotes a region of low or high pressure.

CHAPTER 3

MICROPHYSICAL SENSITIVITIES OF SQUALL-LINE REAR INFLOW

3.1 Background

Squall lines with 50–200 km wide trailing-stratiform precipitation regions are an important type of organized mesoscale convective systems (MCSs), which occur in both the tropics and midlatitudes (Hamilton and Archbold 1945; Newton 1950; Fujita 1955; Pedgley 1962; Zipser 1969, 1977; Houze 1977). Doppler-radar observations have documented the detailed kinematic and precipitation structures of squall-type MCSs (e.g., Roux et al. 1984; Smull and Houze 1985, 1987a; Biggerstaff and Houze 1991a, b, 1993). Numerical modeling has confirmed these observations (Nicholls 1987; Dudhia et al. 1987; Fovell and Ogura 1988; Rotunno et al. 1988; Weisman et al. 1988; Tao and Simpson 1989; Lafore and Moncrieff 1989; Tao et al. 1993; Skamarock et al. 1994). These studies show a mesoscale storm-relative ascending front-to-rear (FTR) flow, transporting hydrometeors rearward from a leading-edge convective line to the trailing-stratiform region, and a storm-relative rear-to-front (RTF) flow, descending through the stratiform region toward low levels in the leading convective region. A conceptual model depicting these and other commonly observed features of leading-line trailing-stratiform squall lines was presented in Fig. 1.1 (from Houze et al. 1989; see also Houze 1993, Chapter 9).

Smull and Houze (1987b) characterized the observed RTF flow (or rear inflow) structure of 18 mesoscale convective systems. They suggested that a midlevel mesolow in the stratiform region (Brown 1979) might act in conjunction with a mesolow in the convective region (LeMone 1983) to establish a continuous RTF current across the storm. They further suggested that in some cases (e.g., Chong et al. 1987) rear inflow could be generated by the physical processes internal to the convective system without the aid of ambient flow entering the system.

Zhang and Gao (1989) performed mesoscale model simulations of an intense midlatitude squall line indicating that the large-scale baroclinicity provided deep and favorable RTF flow within the upper half of the troposphere. The mesoscale response to convective forcing enhanced the trailing rear inflow, and latent cooling and water loading were responsible for the descent of the rear inflow.

Fovell and Ogura (1989) and Weisman (1992) showed that the RTF flow increased in strength with increasing environmental vertical wind shear and convective available potential energy (CAPE). Using a convection-resolving cloud model, Weisman (1992) further discussed how various RTF flow structures could influence the cold-pool circulation at the leading edge of the convective system, producing a stronger or weaker storm.

Despite these previous studies, the physical processes accounting for the structure and strength of rear inflow have not been completely identified. How sensitive is the rear inflow to hydrometeor types (especially heavy hailstones versus light snow particles)? How sensitive is the rear inflow to ice-phase microphysics? How sensitive is the rear inflow to the environmental humidity? What are the crucial microphysical processes determining the rear-inflow structure? Furthermore, it has not been established whether the rear inflow is determined more by environmental factors or by physical processes internal to the storm. The objective of Chapter 3 is to answer these questions.

In Chapter 3, we use the Klemp-Wilhelmson (1978) cloud model to perform seven numerical experiments in order to determine the sensitivity of the storm structure to hydrometeor types, ice-phase microphysics, and environmental humidity. Because the 10-11 June 1985 squall line has a large horizontal extent and seven sensitivity test runs are required, only 2D simulations are carried out. The 2D simulation approach is justified since during the mature stage, the 10-11 June squall line was highly linear and symmetric in its precipitation pattern and its cross-line airflows. Most of Chapter 3 is based on Yang and Houze (1995b).

3.2 The control experiment (CNTL)

The numerical model and initial condition for the 2D model simulations are described in Section 2.2. A control run (CNTL) with full model physics for 15 h has a development pattern similar to that described by Rotunno et al. (1988). Following Fovell and Ogura (1988), we turned off the hail generation processes after 6 h. Without the generation processes, hail particles were depleted within one hour and then the only precipitating ice particle left was snow (i.e., no hail particles left after $t = 7$ h). The justification for turning off hail generation processes after the early stage is that there were very few hailstones in the mature or decaying stage of the 10-11 June squall line. Johnson

and Hamilton (1988) indicated that there were some reports of hailstones during the early stage of the 10-11 June squall line (hailfall reports from Garden City at 2210 UTC and Dodge City at 2307 UTC), but no hailfall reports were made during its mature and decaying stages (see their Fig. 7). The climatology of springtime storms in this region also indicates that hail tends to occur toward the early stages of the storms (Houze et al. 1990).

After $t = 8$ h, the simulated squall line reaches a quasi-steady state, which is realistic compared with observations. The multicellular structure has been interpreted as a gravity-wave phenomenon (Chapter 2; see also Yang and Houze 1995a).

Objective criteria are applied to divide the simulated squall line into convective and stratiform components. A "convective region" is defined as a surface precipitation region where the rainfall rate is greater than 15 mm h^{-1}, or the gradient of rainfall rate has a magnitude greater than 5 mm h^{-1} km^{-1}. A surface precipitation region that does not satisfy the criteria above is defined as the "stratiform region." These criteria are consistent with the convective-stratiform separation method applied to radar observations by Churchill and Houze (1984).

3.2.1 Overview of the storm development

Although the initial condition of the model simulation is discussed in Section 2.2, here we show again the initial temperature and wind profiles for the CNTL run in Fig. 3.1. Figure 3.2 displays the time series of the horizontally integrated rainfall rates over the convective (CV curve) and stratiform (SF curve) regions. A substantial burst of rainfall reached the ground at $t \approx 0.5$ h in response to the initial cold pool (Fig. 3.2). After the first intense rain burst, the domain-total convective rainfall became weaker and reached a somewhat steady value between 3 and 6 h. Initially ($t < 6$ h), most of the precipitation was convective. During $t = 6$–7 h, when hail generation terms were artificially turned off, convective rainfall became much weaker. After $t = 8$ h, when the simulated squall line was well developed, the convective rainfall remained roughly constant, but the stratiform rainfall increased persistently, reaching 28–36% of total rainfall in the mature stage ($t = 10$–11 h) and 45–53% of the total rainfall by the end of simulation ($t = 14$–15 h). The stratiform contribution (28–36%) to total rainfall during the mature stage is in agreement with observational estimates 29% of Johnson and Hamilton (1988) and 35–45% of Braun and Houze (1995c; see their Fig. 3b).

Figures 3.3a–c show the surface rainfall rate over three one-hour periods (7.5–8.5 h, 10–11 h, 12.5–13.5 h) representing three stages of storm development: developing or initial (INI), mature (MAT), and slowly decaying (DEC). The simulated storm did not actually die before the end of integration (15 h), probably because of the constant convectively favorable conditions in the prestorm environment. However, after the mature stage (t = 10–11 h), the storm did show a slow trend of weakening or decay. During the early time (Fig. 3.3a), the trailing stratiform region had just begun to develop and was very narrow. During the mature stage (Fig. 3.3b), surface rainfall in the convective region reached its maximum intensity, and there was a broad and relatively uniform stratiform precipitation region behind the leading-edge convective line. As the system aged (Fig. 3.3c), the convective rainfall became less intense, and the trailing stratiform precipitation region broadened further. The evolution of surface precipitation from one stage to the next can also be seen in Fig. 3.3d, which shows the one-hour-averaged rainfall rates over these three periods. The secondary band of enhanced stratiform precipitation (discussed by Biggerstaff and Houze 1991a, 1993; Braun and Houze 1994a) in the stratiform region shows up clearly in Fig. 3.3d, and it is most evident during the mature and slowly decaying stages.

In order to highlight the mesoscale circulations and their associated storm structures, time averaging is applied to the 2-min model output fields over the three one-hour periods. Thus transient, small-scale fluctuations are smoothed out, and only more steady mesoscale signatures are left. In Figs. 3.4–3.7, all fields are displayed in a storm-relative coordinate such that the gust front is fixed at x = 0 km. The cloudy region is shaded and the storm precipitation boundary is highlighted. The cloudy region is defined as the region with a one-hour-averaged nonprecipitating hydrometeor (cloud water and cloud ice) mixing ratio greater than 0.1 g kg^{-1}. The storm precipitation boundary is defined by the contour of one-hour-averaged radar reflectivity of 15 dBZ; radar reflectivity is calculated from mixing ratio fields of precipitation hydrometeors according to equation (1) of Fovell and Ogura (1988). Storm propagation speeds are 9.4 m s^{-1} in the initial stage (t = 7.5–8.5 h), 12.2 m s^{-1} during the mature stage (t = 10–11 h), and 12 m s^{-1} in the slowly decaying stage (t = 12.5 –13.5 h). The fastest storm propagation speed is 13.8 m s^{-1} around t = 10 h, which matches the observed squall-line propagation speed of about 14 m s^{-1} (Zhang et al. 1989; Biggerstaff and Houze 1991a).

3.2.2 Evolution of the squall line structure

In Section 2.3.1 (see also Yang and Houze 1995a), we showed that the basic features of the full-physics CNTL run agreed well with the dual-Doppler radar analysis of Biggerstaff and Houze (1993). We now examine the evolution of the simulated squall-line structure by reference to Figs. 3.4–3.7.

1) KINEMATIC STRUCTURE

Figure 3.4 shows the evolution of the storm-relative horizontal wind field. Initially (Fig. 3.4a), there was strong inflow in the boundary layer ahead of the system, weaker and drier inflow at midlevels, and strong outflow at upper levels. A mid-to-upper level ascending FTR flow dominated inside the cloud (shaded region). Behind the cloud was a low-to-mid level descending RTF flow. Underneath the midlevel RTF flow behind the system was a low-level FTR outflow.

As the storm matured, the ascending FTR flow became stronger, broader, and more horizontally oriented (Fig. 3.4b). The divergence center near cloud top drifted further rearward. The descending RTF flow became more organized with a pronounced double-core structure. One RTF maximum was at low levels within and behind the convective region. The other was near the melting level ($z = 4$ km) at the back edge of the storm ($x = -150$ to -120 km). It developed later than the first RTF maximum, consistent with observations (Smull and Houze 1987b; Rutledge et al. 1988). Lafore and Moncrieff (1989) and Weisman (1992) interpret the enhanced RTF flow at the rear of the stratiform precipitation in terms of the horizontal buoyancy gradients along the back edge of the storm that generate two counter-rotating horizontal vortices, concentrating the flow from the rear of the system into the storm at midlevels (see Fig. 2c in Weisman 1992). The rear inflow plays a crucial role in supplying potentially cold and dry midlevel air from the environment to aid in the production of the convective and mesoscale downdrafts. Different orientation of the rear inflows (descending or elevated) can increase or decrease the leading-edge updraft and the storm strength, by producing different sign of additional vorticity source in the horizontal-vorticity balance near the gust front (see Weisman 1992 for details).

The simulated maximum of FTR flow in the mature stage (30 m s^{-1}) is stronger than the observed one (20–25 m s^{-1}; see Fig. 2.7b), which might be partly an effect of the enhanced horizontal mass divergence by the imposed 2D geometry (Fovell and Ogura

1988). On the other hand, the simulated maximum of RTF flow at the back edge of the storm only reaches half of the observed strength (8 m s^{-1} vs. 15 m s^{-1}) during the mature stage, which might be a result of neglecting the background baroclinicity (Zhang and Gao 1989; Braun 1995) and/or the enhanced mass convergence associated with vortices on both ends of a fully three-dimensional squall line (see Fig. 10 of Skamarock et al. 1994). By the late stage, both the FTR and RTF flows were mostly horizontally oriented (Fig. 3.4c).

Initially, intense convective updrafts occurred at the leading edge, dynamically induced upper-level downdrafts surrounded the intense upper-level updraft as a result of mass compensation (Houze 1993, pp. 223–226), and precipitation-induced downdrafts were located in low levels (Fig. 3.5a). Vertical motion was generally weak in the stratiform precipitation region ($x = -60$ to -30 km).

As the storm matured, there were two main updrafts in the convective region ($x = -30$ to 0 km in Fig. 3.5b). At the leading edge, a low-level updraft was persistently forced by the strong convergence near the gust front. About 20 km behind the gust front, a midlevel updraft was a free convective updraft associated with the release of the latent heat of condensation. The transient low-level convective downdrafts are largely smoothed out by the one-hour time average. In the trailing-stratiform region, weak ascent occurred at upper levels above a region of weak descent ($x = -140$ to -50 km in Fig. 3.5b). These regions of upper-level ascent and lower-level descent in the stratiform region are often referred to as the mesoscale updraft and mesoscale downdraft in this type of storm (e.g., Houze 1989). The mesoscale updraft/downdraft configuration agrees well with the along-line averaged vertical velocity field from the dual-Doppler radar composite analysis (Fig. 2.8b), which was taken for a portion of the storm where both the radar reflectivity and horizontal flows appeared to be the most nearly two-dimensional (see Fig. 3a of Biggerstaff and Houze 1993). In particular, the simulated mesoscale descent sloped downward toward the leading-edge of the storm, consistent with the dual-Doppler radar analysis (Fig. 2.8b). The mesoscale updraft (taken to be the broad region of $w > 0.5$ m s^{-1} at $x = -130$ to -50 km in Fig. 3.5b) was ahead of the mesoscale downdraft (the broad region of $w < -0.5$ m s^{-1} at $x = -170$ to -90 km in Fig. 3.5b) in the trailing-stratiform region, which was also found in the Doppler radar analysis. Both mesoscale ascent and descent had similar peak magnitudes (1.1 m s^{-1} for mesoscale ascent, -0.9 m s^{-1} for

mesoscale descent) and sizes (80-km wide for mesoscale ascent, 85-km wide for mesoscale descent).

The level of zero vertical velocity roughly corresponded to the stratiform cloud base. The FTR/RTF flow interface (Fig. 3.4) had a horizontal orientation similar to that of the mesoscale updraft/downdraft interface (Fig. 3.5); however, it was at a slightly lower altitude than the mesoscale updraft/downdraft interface. A weak mid-to-upper level downdraft (-0.3 to -0.2 m s^{-1}) was located in the transition zone ($x = -50$ to -20 km), although it does not show up clearly in the contour levels chosen for the figure. This transition-zone downdraft was also seen in the radar data (Biggerstaff and Houze 1993; Braun and Houze 1994a).

By the late stage (Fig. 3.5c), mesoscale ascent and descent were weaker in the expanding stratiform region. The maximum of the RTF flow at the back edge of the stratiform precipitation (Fig. 3.4) was collocated with the strongest mesoscale downdraft (Fig. 3.5) and the FTR/RTF flow interface still had an orientation similar to that of the mesoscale updraft/downdraft interface, indicating that the mass convergence associated with the ascending FTR flow and descending RTF flow in the trailing-stratiform region was crucial to the generation and maintenance of mesoscale updraft and downdraft. The mid-to-upper level downdraft in the transition zone ($x = 30$ to 45 km in Fig. 3.5c) was, however, stronger (-0.5 to -0.2 m s^{-1}).

2) THERMAL AND PRESSURE STRUCTURE

In the early stage of the storm (Fig. 3.6a), the potential temperature perturbation field (deviation from its initial value) indicated a warm plume of air produced in mid-to-upper levels by the release of latent heat within the storm. This warm anomaly extended across the stratiform and rear anvil region. A second warm anomaly occurred below the rear anvil cloud at about 3 km altitude. It resulted from an adiabatic temperature increase in the unsaturated descent of the mesoscale downdraft air (Zipser 1977; Johnson and Hamilton 1988). A low-level precipitation-induced cold pool was produced by latent cooling of evaporation and melting associated with precipitation. Stretching rearward from the back edge of the cold pool head, a midlevel cold tongue ($\theta' < 1$ K) was formed by the sublimational cooling of snow particles.

As the system matured, the midlevel warm anomalies broadened and intensified (Fig. 3.6b). The cold pool head was wider, deeper, and stronger (minimum surface θ' reached -10 K). The adiabatic warming in the mesoscale downdraft had produced a stronger warm anomaly above the back edge of the cold pool head ($z = 4$ to 5 km, $x = -150$ to -120 km). By the late stage (Fig. 3.6c), the system had continued to broaden; however, the cold pool was weaker (minimum surface θ' was -9 K) in association with weaker convective activity during the slowly decaying stage.

The pressure perturbation field (deviations from initial values) in Fig. 3.7a shows a meso-γ-scale[1] low in the convective region, just behind the convective updraft at $z = 3$ km. It was hydrostatically generated as a result of the slope of warm convective updrafts (LeMone 1983; Fovell and Ogura 1988; Braun and Houze 1994a). Near the surface, there was a dynamically generated high pressure at the gust front (Fovell and Ogura 1988; Houze 1993, pp. 364–365; Szeto and Cho 1994).

An important feature for the momentum budget (to be discussed in Chapter 4) is the meso-γ-scale low pressure center at $z \approx 3$ to 4 km, $x \approx 0$ to 20 km in each panels of Fig. 3.7. This low broadens and intensifies as the system progresses from the early (Fig. 3.7a) to mature stage (Fig. 3.7b). This broadening and intensification of the low pressure corresponds to the amount of anomalously warm air above the low which increases during this period (Figs. 3.6a–b). This low pressure center continues to broaden into the weakening stage of the storm (Fig. 3.7c). The horizontal gradient of pressure associated with this small-scale low pressure affects the momentum budget of the storm (Section 4.3) by accelerating air in the convective region rearward and air in the stratiform region forward.

The surface high pressure near the gust front reached its maximum strength ($p' = 2.4$ mb) during the mature stage of the storm (Fig. 3.7b). The horizontal pressure-gradient force associated with this high pressure accelerated air rearward in the boundary layer in the stratiform region of the storm (previewing Fig. 4.4 b). The stratiform region also had a broad zone of high pressure near the storm top. The horizontal gradient of pressure associated with this high also had a strong effect on the storm's momentum budget (Section 4.3) at upper levels. By previewing Fig. 4.13, we see that at upper levels the pressure-gradient force in the stratiform region was strongly RTF.

---

[1]Meso-γ-scale is defined by Orlanski (1975) as a horizontal dimension of 2–20 km.

The mesolow in the stratiform region (Fig. 3.7b) was collocated with the maximum of RTF flow at the back edge of the stratiform precipitation region (see Fig. 3.4b), thus supporting the argument of Smull and Houze (1987b) that the resulting horizontal pressure-gradient force associated with the mesolow drew midlevel air into the storm from the rear to induce the rear inflow. A weak surface wake low produced by subsidence warming of the descending rear inflow was located at the back edge of the stratiform precipitation region (x = −150 km), but it was not as evident as was observed (Johnson and Hamilton 1988).

The pressure perturbation field in the late stage of the storm (Fig. 3.7c) was similar to that in the mature stage (Fig. 3.7b). The meso-γ-scale low pressure in the convective region remained strong; however, the gust-front high pressure weakened (Fig. 3.7c).

3.2.3 Latent heating fields

Figure 3.8 shows the latent heating and cooling fields averaged during the mature stage (t = 10–11 h) of the full physics CNTL run. Figure 3.8a is the total latent heating field, which shows heating in the cloudy region (strongest in the convective region) and cooling in the subcloud region (strongest in the trailing-stratiform region). Most of the latent heating in the cloudy region was produced by condensation of cloud water (Fig. 3.8b). Riming warming associated with accretion of cloud and rain droplets by snow particles occurred mostly in the convective region and also in the leading part of the stratiform region (Fig. 3.8c). Warming associated with depositional growth of snow occurred throughout most of the stratiform cloud region (Fig. 3.8d). Homogeneous freezing of cloud water into cloud ice (not shown) occurred only at upper levels and contributed very little to the total latent heating field.

Strong sublimational cooling occurred below the base of the trailing anvil cloud. This cooling is consistent with the hypothesis of Rutledge et al. (1988) that sublimational cooling of snow particles first drives the rear inflow to descend (see Fig. 3.4b and Fig. 3.8d) and penetrate through the storm. Melting of falling snow particles (Fig. 3.8e) further enhanced the cooling near 0°C level (z = 4 km) and strengthened (but did not initiate) the mesoscale downdrafts (details in Section 3.3.4). Most of the latent cooling in the subcloud region was produced by evaporation of rainwater (Fig. 3.8f). Evaporation was the most important microphysical process driving the descending rear inflow (details in Section 3.3.3).

3.2.4 Air parcel trajectories

Figures 3.9a-c show the one-hour air-parcel trajectories ($t = 10$–11 h) calculated backward by the method of Doty and Perkey (1993) from model-generated wind fields at 2-min intervals. All trajectories are displayed in a storm-relative coordinate, in which the gust front is fixed at $x = 0$ km. The equivalent potential temperature θ_e along the air-parcel trajectories is nearly conserved outside the convective region ($x = -30$ to 0 km). The maximum difference of θ_e along the trajectories is less than 2 K in the convective region.

Fifty-one air-parcel trajectories ending in the broad mesoscale ascent region in the stratiform region (corresponding to $w > 0.5$ m s^{-1} at $x = -130$ to -50 km, $z = 7$ to 12 km in Fig. 3.5b) show that most of the air within the mesoscale ascent came from the high-θ_e boundary layer ahead of the system (Fig. 3.9a). Some air parcels were from the prestorm low-θ_e layer at midlevels, and a very few were from the upper levels of the transition zone.

A total of 102 trajectories in the mesoscale descent region (corresponding to $w < -0.5$ m s^{-1} at $x = -170$ to -90 km, $z = 1$ to 6 km in Fig. 3.5b) determines the source of the descending air (Fig. 3.9b). Unlike the results of Tao and Simpson (1989), which indicated that some parts of mesoscale downdrafts originated in the rotor circulation within the cold pool head, air-parcel trajectories in Figs. 3.9b and 3.9c show the mesoscale descent in the stratiform region to be distinct from the rotor circulation. Figure 3.9b shows that air parcels in the forward part of mesoscale descent region were from the middle levels in the convective region, and those in the rear part of mesoscale descent region came from the poststorm low-θ_e layer at midlevels. A 3-h ($t = 9$–12 h) forward trajectory analysis for air parcels in the rear inflow at the back edge of the stratiform precipitation indicates that a substantial portion of air parcels in the rear inflow descends and reaches low levels in the convective region (not shown).

Figure 3.9c clearly shows the rotor circulation within the head of the cold pool. Some of the air within the leading portion of the cold pool originated from the stratiform region. It entered the storm as part of the descending RTF flow from the low-θ_e layer at midlevels behind the system. Some of the air within the rotor circulation was from the low-θ_e midlevel ahead of the system, which indicates a crossover zone in the convective region (Zipser 1977; Redelsperger and Lafore 1988; Houze 1993, pp. 363–367).

3.2.5 Trajectories of precipitation particles

Figure 3.10 displays one-hour forward-computed trajectories ($t = 10$–11 h) of precipitation particles starting from different vertical levels in the transition zone during the mature stage ($x = 10$ km in Fig. 3.5b). Hydrometeors are assumed to fall at their mass-weighted mean terminal velocities, which depend on time-variant amounts of hydrometeors (rain and/or snow) at each grid point. Precipitation particles falling to the surface in the transition zone were from the low levels of the convective region, while those falling to the surface in the stratiform region were from the middle to upper levels of the convective region. These findings are consistent with the results of Biggerstaff and Houze (1993) and Braun and Houze (1994a).

3.3 Sensitivity tests

Six numerical experiments (see Table 3.1) are performed to determine the sensitivity of the storm structure, with emphasis on rear inflow, to hydrometeor types, ice microphysics, and environmental humidity. We compare these results with those of the full-physics CNTL run. To facilitate the comparisons of these numerical experiments with the full-physics CNTL run, Figure 3.11 is obtained by grouping Figs. 3.4b, 3.5b, and 3.6b into a separate figure to highlight the mature-stage structure of the CNTL run.

3.3.1 Hail storm simulation (HAIL)

The experiment HAIL is the same as the CNTL run except that hail generation terms are not turned off after 6 h (i.e., allowing heavy hailstones to occur during the mature and slowly decaying stages). Owing to the large fall speeds of hail particles (10–40 m s^{-1}; see Section 2.2.2), hydrometeors fall out quickly, before they can be transported very far behind the convective line by FTR flows; therefore, the surface precipitation region is much narrower (60 km in Fig. 3.12 vs. 130 km in Fig. 3.11) during the mature stage ($t = 10$–11h).

With the occurrence of hailstones, the multicellular structure is very pronounced in the vertical velocity field (Fig. 3.12b), even after the one-hour averaging. Neither the broad mesoscale updraft/downdraft nor the upper-level transition-zone downdraft occur in the HAIL storm during the mature stage. The subcloud cold pool (Fig. 3.12c) remains approximately the same strength (minimum surface θ' is -10 K). However, the cold pool

head of the HAIL storm is much narrower (55 km wide in Fig. 3.12c vs. 150 km wide in Fig. 3.11c), because the heavier hydrometeors fall out too quickly to be transported far away from the convective region. The cooling by evaporation and melting associated with these hail particles thus occurs closer to the convective region and leads to a narrower cold pool head.

The ascending FTR flow is slightly weaker and more vertically oriented (Fig. 3.12a). The descending RTF flow shows only one maximum—in the convective region. A second maximum of RTF flow does not occur at the back edge of the storm, as in the CNTL storm (Fig. 3.11a), because the horizontal pressure gradient associated with the midlevel mesolow in the stratiform region is too weak to generate a RTF wind maximum as a result of weaker buoyancy gradient at the rear of the system (Fig. 3.12c).

When heavy hailstones are not present during the mature stage (like the CNTL run; the only precipitating ice particles are snow particles), hydrometeors are transported further back of the leading convective line to form a wider storm, in which mesoscale ascent and descent appear clearly (Fig. 3.11b). Then the thermal structure, modified by diabatic heating/cooling over a larger region, hydrostatically generates a midlevel mesolow in the trailing-stratiform region to support the formation of the rear inflow. Similar results were also found in Fovell and Ogura (1988) and Tao et al. (1991). Therefore, we conclude that *the realistic structure of the simulated descending rear inflow, at least for the 10-11 June 1985 squall line, is sensitive to the assumed hydrometeor types, which affect the kinematic structure of the storm through their fallout pattern and the subsequent effects of diabatic processes on the thermal and pressure fields.*

3.3.2 No ice-phase microphysics (NICE)

To determine the overall effects of ice microphysics on the storm structure, we exclude the ice-phase microphysics. In this run called NICE, the simulated storm propagates more slowly (storm propagation speed is 8 m s^{-1} vs. 12.2 m s^{-1}) during the mature stage ($t = 10$–11 h), but it has a more distinct multicellular behavior. After $t = 4$ h, the NICE storm reaches a "quasi-equilibrium" state (Fovell and Ogura 1988) in which convective cells are periodically generated at the leading edge with a period of 14–15 min. The mature-stage NICE storm structure (in Fig. 3.13) resembles the initial-stage structure of the full-physics CNTL storm (panel a of Figs. 3.4–3.7). In particular, the horizontally

uniform stratiform precipitation seen in CNTL during the mature and slowly decaying stages (Figs. 3.3b and 3.3c), which is mainly produced by the rearward transport, fallout, and melting of snow particles, is absent in the NICE run. Hence, the NICE storm can only capture (qualitatively) the precipitation structure within the convective region to some extent, but not the realistic stratiform precipitation region.

The vertical velocity field (Fig. 3.13b) displays a cellular structure, even after the one-hour time averaging. However, the mesoscale updraft/downdraft is not as broad and uniform as that in the CNTL run (Fig. 3.11b) and in observations (Fig. 2.8b), and the upper-level transition-zone downdraft is absent in the NICE run. The leading-edge updraft of the NICE storm has a magnitude of 7 m s^{-1}, about 30% weaker than that (10.5 m s^{-1}) of the CNTL storm. The midlevel warm anomaly is much weaker (4 K in Fig. 3.13c vs. 7 K in Fig. 3.11c), and the subcloud cold pool head is much narrower (60 km wide vs. 150 km wide). These facts indicate that *ice microphysics have both a qualitative and quantitative impact on the storm structure, including the convective region.* The cold pool is only a little weaker (minimum surface θ' is -9 K vs. -10 K); it is dominated by the evaporative cooling of rainwater in the convective region, which is still present in the NICE run.

The ascending FTR flow is somewhat weaker (-27 m s^{-1} in Fig. 3.13a vs. -30 m s^{-1} in Fig. 3.11a) and more vertically oriented. The descending RTF flow shows only one maximum (located at $x = -60$ to -20 km) within a much narrower storm (surface precipitation region is 60 km wide compared to 150 km wide), although its strength is greater than in the ice-on CNTL run (12 m s^{-1} vs. 9 m s^{-1}) as indicated by Chin (1994). When ice microphysics are included (see the CNTL run in Fig. 3.11a), the layer of RTF flow has two maxima, one of which occurs at the back edge of the stratiform precipitation as indicated in radar analysis (Fig. 2.7b; see also Biggerstaff and Houze 1993). However, this feature is absent in the NICE run. Therefore, we conclude that *ice-phase microphysics are essential to the realistic structure of the descending RTF flow.*

3.3.3 No evaporative cooling (NEVP)

The experiment NEVP is the same as the CNTL run except that air is not cooled when raindrops evaporate (latent cooling by evaporation is set to zero). In order to speed up the simulation, the NEVP run restarts from the history file of the CNTL storm saved at t = 3 h. Without the latent cooling of evaporation, the NEVP storm moves very slowly,

about 4–8 m s^{-1} slower than the CNTL storm. During the time period $t = 10$–11 h, the NEVP storm moves at a speed of 5 m s^{-1} versus 12 m s^{-1} of the CNTL storm.

This simulation is completely unrealistic. The results are thus quite different from that of the CNTL storm. The storm never develops an upshear tilt. As discussed in Zhang and Gao (1989), the persistently upright to downshear-tilted orientation of the NEVP storm indicates the significant effects of evaporative cooling. Without the evaporative cooling, there is no subcloud cool pool (Fig. 3.14c), and the system fails to show a substantial upshear tilt during the time period $t = 10$–11 h as in the CNTL run. This behavior is consistent with the theory of Rotunno et al. (1988) that the vorticity generation by the cold pool is required to overcome the vorticity associated with the environmental low-level wind shear in order for the storm to become tilted upshear.

Because of the upright to downshear-tilted system orientation, the stratiform precipitation does not trail behind the convective region but rather occurs ahead of the convective region. There is no mesoscale ascent or descent (Fig. 3.14b). Owing to the lack of upshear tilt of the convection, there is no midlevel mesolow behind the convective region (see Fig. 3.18a); as a result, the mid-to-upper level FTR flow transporting hydrometeors rearward is absent (Fig. 3.14a). The RTF flow is elevated and entirely a consequence of strong midlevel winds in the large-scale environment overtaking and entering the storm. This NEVP sensitivity test thus supports the argument of Smull and Houze (1987b) that *the descending rear inflow develops in response to dynamical and microphysical feedbacks in the trailing-stratiform region*. With no trailing-stratiform region, the rear inflow in the NEVP storm does not descend and penetrate through the storm but remains elevated across the system.

3.3.4 No latent cooling by melting (NMLT)

The experiment NMLT is the same as the CNTL run except that air is not cooled when ice particles melt (latent cooling by melting is set to zero). Like the NEVP run, the NMLT simulation restarts from the history file of the CNTL run saved at $t = 3$ h. The NMLT storm generally propagates at a speed 1–2 m s^{-1} slower than the CNTL storm; however, the speed difference becomes smaller once the system becomes well developed (speed difference is only 0.2 m s^{-1} during the time period $t = 10$–11 h). The evolution of the NMLT storm is similar to the CNTL storm, although the NMLT storm reaches its

mature stage slightly (0.5–1 h) later than the CNTL storm. Figure 3.15 shows the one-hour-average storm structure during the mature stage ($t = 10$–11 h). Although the melting cooling is turned off everywhere in the NMLT run, its simulation result is very similar to the result where melting cooling is turned off only in the stratiform region (not shown), since the dominant melting cooling process occurs in the trailing stratiform region (Fig. 3.8e).

Without the latent cooling by melting, the FTR flow (Fig. 3.15a) is much weaker (–24 m s^{-1} vs. –30 m s^{-1}) and more vertically oriented. The double core structure of the RTF flow is well preserved in the NMLT run; however, its strength is less than in the CNTL run. This result demonstrates that cooling by melting is not the cause of the rear inflow; however, the weaker rear-edge maximum of RTF flow in the NMLT run (6 m s^{-1} in Fig. 3.15a vs. 8 m s^{-1} in Fig. 3.11a) indicates that *the latent cooling by melting accounts for at least 25% of the intensity of the local maximum of RTF flow at the rear of the storm during the mature stage.* The effect of melting on the stratiform-region RTF flow was suggested by Smull and Houze (1987b) and Rutledge et al. (1988), but it has not been demonstrated *quantitatively* before.

The updrafts at the leading edge of the NMLT storm are more upright (Fig. 3.15b) than in CNTL (Fig. 3.11b). The mid-to-upper level updrafts in the convective region are stronger, but the low-level updrafts near the gust front head are weaker. Tao et al. (1995) obtained similar results. The maximum of the 1-h mean mesoscale ascent in the trailing-stratiform region of the NMLT storm is somewhat stronger (1.3 m s^{-1} vs. 1.1 m s^{-1}) but the mesoscale ascent occurs in a narrower zone (area covered by updrafts greater than 0.5 m s^{-1} is 30 km wide vs. 60 km wide). Without the latent cooling by melting, the mesoscale downward motion in the trailing-stratiform region is 22% weaker (–0.7 m s^{-1} versus –0.9 m s^{-1}) and 33% narrower (area covered by downdrafts less than –0.5 m s^{-1} is 40 km wide vs. 60 km wide). This NMLT sensitivity test then clearly shows that *cooling due to melting does not initiate the mesoscale downdrafts in the model storm, as suggested by Leary and Houze (1979); however, the melting significantly enhances the mesoscale downdrafts.* Corresponding to weaker mesoscale descent, the region of subsidence warming at the back edge of the NMLT storm (near $x = -95$ km in Fig. 3.15c) is 33% narrower (the packet of subsidence-warmed air defined by the $\theta' = 3$ K contour line near $z = 4$ km is 40 km wide vs. 60 km wide).

3.3.5 No latent cooling by sublimation (NSUB)

For the NSUB experiment, air is not cooled in the process of sublimation (warming by deposition is still active). Other conditions are the same as in the CNTL run. Like the NEVP experiment, the NSUB simulation restarts from the history file of the CNTL run saved at $t = 3$ h. The evolution of the NSUB storm is similar to the CNTL run. The NSUB storm propagates at a speed $1-1.5$ m s^{-1} slower than the CNTL storm, and the speed difference is 1.4 m s^{-1} during the mature stage ($t = 10-11$ h). Figure 3.16 displays the one-hour-average storm structure in the mature stage. Similar to the NMLT run, the simulation result of NSUB (where sublimational cooling is turned off everywhere) is almost the same as the result where sublimational cooling is turned off only in the stratiform region (not shown), since the dominant sublimational cooling process occurs in the stratiform region (Fig. 3.8d).

Without the latent cooling by sublimation, the ascending FTR flow (Fig. 3.16a) is much weaker (-24 m s^{-1} vs. -30 m s^{-1}) but the maximum of descending RTF flow at the rear of the storm is only slightly weaker. Since sublimational cooling only slightly affects the strength of the enhanced rear inflow at the back edge of the system (7 m s^{-1} in Fig. 3.16a vs. 8 m s^{-1} in Fig. 3.11a), we conclude that *the latent cooling by evaporation and melting are the most important microphysical processes determining the structure and strength of rear inflow in the cloud-model simulations.*

However, the observed rear inflow (Fig. 2.7b) has stronger magnitude (~ 15 m s^{-1}) and is located ~ 1 km above the melting level ($z = 4$ km). It is associated with ambient RTF flow induced by a short-wave trough in the upper troposphere (Zhang and Gao 1989; Braun 1995). This ambient RTF flow is not included in the cloud model. When large-scale baroclinic processes are included (for example, in a mesoscale model), the large-scale contribution to rear inflow can develop and occurs above the melting level; under these circumstances, the structure and strength of the rear inflow above the $0°$ C level is found to be more sensitive to latent cooling by sublimation (Braun 1995). The condensational heating within the ascending FTR flow and sublimational cooling at the back edge of the storm contribute to a strengthening of the large-scale trough and hence to the upper portion of the rear inflow.

The vertical velocity field of the NSUB storm (Fig. 3.16b) shows that the mesoscale updrafts/downdrafts in the stratiform region are much narrower (area of updraft/downdraft with magnitude greater than 0.5 m s^{-1} is 50 km wide vs. 80 km wide). In particular, without the diabatic cooling by sublimation, the mesoscale downdraft (the broad downdraft less than –0.5 m s^{-1}) is initiated below the 0°C level ($z = 4$ km), instead of above the 0°C level as in the CNTL run (Fig. 3.11b) and in the observations (Fig. 2.8b). The comparison of model runs NSUB and CNTL thus strongly supports the speculation of Rutledge et al. (1988) that *sublimational cooling at the base of the trailing anvil cloud is key to the initiation of downward air motion above the 0°C level ($z = 4$ km) at the rear of the storm.* Adiabatic warming associated with the mesoscale downdraft (Fig. 3.16c) at the rear edge of the NSUB storm is stronger (maximum θ' anomaly is 5 K vs. 4 K) and occurs at a higher altitude (5 km vs. 4 km), inducing a stronger mesolow at the back of the stratiform region (–3.3 mb vs. –3.0 mb; not shown).

3.3.6 Drier midlevel environment (DRYM)

The experiment DRYM is the same as the CNTL run except that the initial environmental moisture at midlevels ($z = 2.5$–6 km or $p = 800$–450 mb) is reduced by approximately half (see Fig. 3.1a). The DRYM storm generally evolves in the same way as the CNTL storm; it initially propagates slightly faster than the CNTL storm; after $t = 5$ h, it propagates slightly slower. Averaged over the total integration time (12 h), the difference of the propagation speeds between the two storms is less than 1 m s^{-1}. Figure 3.17 shows the DRYM storm structure during the mature stage.

The DRYM storm moves at approximately the same speed as the CNTL storm during the mature stage (12.2 m s^{-1}), as a result of similar strength and depth of the cold pool (Fig. 3.17c). The DRYM storm is more upright and has a slightly weaker ascending FTR flow (–27 m s^{-1} in Fig. 3.17a vs. –30 m s^{-1} in Fig. 3.11a). The descending RTF flow is much weaker with some FTR flow in between the two maxima of RTF flow (in the region $x = -100$ to –80 km). In particular, the maximum of RTF flow at the back edge of the storm has only 38% of the strength in the CNTL storm (3 m s^{-1} vs. 8 m s^{-1}). This result is counter-intuitive; we expected the reduced midlevel environmental moisture to enhance the sublimational and evaporative cooling at the back edge of the system and thus to increase the local buoyancy gradients and the rear-inflow strength. However, the

horizontal buoyancy gradients of the DRYM storm in the stratiform region (Fig. 3.17c) are weaker than those of the CNTL storm (Fig. 3.11c).

This counter-intuitive behavior is related to the more upright system orientation in DRYM compared to CNTL. The drier environmental air entrained into the leading convective region enhances evaporative cooling at midlevels (see the $\theta' < -2$ K packet at $z = 4$ to 6 km, $x = 0$ km in Fig. 3.17c), which counteracts the vorticity tendency produced by the cold pool (Rotunno et al. 1988; Weisman 1992) and tilts the convection into a more upright orientation. The FTR flow is reduced, and the stratiform region is narrower and weaker in most respects. With less sublimation, melting, and evaporation in the trailing portion of the stratiform region, the horizontal buoyancy gradients in the stratiform region are weaker, and the RTF flow of the DRYM storm is much weaker than that of the CNTL storm.

The vertical velocity field of the DRYM storm (Fig. 3.17b) shows that in the convective region, the low-level updrafts near the gust front are weaker but midlevel ones are stronger. In the stratiform region, the mesoscale downdrafts are 22% stronger (-1.1 m s^{-1} vs. -0.9 m s^{-1}), as a result of an enhanced evaporative cooling associated with lower midlevel environmental humidity. In contrast, the mesoscale updrafts are weaker (0.8 m s^{-1} vs. 1.1 m s^{-1}) and narrower (area enclosed by the 0.5 m s^{-1} contour is 45 km wide vs. 80 km wide).

3.4 Role of mesolows in the formation of the descending rear-to-front flow

Smull and Houze (1987b) suggested that the midlevel mesolow in the stratiform region might act in conjunction with the mesolow in the convective region to establish a broad RTF current across the storm. They further suggested that the RTF flow in some cases could be generated by "the physical processes internal to the mesoscale convective system" without the aid of ambient flow entering the system.

Zhang and Gao (1989) performed mesoscale model (MM4) simulations of the 10-11 June storm and examined the mesolow mechanism proposed by Smull and Houze (1987b). In their experiment NEV[2], which had no resolvable-scale ($\Delta x = 25$ km in their fine mesh) evaporation and sublimation, they found that the RTF flow was weak and did

---

[2]it stands for "No EVaporation"

not extend down to the surface, despite the occurrence of a strong midlevel mesolow (see their Fig. 13). The strong midlevel mesolow was produced by the Fritsch–Chappell (1980) convective parameterization scheme and was located in the leading convective region. This result seemed to suggest that, "the midlevel mesolow mechanism proposed by Smull and Houze (1987b) cannot be used alone to explain the generation of the descending rear inflow."

We investigate this question further. The Klemp-Wilhelmson cloud model used in this study constitutes a more explicit physical framework to investigate "the physical processes internal to the mesoscale convective system" referred to by Smull and Houze (1987b). The model is nonhydrostatic, the convection is explicitly resolved ($\Delta x = 1$ km in our fine mesh), and the environment is horizontally uniform, so that there are no large-scale baroclinic processes active in the simulation.

The two midlevel mesolows in a squall line with a trailing-stratiform precipitation region and the physical processes producing them are the phenomena that are key to understanding the ability of a mesoscale convective system to develop its own rear inflow. To investigate the role of mesolows in the formation of the descending rear inflow, we present Figs. 3.18 and 3.19, which show the storm-induced pressure perturbations with shaded RTF flow ($u-c > 5$ m s^{-1}) for three experimental simulations during the mature ($t = 10$–11 h; Fig. 3.18) and late stage ($t = 12.5$–13.5 h; Fig. 3.19). The detailed horizontal wind structures of these simulations are shown in Figs. 3.4b, 3.4c, 3.13a, and 3.14a.

In the no-evaporative-cooling run (NEVP; Fig. 3.18a), where the mesolows in both the convective and trailing stratiform regions are absent, there is *no* descending rear inflow; the rear inflow remains elevated. The rear inflow results from environmental winds entering and overtaking the storm. When the stratiform region is narrow and weak, as in the no-ice run (NICE; Fig. 3.18b), there is only one mesolow which is due to the slope of the convective cells in the leading line (LeMone 1983). In this case, there is only *one* RTF wind maximum. In the full-physics control run (CNTL; Fig. 3.18c), the low at the back of the convective cells is broader, and a second mesolow is at the back edge of the stratiform region. The mesolow in the stratiform region is *collocated* with the RTF wind maximum at the back edge of the stratiform precipitation ($x = -160$ to -130 km). This structure is consistent with Smull and Houze's suggestion that the resulting horizontal pressure-

gradient force associated with the stratiform-region mesolow draws midlevel air into the storm from the rear to induce the rear inflow.

The RTF flow during the late stage of the NICE storm (Fig. 3.19a) has the same width, intensity, and slope as in the mature stage (Fig. 3.18b). However, in the late stage of the full-physics CNTL run (Fig. 3.19b), the mesolow in the convective region is broader and stronger, and the two RTF maxima are more distinct and more widely separated from each other than in the mature stage (Fig. 3.18c). With ice-phase microphysics included, the RTF flow (Fig. 3.19b) descends and spreads along the surface well behind the leading edge of the storm. The enhanced RTF flow at the back edge of the storm ($x = -200$ km) is located farther rearward in the late stage, consistent with radar observations (see Figs. 5–7 of Rutledge et al. 1988).

Since large-scale baroclinic processes are inoperative and the descending rear inflow in this model is caused entirely by the storm-induced circulation, this study confirms the conclusion of Smull and Houze (1987b) and Lafore and Moncrieff (1989) that the rear inflow can be generated by physical processes internal to the MCS. The good correspondence of the midlevel mesolow in the convective/stratiform region to the maximum RTF flow at the rear of the convective/stratiform region (in the CNTL run) further supports Smull and Houze's argument that two separate midlevel mesolows are involved in the development of the RTF flow and that the two mesolows may act constructively to establish a continuous RTF flow channel across the storm.

3.5 Summary

Two-dimensional simulations of the 10-11 June 1985 squall line in PRE-STORM with the Klemp-Wilhelmson cloud model reproduce a storm structure that agrees with the detailed observations obtained in this case. Despite two-dimensional geometry and neglect of Coriolis force, large-scale motion, radiation, and surface drag, the microphysical, kinematic, thermal, and pressure structures are well simulated.

The ascending FTR flow transports hydrometeors across the system from the leading-edge convective line to the trailing-stratiform region. The FTR flow becomes stronger and more horizontally tilted with time. The descending RTF flow enters the storm from the rear and penetrates into the convective region at low levels. As the system matures and expands, the RTF flow develops a double-maximum structure. A maximum

of RTF flow located at the back edge of the stratiform precipitation consists of midlevel environmental air from the rear of the storm.

The mesoscale updraft and downdraft become organized once the system is well developed, and they reach their maximum strength during the mature stage. Air-parcel trajectory analysis indicates that most of the air within mesoscale updrafts originally comes from the high-θ_e boundary layer ahead of the system. About half of the air within mesoscale downdraft is from the leading-edge convective region, and the other half is from the poststorm midlevel low-θ_e layers. Precipitation particles falling into the transition zone are from the low levels of the convective region, and those falling into the stratiform region are from the mid- to upper-levels of the convective region, consistent with the results of Biggerstaff and Houze (1993) and Braun and Houze (1994a).

Most of the latent heating in the cloudy region is produced by condensational warming of cloud water, and most of the latent cooling in the subcloud region is produced by evaporative cooling of rainwater. Depositional growth of ice particles in the stratiform cloud region adds additional latent heating and enhances the mesoscale updraft. The structure and strength of the rear inflow is found to be sensitive to precipitating hydrometeor types, ice-phase microphysics, and the latent cooling of evaporation, melting, and sublimation. A series of sensitivity tests isolates and quantifies the role of each of these microphysical processes in the generation and maintenance of the descending RTF flow. Table 3.2 summarizes the main results of each test.

In the HAIL test, hailstones are allowed to form throughout the mature and decaying stages. Hail particles fall out so quickly that the surface precipitation region is much narrower than in the control case (CNTL), in which there are no hailstones after the initial stage. The stratiform precipitation region is weak and narrow. The broad and uniform mesoscale updraft/downdraft does not occur. There is only one maximum of RTF flow within the storm; no second maximum occurs at the back edge, because the midlevel mesolow in the stratiform region is too weak. The realistic structure of the simulated descending rear inflow (at least for the 10-11 June 1985 squall line) thus appears to be sensitive to the hydrometeor types, which affect the kinematic structure of the storm through their fallout pattern and the subsequent effects of diabatic processes on the thermal and pressure fields.

Stratiform precipitation and the enhanced RTF flow at the back edge of the storm in the no-ice run (NICE) are not as realistic as in the CNTL run. The lack of ice microphysics and realistic stratiform precipitation implies that none of the key cooling processes in the production of the rear inflow—sublimation, melting, and evaporation—can occur in the stratiform region. The NICE test thus shows that ice microphysics are crucial to the proper existence of the descending rear inflow and mesoscale updraft/downdraft.

In the test with evaporative cooling turned off (NEVP), the system is upright to downshear-tilted, with stratiform precipitation ahead of the convective region. There is no mesoscale ascent or descent. There is no mid-to-upper level FTR flow transporting hydrometeors rearward. The RTF flow is elevated, a consequence of strong midlevel winds in the environment overtaking and entering the storm. The NEVP test thus supports the argument of Smull and Houze (1987b) that the descending rear inflow and mesoscale downdraft develop in response to the dynamical and microphysical feedbacks (in particular, the evaporative cooling) of the storm.

The no-melting-cooling (NMLT) storm is more upright compared to the CNTL case. The double maximum structure of the RTF flow is well preserved, indicating that the cooling by melting is not the cause of rear inflow. However, this experiment shows that the latent cooling by melting accounts for at least 25% of the intensity of the peak RTF flow at the back edge of the storm during the mature stage, confirming the impact of melting cooling on the stratiform-region RTF flow suggested by Smull and Houze (1987b) and Rutledge et al. (1988). The mesoscale ascent of the NMLT storm is somewhat stronger, and the mesoscale descent is 22% weaker and 33% narrower. Therefore, cooling by melting does not initiate the mesoscale downdraft (as suggested by Leary and Houze 1979), but does strongly enhance the mesoscale downdraft.

The test NSUB (latent cooling by sublimation turned off) shows that sublimational cooling only slightly affects the strength of the rear inflow in the cloud model simulation. However, sublimation at the base of the anvil cloud at the rear of the trailing-stratiform region is key to the initiation of downward air motion above the 0°C level ($z = 4$ km) at the rear of the storm, as suggested by Rutledge et al. (1988). A mesoscale model simulation of the same storm (Braun 1995) shows that, when the large-scale horizontal and temporal variations of the environment are taken into account in the development of the squall-line system, the sublimation also increases the RTF flow intensity at the back edge of the storm.

The test DRYM shows that with only half of the initial midlevel moisture, the mesoscale downdraft is 22% stronger, but the maximum of RTF flow at the rear of the system is 62% weaker. The weaker stratiform-region RTF flow is due to the weaker horizontal buoyancy gradients at the back edge of the storm, which result from a more upright system orientation. When drier environmental air is entrained into the storm, it enhances the evaporative cooling at midlevels at the leading edge and counteracts the upshear tilt induced by the cold-pool circulation.

In summary, the descending rear inflow is partly a dynamical response to the latent cooling processes in the squall-line's trailing-stratiform precipitation region. The role of mesolows in the formation of the descending RTF flow is discussed, and the numerical experiments confirm Smull and Houze's (1987b) argument that the stratiform-region mesolow acts constructively with the convective-region mesolow to establish a continuous RTF flow across the system. The simulated RTF flow is more sensitive to evaporative cooling than to other latent cooling processes. The descent of the rear inflow and the mesoscale downdraft are initiated above the 0°C level by sublimation at the base of the trailing cloud anvil. The role of sublimation is better seen in the mesoscale model experiments of Braun (1995). Melting does not initiate the mesoscale downdraft but strongly enhances both the mesoscale downdraft and the RTF flow in the stratiform region. Evaporation accounts for most of the structure and strength of the descending RTF flow, but without ice-phase microphysics, neither the realistic stratiform precipitation nor the enhanced RTF flow at the back edge of the storm can occur. Finally, correct types of ice particles must be included in the model in order to have a proper structure of the descending RTF flow, at least for the 10-11 June 1985 squall line.

An important implication of the results in Chapter 3 is that parameterization of MCSs in a large-scale general circulation model (GCM) is not simple. A slight change of hydrometeor types, ice microphysics, and environmental humidity can significantly affect the storm structure, and hence momentum and moisture transports, radiation budget, and the interaction with the surrounding large-scale environment. Therefore, the proper handling of microphysical processes is necessary in order to have a reasonable representation of the effects of MCSs in a GCM or a numerical weather prediction model.

Table 3.1 Design of experimental simulations.

Run	Run time	Restart time	Comments
CNTL	15 h		full physics; turn off hail generation processes after 6 h
HAIL	13 h		full physics; leave hail generation processes on after 6 h
NICE	14 h		no ice-phase microphysics
NEVP	12 h	CNTL at 3 h	no evaporative cooling
NMLT	12 h	CNTL at 3 h	no melting cooling
NSUB	12 h	CNTL at 3 h	no sublimational cooling
DRYM	12 h		drier midlevel environment; see Fig. 1.1a

Table 3.2 Summary of mature-stage RTF flow structure of experimental simulations.

Run	Storm speed	Storm orientation	RTF flow structure
CNTL	12.2 m s^{-1}	upshear tilt	two maximum in the storm (8)*
HAIL	11 m s^{-1}	upshear tilt	one maximum in convective region
NICE	8 m s^{-1}	upshear tilt	one maximum in convective region
NEVP	5 m s^{-1}	upright to downshear-tilt	a highly elevated RTF flow
NMLT	12 m s^{-1}	less upshear tilt	two maximum in the storm (6)
NSUB	10.8 m s^{-1}	less upshear tilt	two maximum in the storm (7)
DRYM	12.2 m s^{-1}	more upright	two maximum in the storm (3)

*Number in the parentheses is the maximum of RTF flow in m s^{-1} at the back edge of the stratiform precipitation during the mature stage ($t = 10–11$ h).
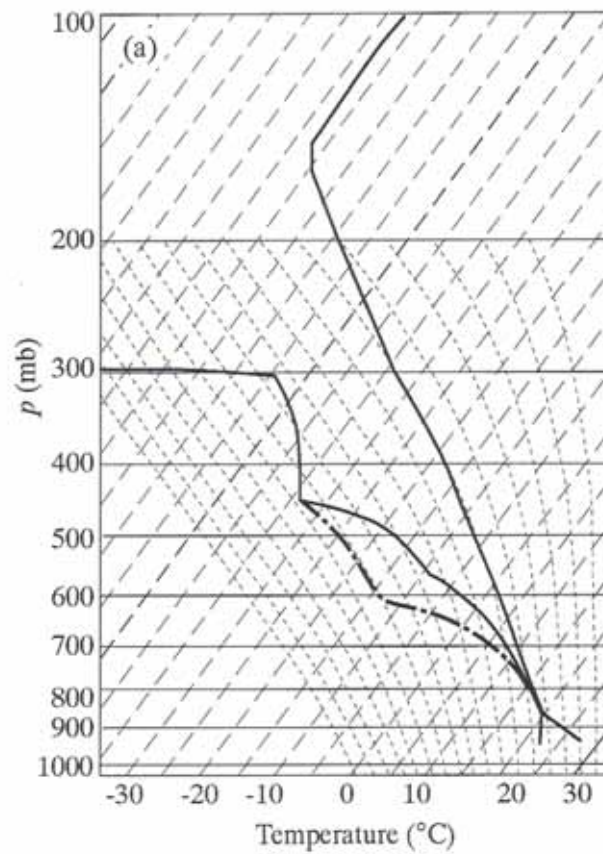
Fig. 3.1 (a) Temperature and dewpoint soundings of Enid, Oklahoma on 2331 UTC 10 June 1985. Dashed–dot line is the dew point profile for the DRYM run (see Section 3.3.6 for details).
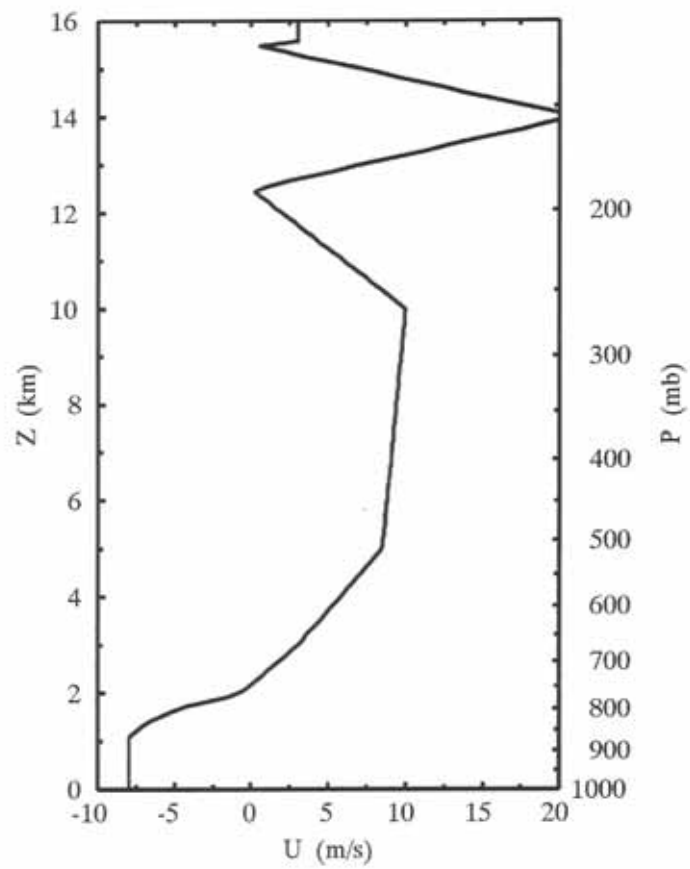
Fig. 3.1 (b) the cross–line wind component of Enid, Oklahoma on 2331 UTC 10 June 1985.

CV and SF precipitation
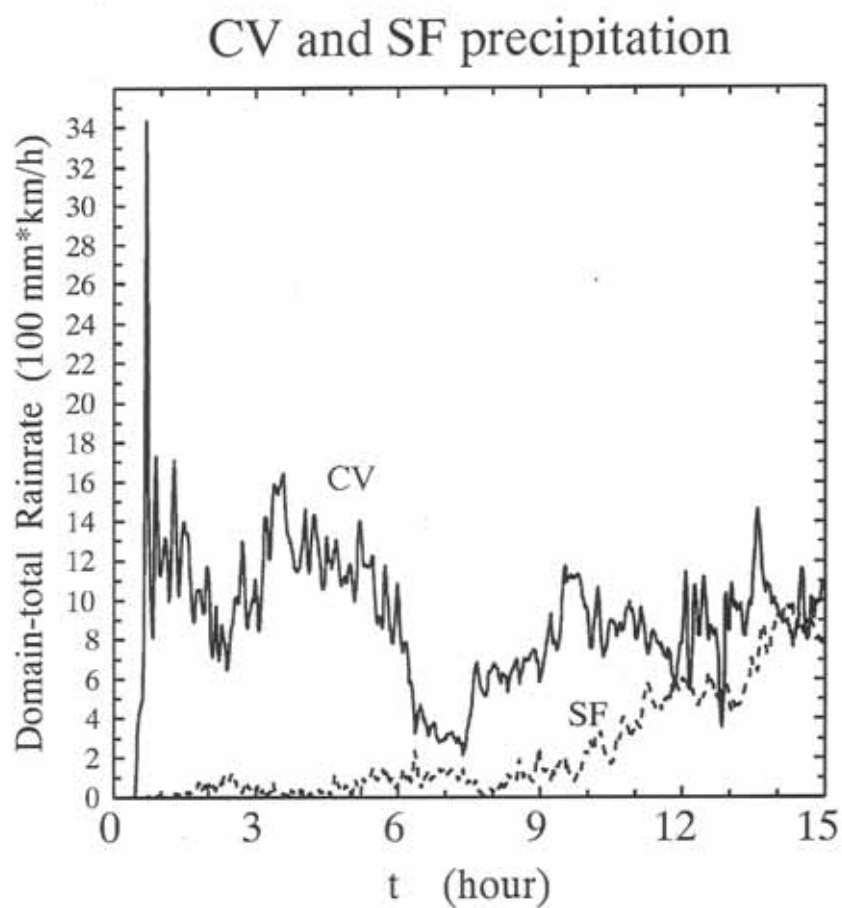
Fig. 3.2 Time evolution of domain total (in units of 100 mm h^{-1} km) surface convective (CV) and stratiform (SF) rainfall rates of the full–physics CNTL storm. See text for the criteria of convective and stratiform precipitation.
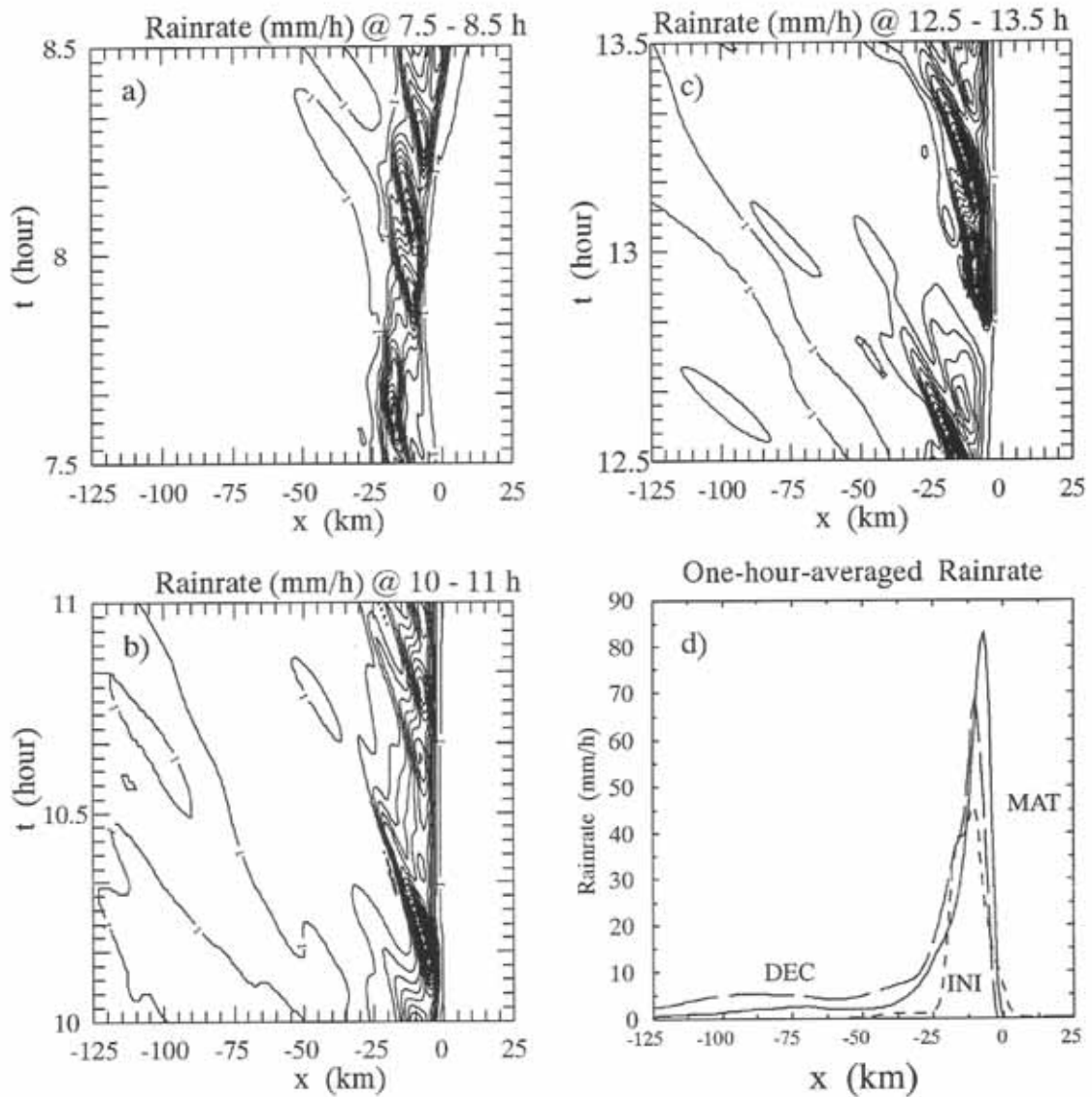
Fig. 3.3 Time history of surface rainfall rate during (a) the initial stage (INI; $t =$ 7.5–8.5 h), (b) mature stage (MAT; $t =$ 10–11 h), and (c) slowly decaying stage (DEC; $t =$ 12.5–13.5 h) of the CNTL storm. The three one–hour–averaged surface rainfall rates of the CNTL storm are in (d). Contour lines in (a)–(c) start from 1 mm h^{-1} with an interval of 10 mm h^{-1}. These surface rainfall rate fields are displayed in a storm–relative coordinate such that the gust front is fixed at $x =$ 0 km.
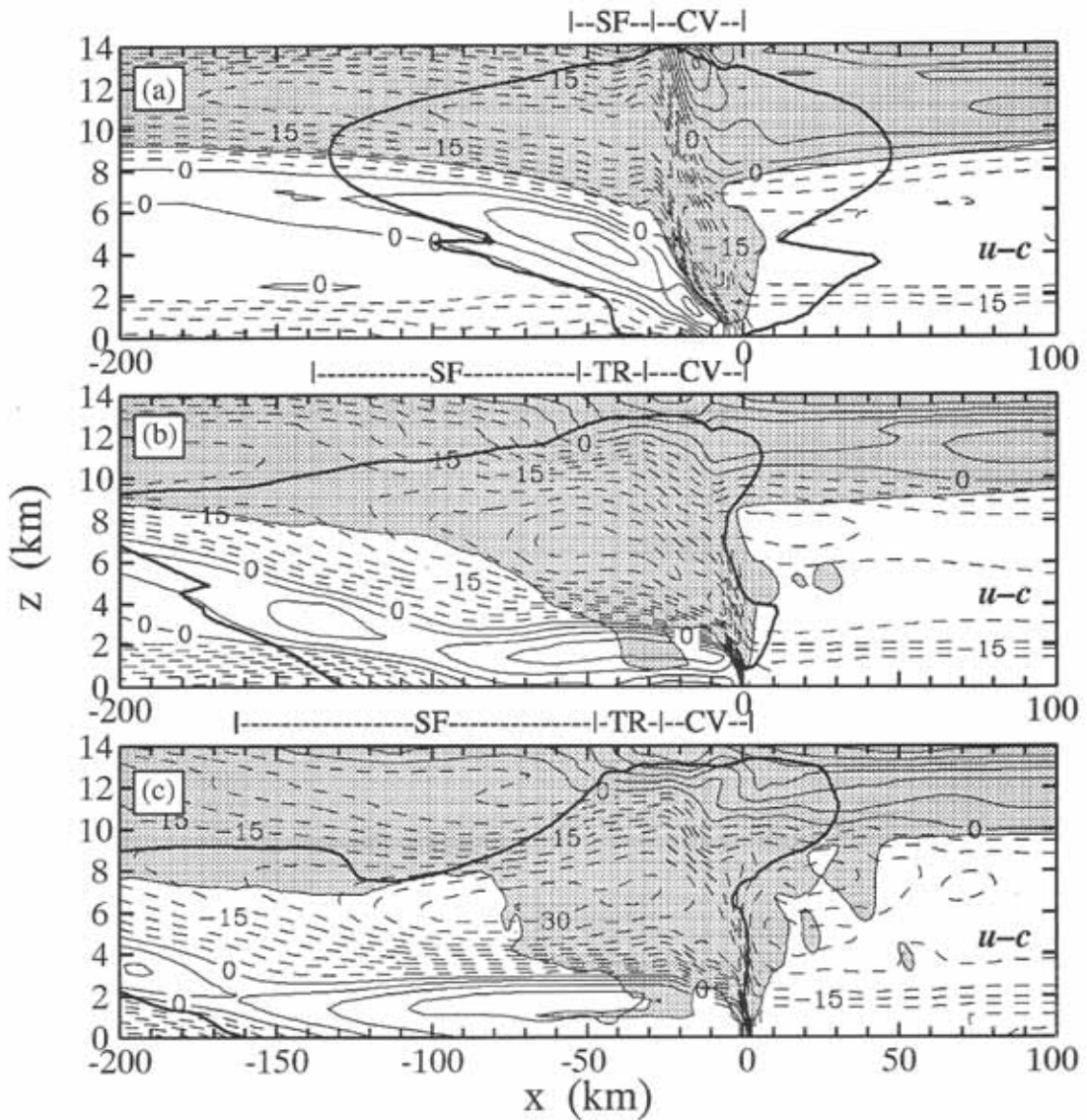
Fig. 3.4 Storm–relative horizontal wind field (u–c; contour interval is 3 m s^{-1}) averaged during (a) the initial stage ($t = 7.5$–8.5 h); (b) mature stage ($t = 10$–11 h), and (c) the slowly decaying stage ($t = 12.5$–13.5 h) of the CNTL storm. Rear-to–front flow is in solid lines, and front–to–rear flow is dashed. Region of time–averaged nonprecipitating hydrometeor (cloud water and cloud ice) mixing ratio greater than 0.1 g kg^{-1} is shaded. Heavy outline is the storm precipitation boundary determined by the time–averaged modeled radar reflectivity of 15 dBZ contour. Locations of convective region (CV), transition zone (TR), and stratiform region (SF) are shown in the bar above.
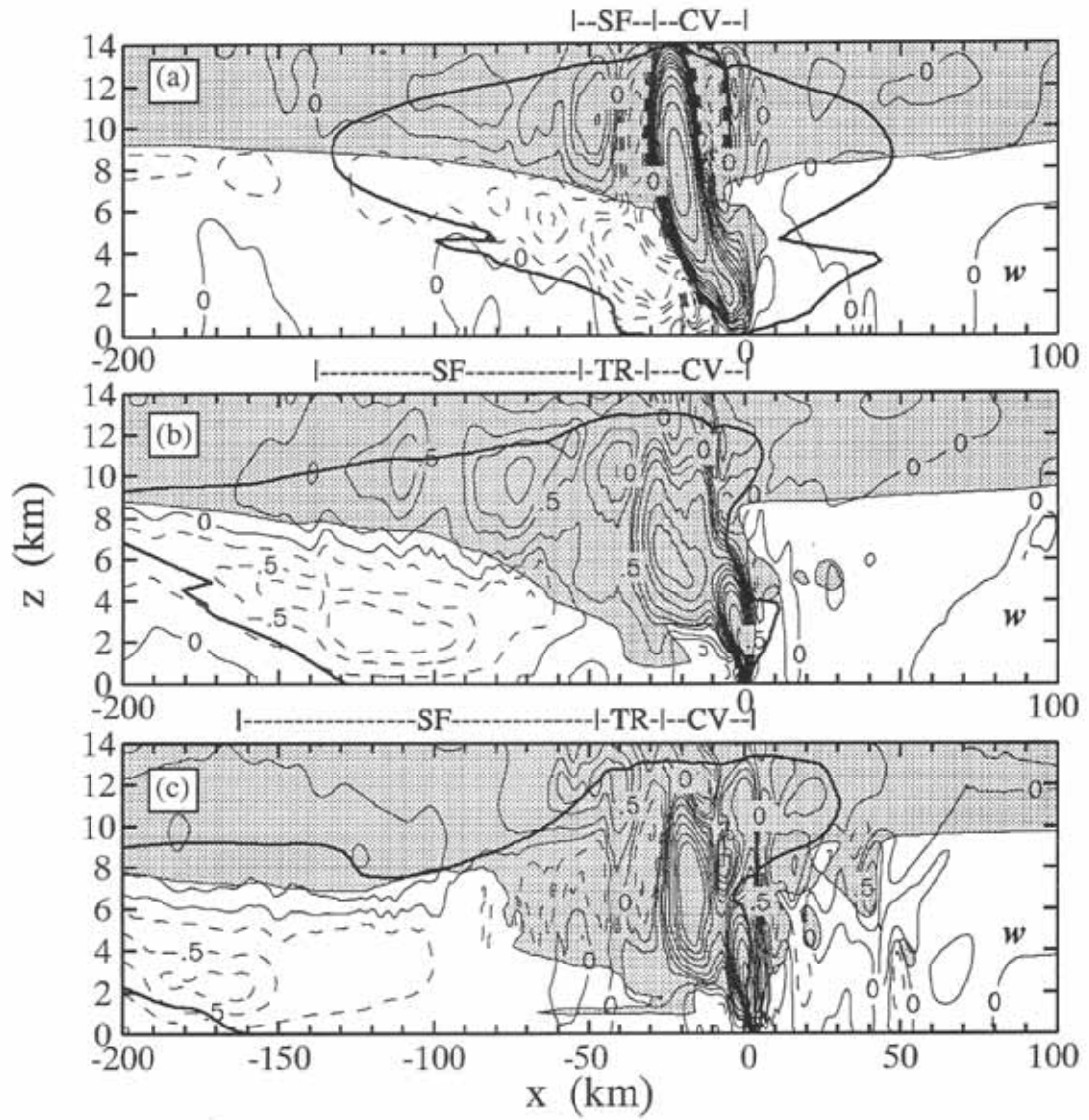
Fig. 3.5 Same as Fig. 3.4 except for vertical velocity field (w). Vertical velocity is contoured at −4, −2, −1.5, −1, −0.7, −0.5, −0.2, 0, 0.2, 0.5, 0.7, 1, 1.5, 2, 2.5, 3, 4, 5, 7, 10, and 13 m s^{-1}. Positive field is in solid lines; the negative field is dashed.
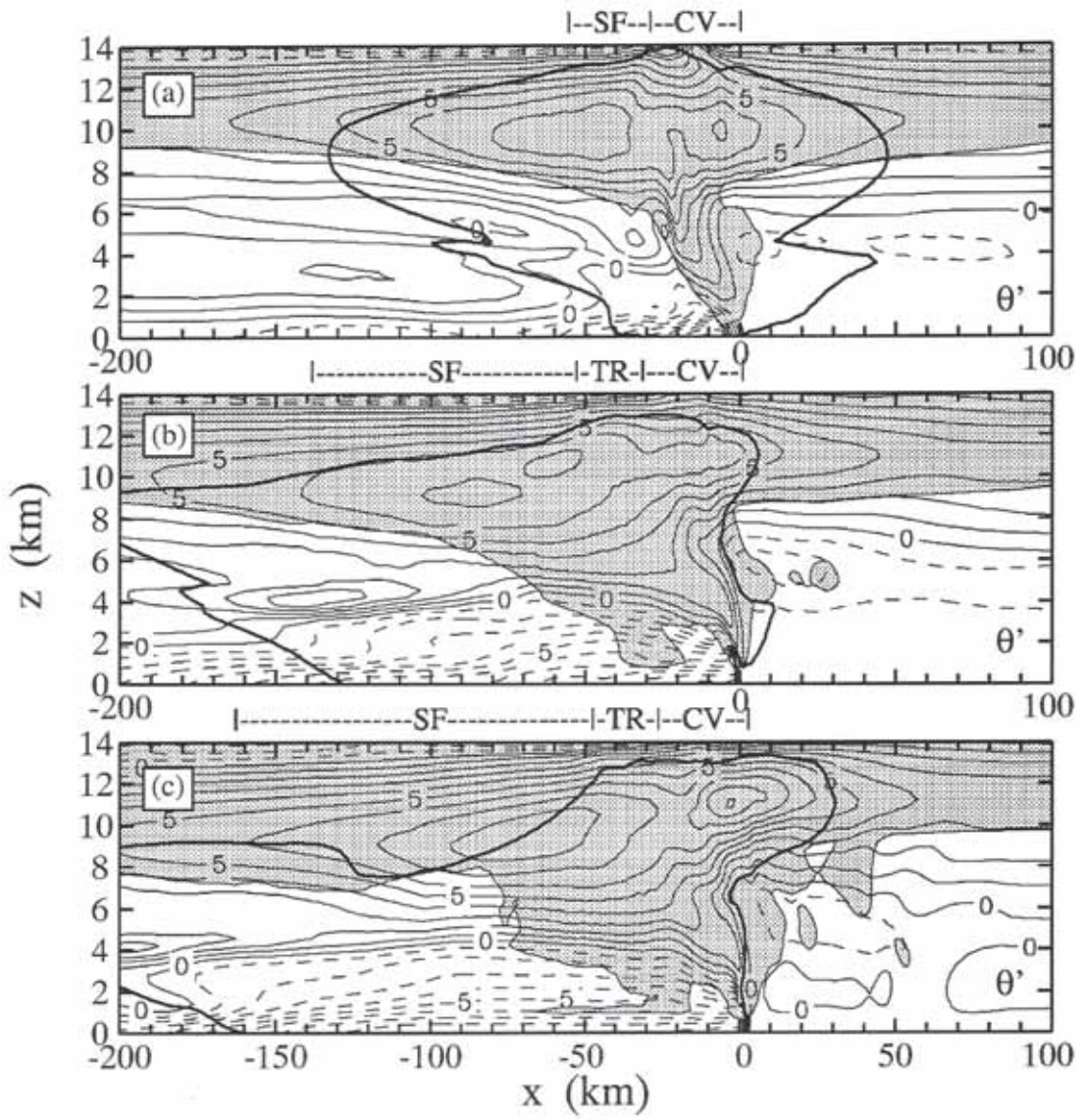
Fig. 3.6 Same as Fig. 3.4 except for potential temperature perturbation (θ'; contour interval is 1 K).
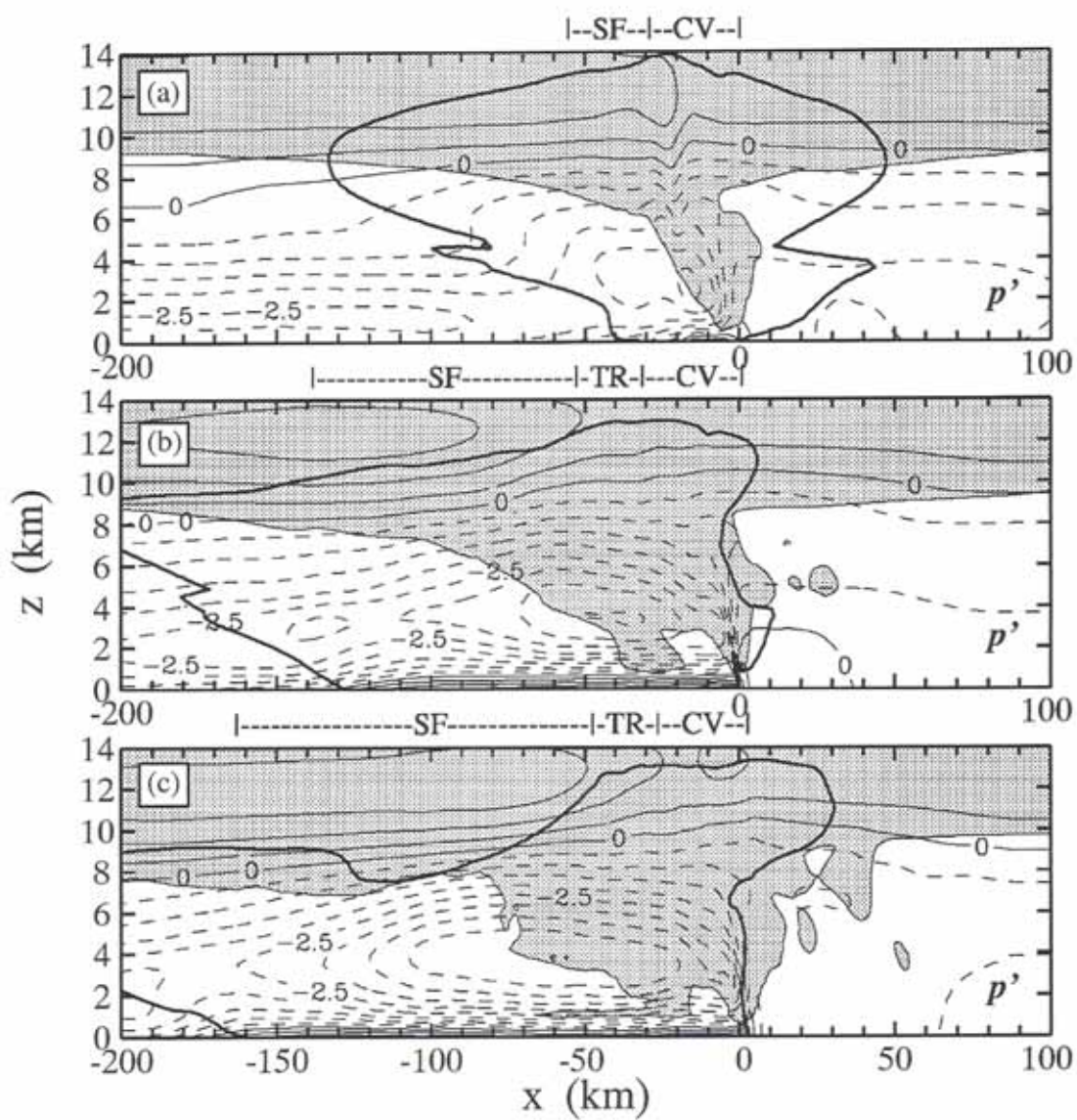
Fig. 3.7 Same as Fig. 3.4 except for pressure perturbation (p'; contour interval is 0.5 mb).
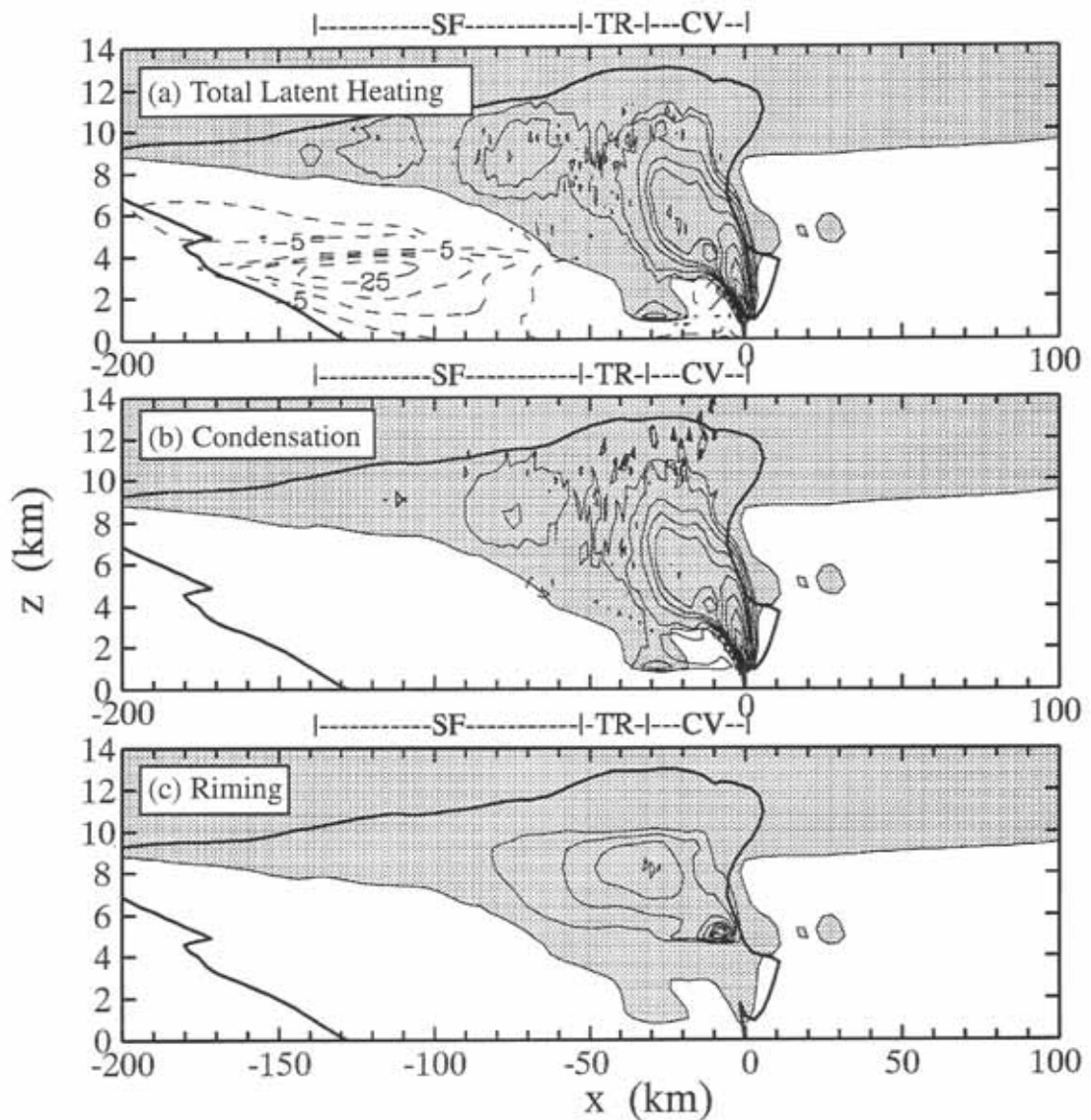
Fig. 3.8 One–hour–averaged (t = 10–11 h) fields of (a) total latent heating, (b) condensational warming, (c) riming warming (contour interval is 1 K h^{-1}), (d) depositional warming and sublimational cooling (contour interval is 1 K h^{-1}), (e) melting cooling (contour interval is 2 K h^{-1}), and (f) evaporative cooling (contour interval is 4 K h^{-1}) of the CNTL storm. Latent heating in (a) and (b) is contoured at –25, –15, –10, –5, 5, 10, 20, 30, 40, 60, 100, 140, 180, and 220 K h^{-1} .
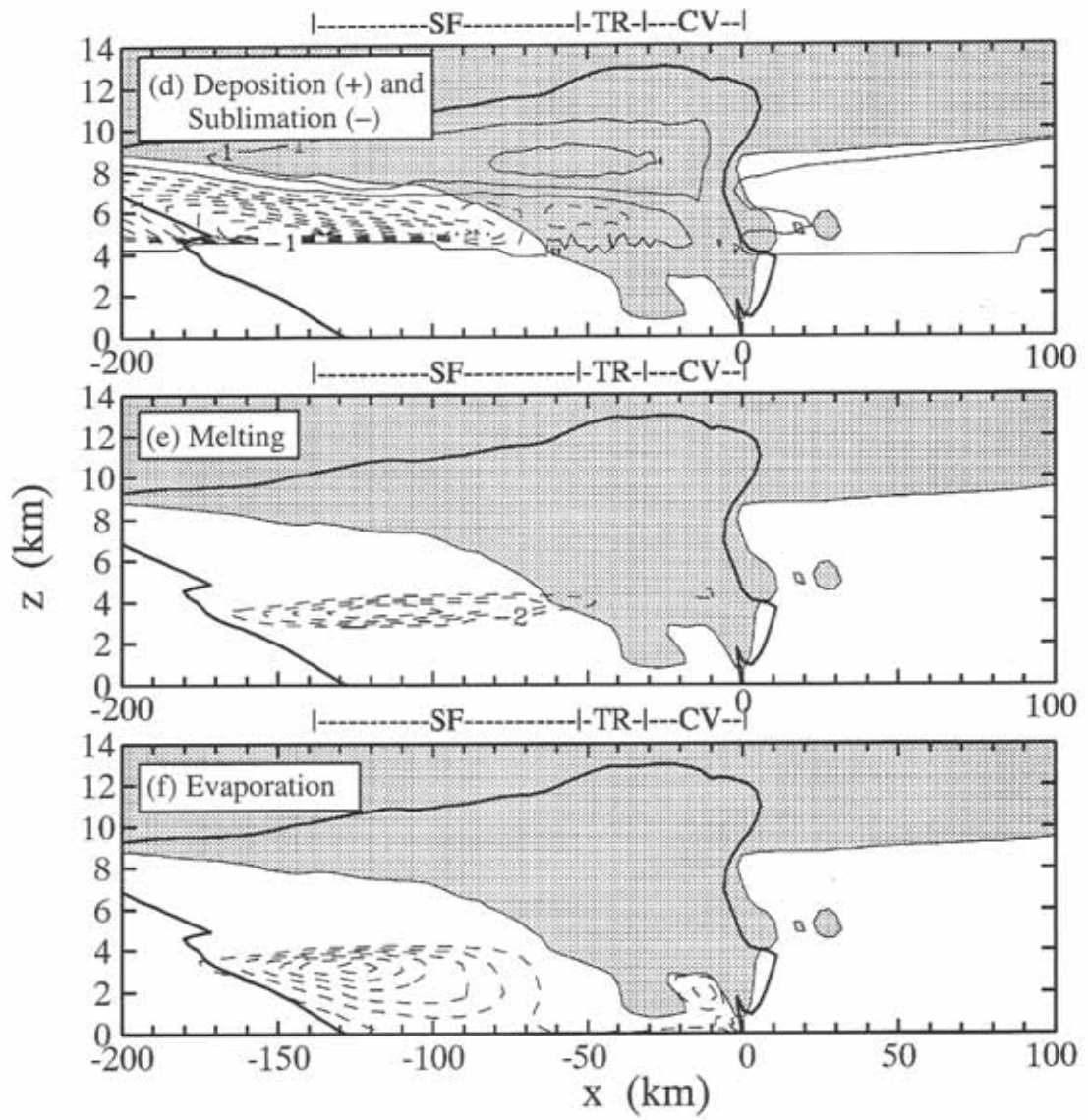
Fig. 3.8 (*contd.*) The heating field is in solid lines, and the cooling field is dashed. Shaded cloudy region and the storm precipitation boundary outline are the same as in Fig. 3.4.
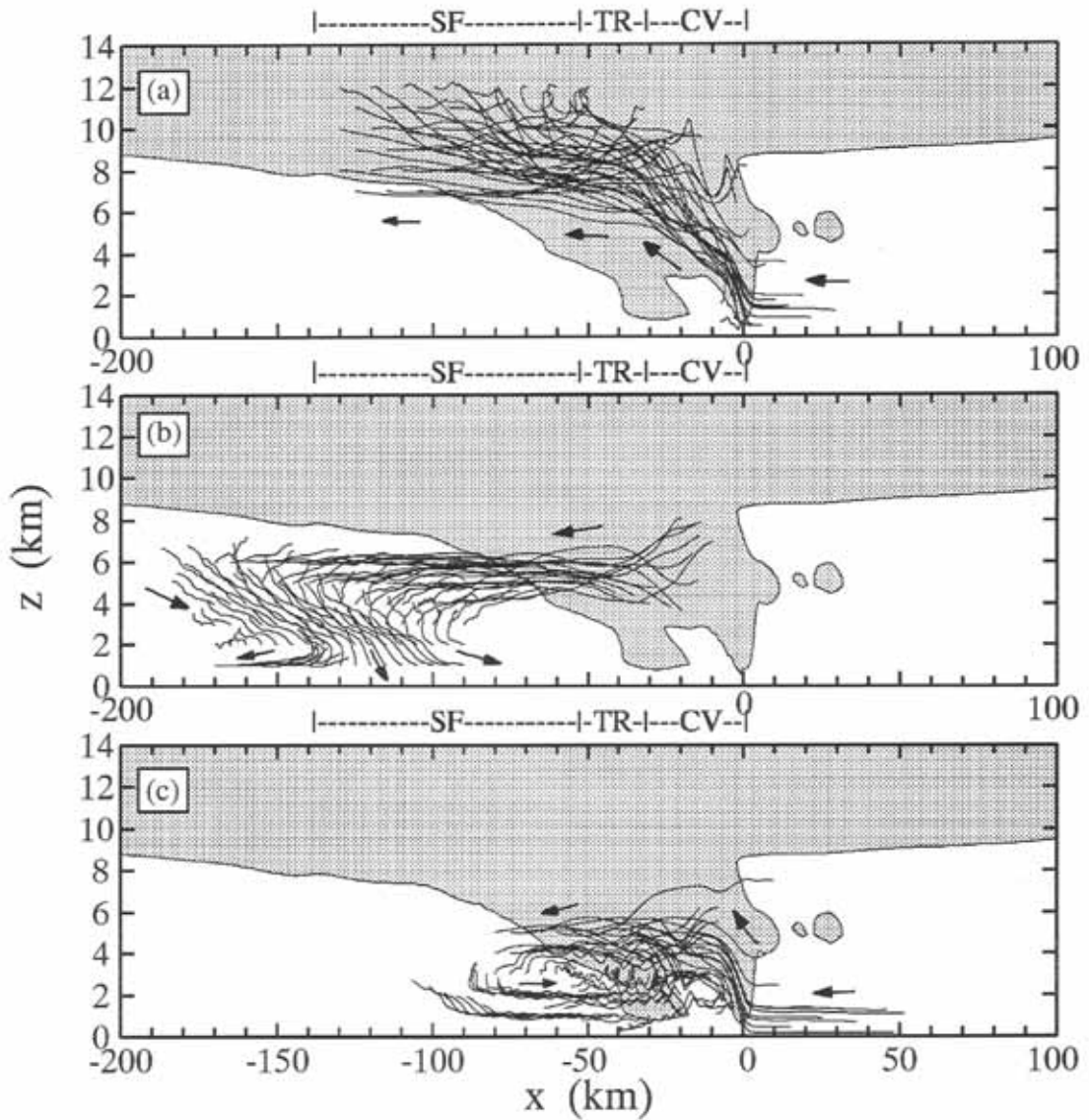
Fig. 3.9 One–hour (t = 10–11 h) air–parcel trajectories highlight (a) the origin of mesoscale ascent, (b) the origin of mesoscale descent, and (c) the rotor circulation within the cold pool of the CNTL storm. Air parcels move in the direction of arrows. Shaded cloudy region is the same as in Fig. 3.4.
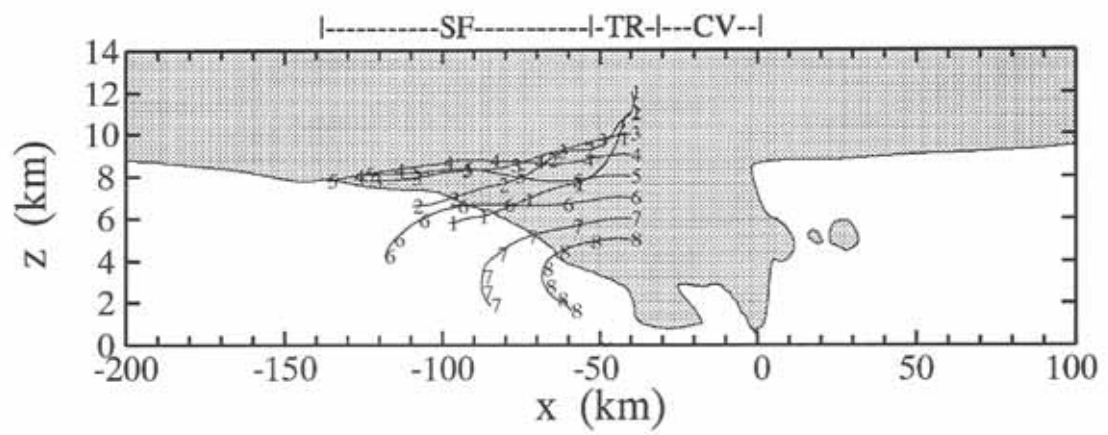
Fig. 3.10 One–hour ($t = 10$–11 h) trajectories of precipitating particles starting from different vertical levels in the transition zone for the CNTL run. Each number along the trajectories indicates the particle position every 10 min. Shaded cloudy region is the same as in Fig. 3.4.
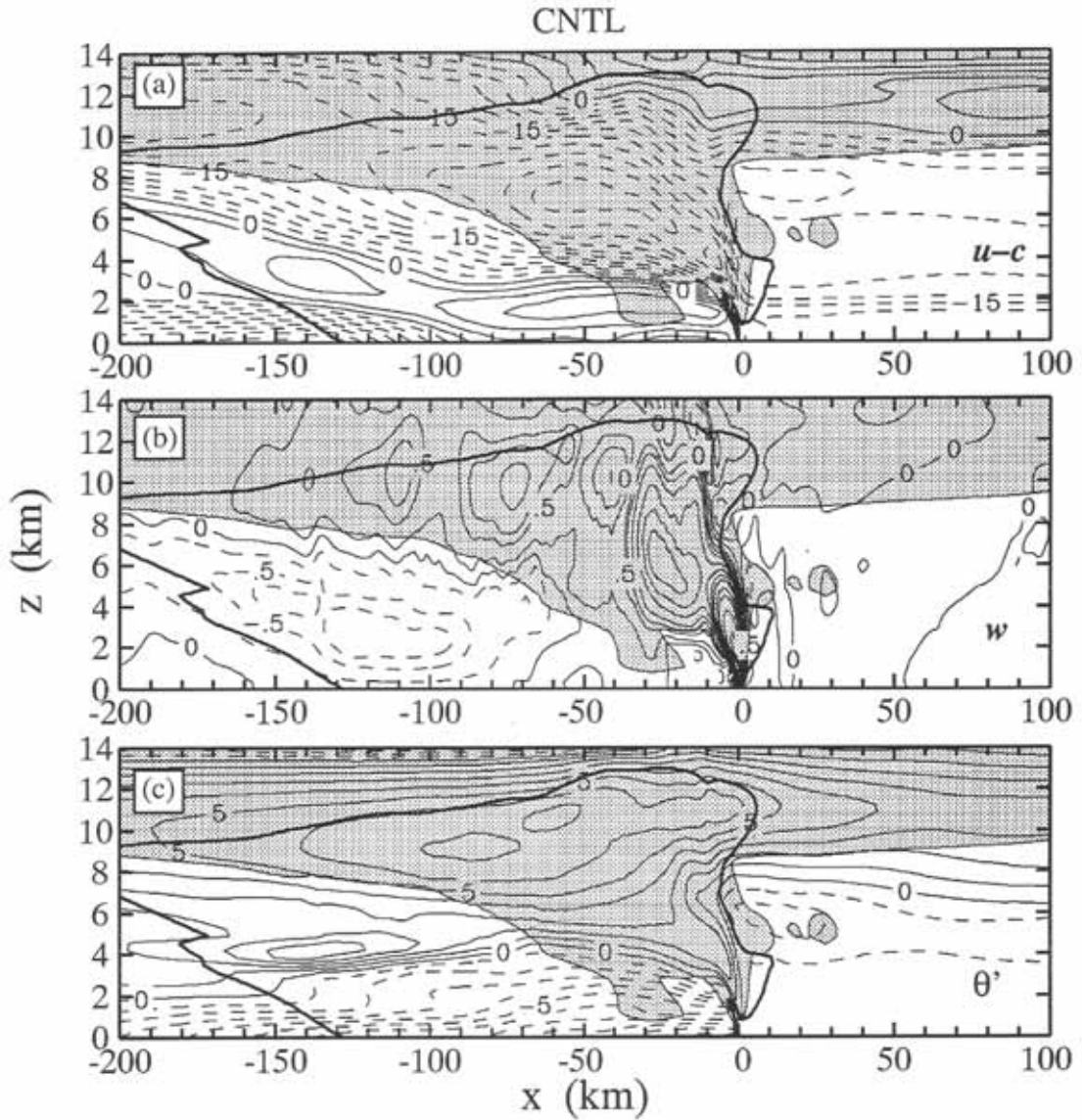
CNTL

Fig. 3.11 (a) One–hour–averaged (t = 10–11 h) storm–relative horizotal wind (u–c; contour interval is 3 m s^{-1}), (b) vertical velocity (w), and (c) potential temperature perturbation (θ'; contour interval is 1 K) of the CNTL storm. Vertical velocity in (b) is contoured at –4, –2, –1.5, –1, –0.7, –0.5, –0.2, 0, 0.2, 0.5, 0.7, 1, 1.5, 2, 2,.5, 3, 4, 5, 7, 10, and 13 m s^{-1}. Shaded cloudy region and the storm precipitation boundary outline are the same as in Fig. 3.4.
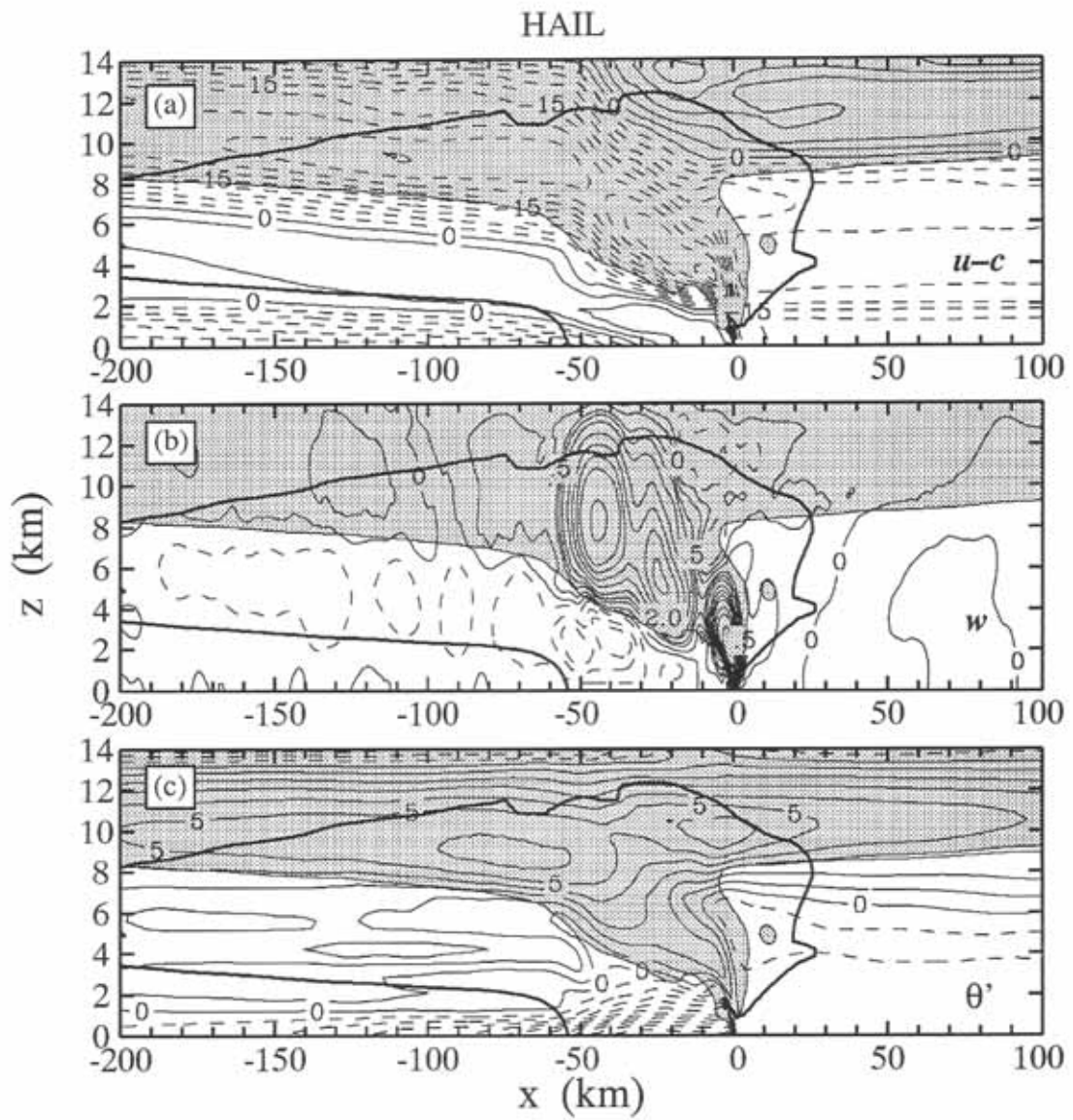
HAIL

Fig. 3.12 Same as Fig. 3.11 except for the HAIL storm.
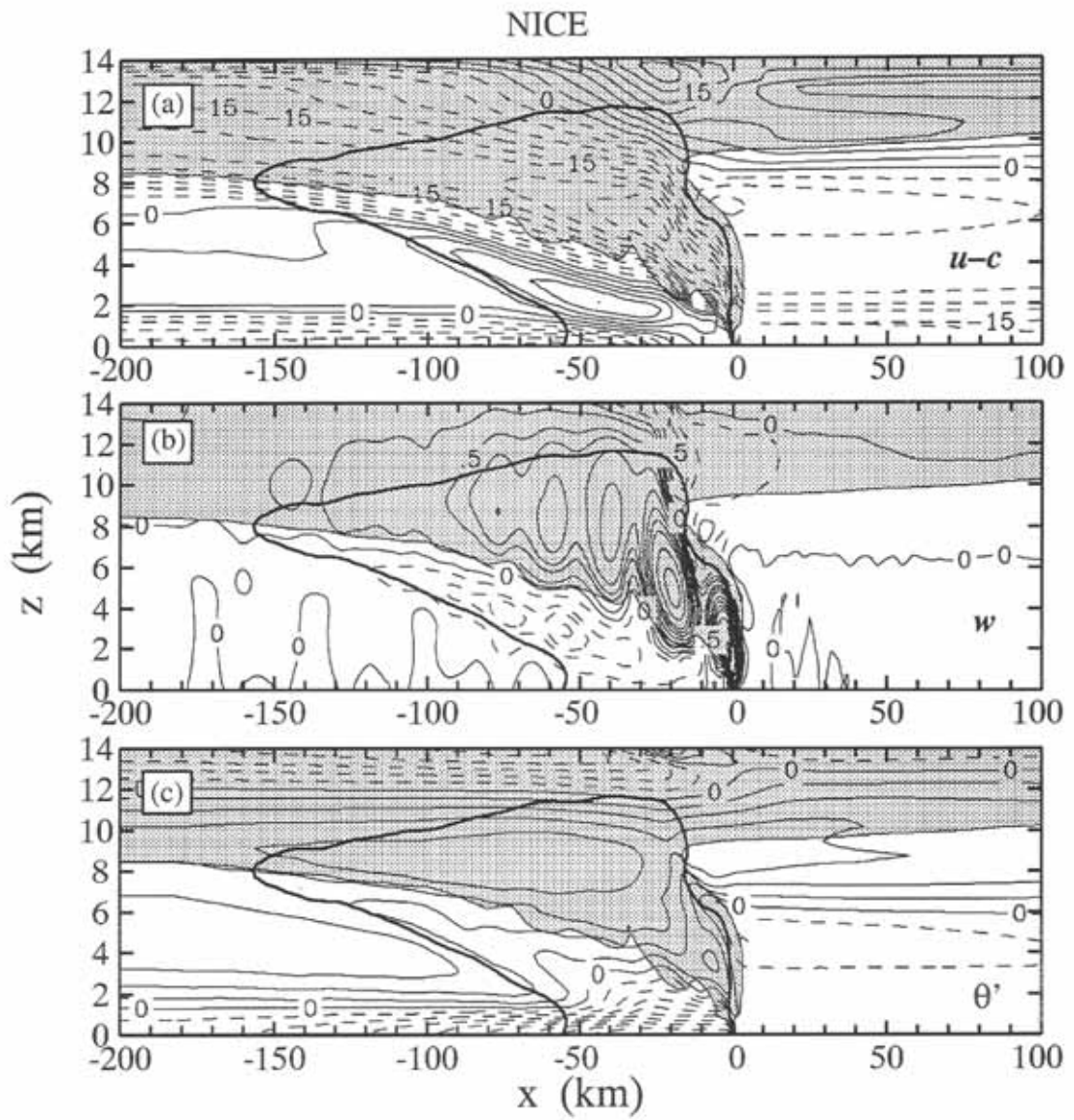
NICE

Fig. 3.13 Same as Fig. 3.11 except for the NICE run.
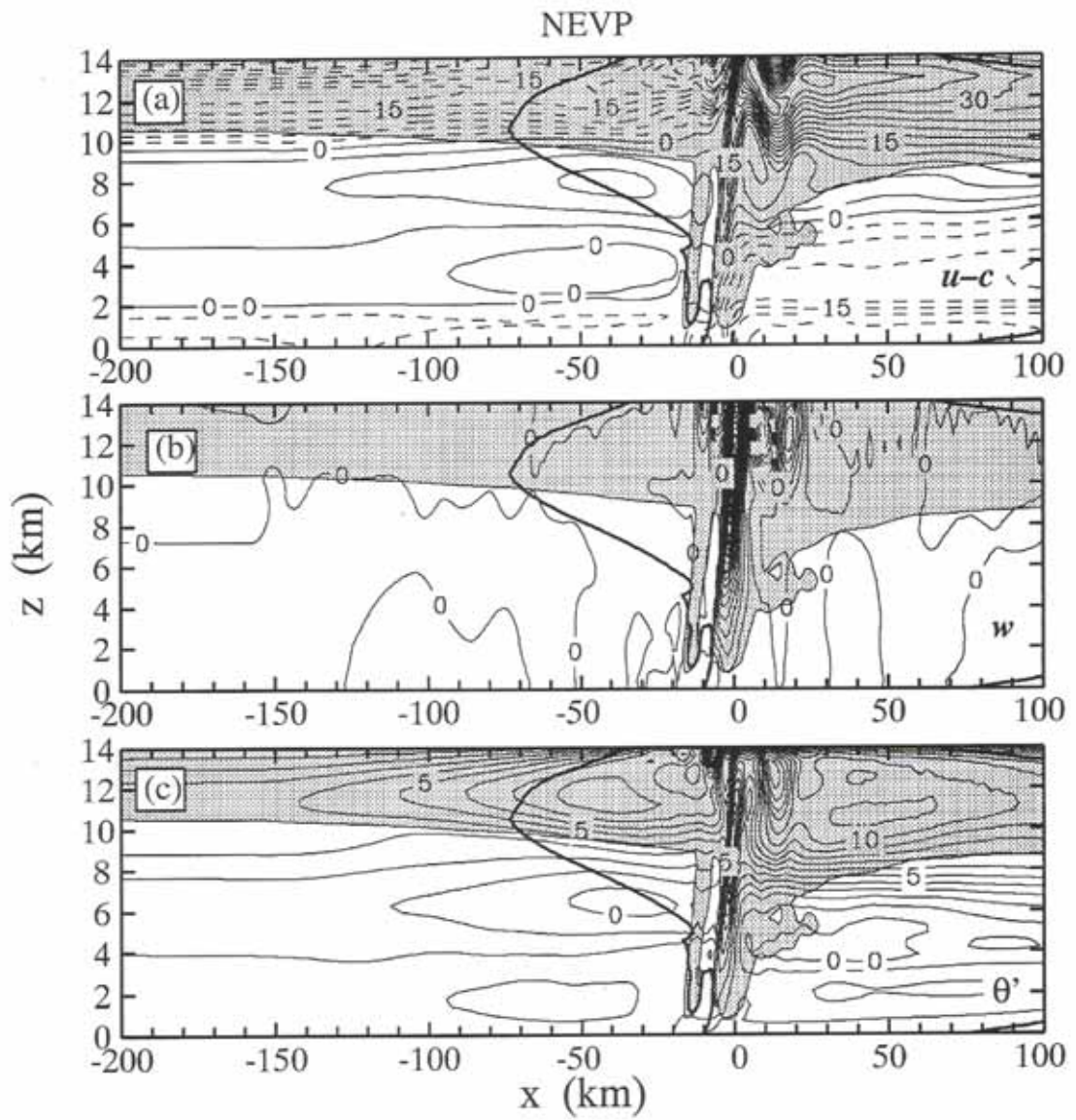
Fig. 3.14 Same as Fig. 3.11 except for the NEVP run. Vertical velocity in (b) is contoured every 2 m s⁻¹.
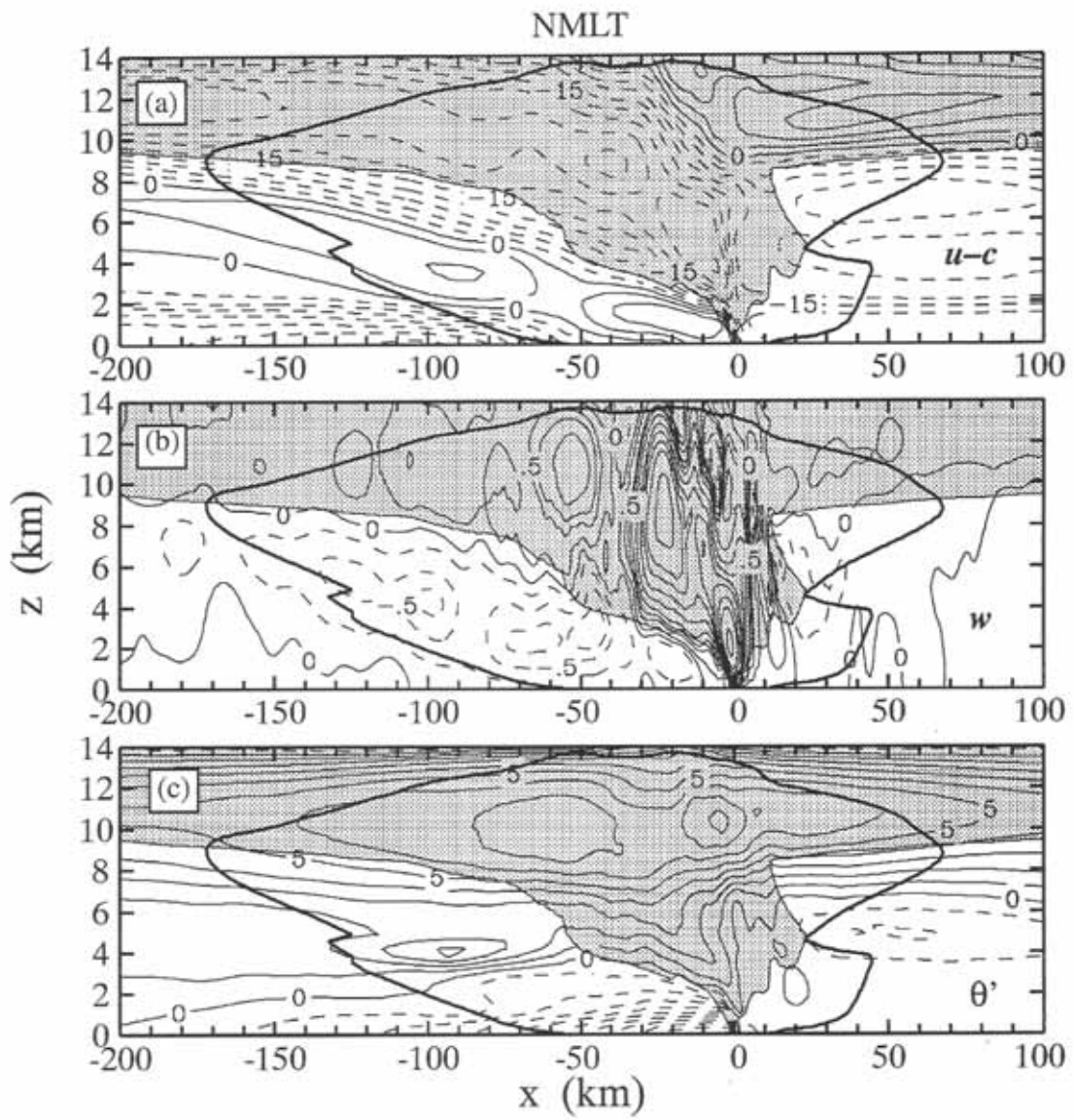
Fig. 3.15 Same as Fig. 3.11 except for the NMLT storm.
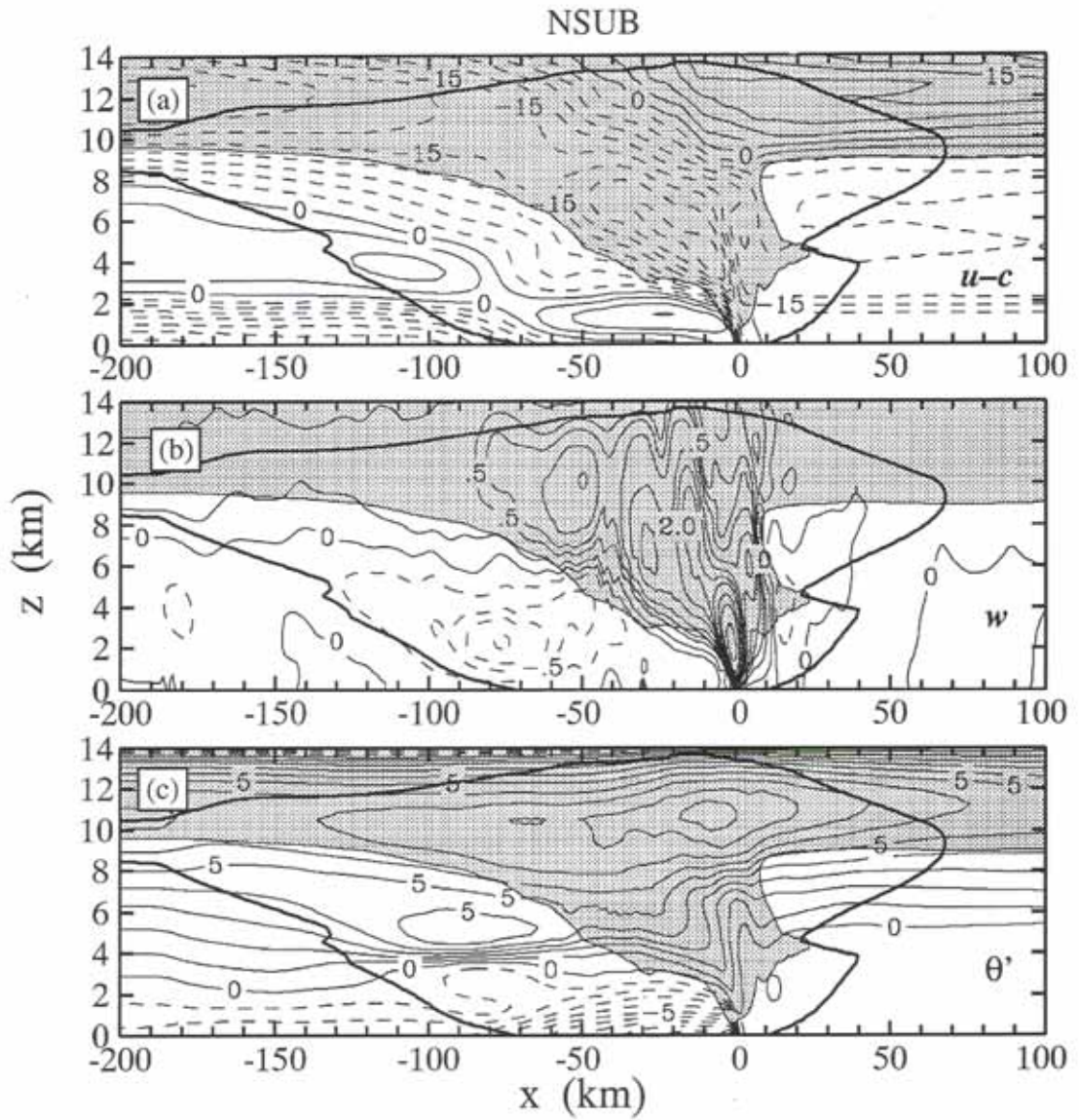
NSUB

Fig. 3.16 Same as Fig. 3.11 except for the NSUB run.
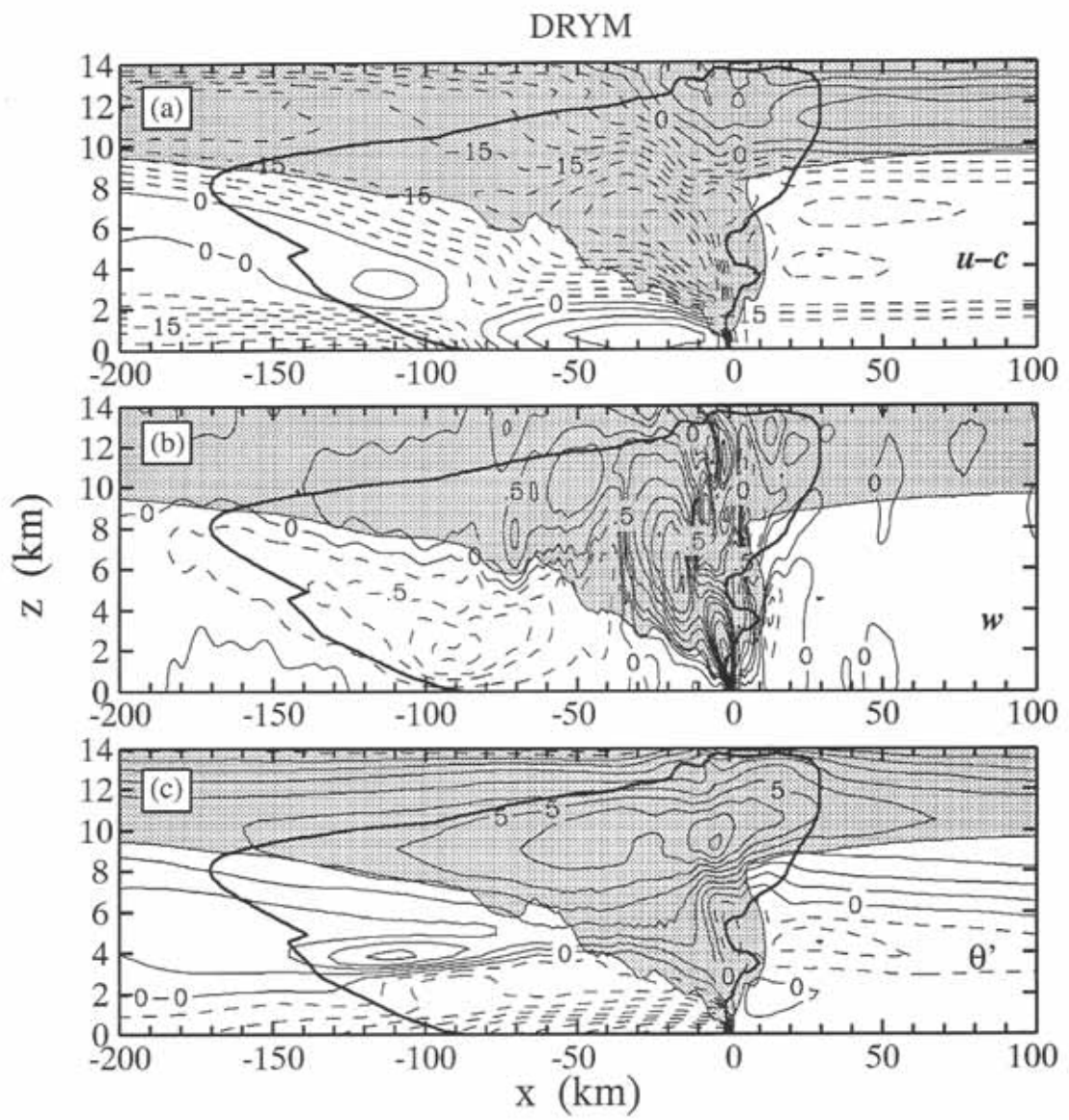
DRYM

Fig. 3.17 Same as Fig. 11 except for the DRYM run.
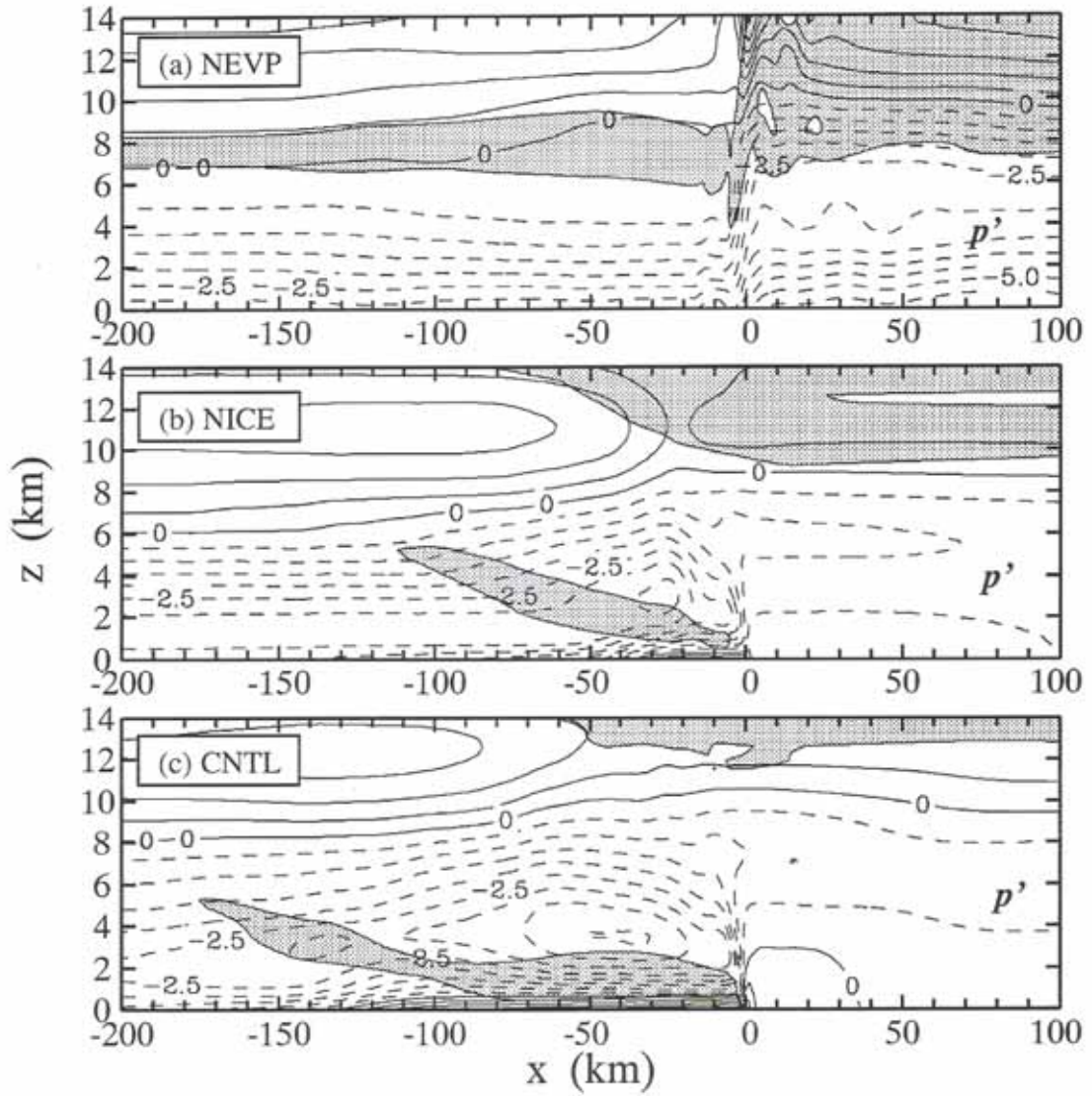
Fig. 3.18 One–hour–averaged ($t = 10$–11 h) pressure perturbation (p'; contour interval is 0.5 mb) of (a) the NEVP run, (b) the NICE run, and (c) the CNTL run. Positive field is in solid lines; the negative field is dashed. Rear–to–front flow greater than 5 m s^{-1} is shaded.
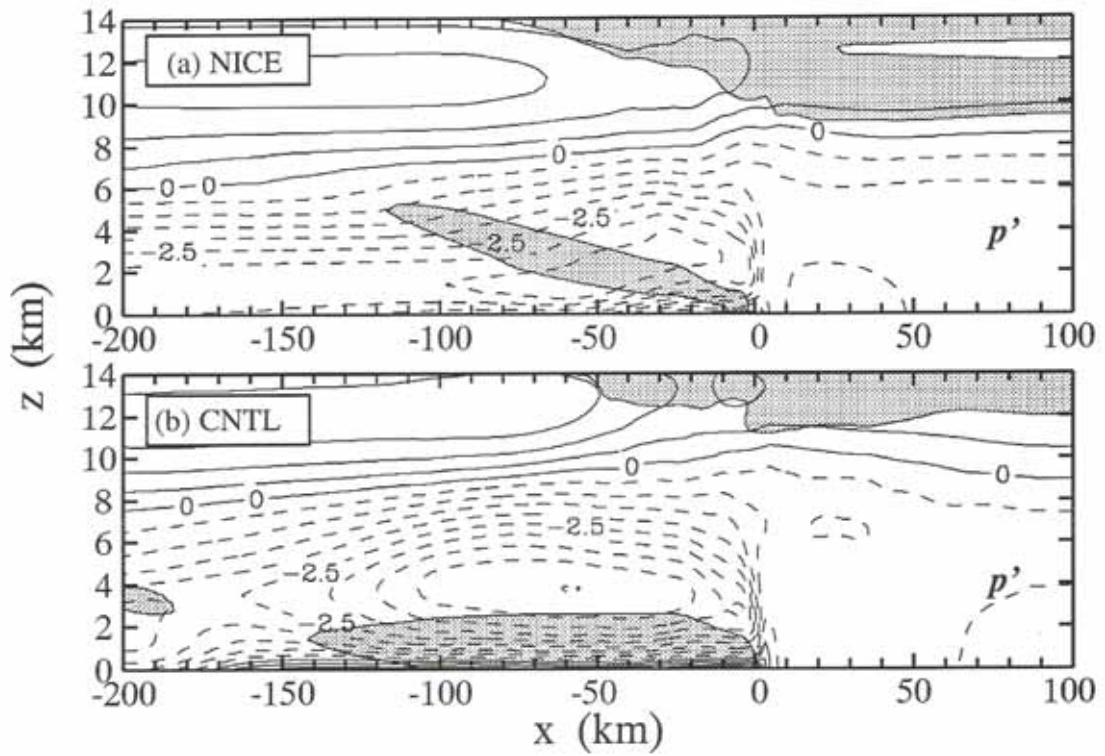
Fig. 3.19 One–hour–averaged (t = 12.5–13.5 h) pressure perturbation (p'; contour interval is 0.5 mb) of (a) the NICE run and (b) the CNTL run. Positive field is in solid lines; negative field is dashed. Rear–fo–front flow greater than 5 m s^{-1} is shaded.

CHAPTER 4

MOMENTUM BUDGET

4.1 Background

Schneider and Lindzen (1976) and Stevens et al. (1977) pointed out the importance of vertical momentum transport by deep convection in large-scale dynamics. For many convective clouds, convective momentum transport may be downgradient, reducing the wind shear of mean flow as predicted by the mixing-length theory. However, Moncrieff (1981) showed that organized deep convective systems (like squall lines) could transport momentum in a countergradient sense, increasing the wind shear of large-scale mean flow. This countergradient momentum transport associated with organized deep convection must be accounted for in cumulus parameterization schemes in mesoscale and large-scale numerical models.

Observations of tropical squall lines show that the vertical flux of horizontal momentum is countergradient in the cross-line direction and downgradient in the along-line direction (LeMone 1983; LeMone et al. 1984). Gao et al. (1990) obtained a similar result in a mesoscale model (MM4) simulation of the 10-11 June 1985 squall line in PRE-STORM (Cunning 1986). They investigated the meso-β-scale[1] momentum budget and its effects on large-scale mean flow, and found that cross-line momentum generation was the strongest contributor to the momentum budget. Convectively generated downdrafts were as important as updrafts in vertically transporting horizontal momentum within both the convective and stratiform regions.

Gallus and Johnson (1992) used rawinsonde data to diagnose the momentum fluxes and tendencies in the 10-11 June 1985 squall line observed in PRE-STORM. They found a strong midlevel mesolow, which contributed to the rear-to-front (RTF) tendency in the vicinity of a rear inflow jet. This mesolow also led to a strong front-to-rear (FTR) tendency elsewhere through most of the storm. The vertical flux of cross-line momentum in the convective region during the mature and dissipating stages was countergradient, in agreement with previous studies of LeMone et al. (1984) and Gao et al. (1990). However, the rawinsonde data they used did not fully resolve the leading convective region.

---

[1]Meso-β-scale is defined by Orlanski (1975) as a horizontal dimension of 20–200 km.

LeMone and Moncrieff (1994) investigated the effects of quasi-two-dimensional convective bands on the environmental flow by comparing observed mass fluxes, momentum fluxes, and horizontal pressure changes to those predicted by the idealized dynamical model of Moncrieff (1992). Despite assumptions of two dimensionality, steady state, and no Coriolis or buoyancy effects, Moncrieff's (1992) model successfully predicted both the amplitude and shape of vertical mass and momentum fluxes for mesoscale convective systems (MCSs) in near-neutral environments (low buoyancy or high shear) and with system width-to-depth ratios close to the value of 4:1. However, the model was less successful for systems in more unstable environments or those with large horizontal extent, probably because of the neglect of the generation of horizontal momentum by buoyancy.

Within certain squall-type MCSs, the leading-convective region and the trailing-stratiform precipitation region are kinematically and microphysically different (Zipser 1969, 1977; Houze 1977, 1989; Hauser and Amayenc 1986; Biggerstaff and Houze 1991a, b, 1993; Braun and Houze 1994a, b, 1995a, b). The momentum balance and transport within these two physically distinct regions may also be quite different. The objective of Chapter 4 is to investigate the momentum budget of a midlatitude squall line to gain insight into the contributions of different subregions of the squall-type MCS to the momentum budget of a large-scale region containing the storm. For this purpose, we divide the storm horizontally into four physically distinct regions—convective precipitation region, stratiform precipitation region, rear anvil, and forward anvil—and calculate the momentum tendency as a function of height in each region. Within each region we determine the contributions to the momentum tendency by horizontal pressure-gradient accelerations and by convergence of mean and eddy fluxes of momentum.

Although the momentum budget of the 10-11 June squall line has been investigated previously, both numerically (Gao et al. 1990) and observationally (Gallus and Johnson 1992), none of these studies has completely addressed the objectives of Chapter 4. We make use of the two-dimensional numerical simulation results of the high-resolution nonhydrostatic cloud model discussed in Chapters 2 and 3. The very high spatial and temporal resolution ($\Delta x = 1$ km, $\Delta t = 6$ s) of this model provides detailed insights into the convective-scale processes, which are essential in the momentum generation and transport of the intense 10-11 June squall line. Most of Chapter 4 is based on Yang and Houze (1995c).

4.2 Subregional contributions to the large-scale mean horizontal and vertical velocity fields

The evolution of the simulated kinematic, thermodynamic, and pressure structure of the 2D control (CNTL) storm is described and discussed in Section 3.2 (referred to Figs. 3.4–3.7). In this section, we will consider the subregional contributions to the large-scale mean horizontal and vertical velocity fields. Consider a 300-km-wide large-scale area A containing the simulated squall line like the fine mesh domain shown in Figs. 3.4–3.7. The large-scale area A can be decomposed into four subregions

$$A = A_{CV} + A_{SF} + A_{RA} + A_{FA} \qquad (4.1)$$

where A_{CV}, A_{SF}, A_{RA}, A_{FA} are areas covered by convective precipitation (CV), stratiform precipitation (SF), rear anvil (RA), and forward anvil (FA), respectively. Then the area average of a physical quantity I over the large-scale area A can be written as

$$[I] = \sigma_{CV}\langle I\rangle_{CV} + \sigma_{SF}\langle I\rangle_{SF} + \sigma_{RA}\langle I\rangle_{RA} + \sigma_{FA}\langle I\rangle_{FA} \qquad (4.2)$$

where $[I]$ is the average of I over the large-scale area A; σ_{CV}, σ_{SF}, σ_{RA}, and σ_{FA} are fractions of large-scale area A covered by regions of convective precipitation (CV), stratiform precipitation (SF), rear anvil (RA), and forward anvil (FA), respectively (indicated in Table 4.1); $\langle I\rangle_{CV}$, $\langle I\rangle_{SF}$, $\langle I\rangle_{RA}$, and $\langle I\rangle_{FA}$ are the averages of I over the corresponding subregions.

Figure 4.1 shows the large-scale-averaged vertical velocity [$I = w$ in (4.2)] and the contributions of subregions [terms on the right of (4.2)] during the mature stage of the storm. The vertical velocity averaged over the convective region (CV profile) is positive at all levels with a maximum value near $z = 4$ km. The vertical velocity averaged over the stratiform region (SF profile) shows mean ascent (the mesoscale updraft) in the upper troposphere ($z > 5.5$ km) and mean descent (the mesoscale downdraft) in the lower troposphere ($z < 5.5$ km). The area-weighted vertical velocity in the rear anvil region (RA profile) has a mean downdraft peaked near $z = 5$ km, corresponding to the descending rear inflow, and weak upward motion above ($z > 7.5$ km). The area-weighted vertical velocity in the forward anvil region (FA profile) shows a weak updraft peaked near the top of the boundary layer ($z = 1.5$ km), favorable for the development of new convective cells ahead of the gust front.

The vertical velocity averaged over the large-scale area A (Total profile) shows a mean updraft. As noted by Houze (1982, 1989), the large-scale ascent peaks at a higher level than that in the convective region (CV profile), owing to the effect of mesoscale updraft/downdraft in the stratiform region (SF profile).

Figure 4.2 shows the contributions to the large-scale-averaged storm-relative horizontal wind [$I = u-c$ in (4.2)] by the four storm subregions during the mature stage. The large-scale horizontal wind (Total profile) is mainly determined by the stratiform region (SF profile), which shows strong FTR flow at midlevels and RTF flow at low levels, while the contributions from other regions are small.

4.3 Evolution of momentum generation and advection processes

4.3.1 Time-averaged momentum equation

The horizontal momentum equation in a coordinate system moving with the squall line can be written as

$$\frac{\delta u_s}{\delta t} = \frac{\partial u_s}{\partial t} + c\frac{\partial u_s}{\partial x} = -c_p\theta_{vo}\frac{\partial \pi}{\partial x} - u_s\frac{\partial u_s}{\partial x} - w\frac{\partial u_s}{\partial z} + D_u \qquad (4.3)$$

TEN   PGF   HAD   VAD   TRB

where

$$u_s = u - c \qquad (4.4)$$

u is the ground-relative horizontal wind, c is the storm propagation speed, u_s is the storm-relative horizontal wind, x and z are the horizontal and vertical coordinates, respectively; $\delta/\delta t$ is the local derivative (or tendency, TEN) in the moving coordinate system, w is the vertical velocity, c_p is the specific heat at constant pressure, θ_{vo} is the basic-state virtual potential temperature, π is the nondimensional pressure perturbation, and D_u is the subgrid-scale turbulent mixing. A detailed derivation of equation (4.3) is given in Klemp and Wilhelmson (1978). Terms on the right-hand side of (4.3) are pressure-gradient force (PGF) per unit mass, horizontal advection (HAD), vertical advection (VAD), and subgrid-scale turbulence (TRB). Note that the Coriolis force is not included.

The time-averaged form of (4.3) is

$$\overline{\frac{\delta u_s}{\delta t}} = -\overline{c_p \theta_{vo} \frac{\partial \pi}{\partial x}} - \overline{u_s \frac{\partial u_s}{\partial x}} - \overline{w \frac{\partial u_s}{\partial z}} + \overline{D_u} \tag{4.5}$$

where

$$\overline{(\ )} \equiv \frac{1}{T} \int_0^T (\ )dt \tag{4.6}$$

and T is some finite time period. We let $T = 1$ h, and we take averages over three stages of the storm's lifetime: the *initial* stage ($t = 7.5$–8.5 h), *mature* stage ($t = 10$–11 h), and *slowly decaying* stage ($t = 12.5$–13.5 h). The time resolution of the model output used to calculate the one-hour averages in (4.5) is 2 min.

4.3.2 Initial stage

Figure 4.3 shows the spatial distribution of one-hour-averaged momentum tendency (TEN), pressure gradient force (PGF), and total advection (ADV = HAD + VAD) during the initial stage ($t = 7.5$–8.5 h). To highlight the effects of momentum generation and advection on the horizontal wind field, RTF flow ≥ 3 m s^{-1} is heavily shaded and FTR flow ≤ -18 m s^{-1} is lightly shaded. The detailed horizontal wind field in the initial stage can be found in Fig. 3.4a. Turbulent mixing (TRB) is not shown in Fig. 4.3 since it is generally small, being significant only near the intense convective updrafts or the cloud top (see Fig. 4.6), where mixing associated with entrainment and/or detrainment may be important.

Initially, the storm is characterized by intense convective updrafts at the leading edge and a steep RTF flow penetrating into the low levels at the leading edge from behind (see Figs. 3.4a and 3.5a). The momentum tendency in the convective region ($x = -10$ to 20 km in Fig. 4.3a) appears to be a small residual between large terms (pressure gradient force, horizontal advection, and vertical advection), as indicated by Gao et al. (1990). Behind the convective region ($x < -10$ km), the momentum tendency shows increasing FTR flow within the ascending FTR flow, increasing RTF flow within the descending RTF flow, and increasing FTR flow again within the low-level FTR flow (Fig. 4.3a). That is, these features are all intensifying.

Figure 4.3b shows that the pressure-gradient force accounts for most of the increasing intensity and downward extension of the descending RTF flow. Note that two maximum RTF increases (28 m s^{-1}h^{-1} near $x = -20$ km, $z = 4$ km and 54 m s^{-1}h^{-1} near $x = 5$ km, $z = 3$ km) in Fig. 4.3b are collocated with the two RTF wind maxima in Fig. 3.4a. This result is consistent with previous studies of the 10-11 June storm (Gao et al. 1990; Gallus and Johnson 1992), and it also agrees with the conclusion of Yang and Houze (1995b; see also Chapter 3) that the descending rear inflow is partly a dynamical response to the latent cooling processes of the squall-line system. The pressure-gradient force also accounts for the strong negative tendency within the ascending FTR flow. Note again that two peak FTR tendencies (−116 m s^{-1}h^{-1} near $x = -4$ km, $z = 9$ km and −112 m s^{-1}h^{-1} near $x = 15$ km, $z = 2$ km) by the pressure-gradient force in Fig. 4.3b are also collocated with the two FTR wind maxima in Fig. 3.4a.

In the convective region, total advection (ADV) opposes the momentum changes produced by pressure-gradient force (Fig. 4.3c). Behind the convective region ($x < -10$ km), total advection generally supports the rearward extension of the ascending FTR flow by producing FTR flow change in middle to upper levels.

4.3.3 Mature stage

In the mature stage ($t = 10$–11 h), the simulated squall system was fully developed with pronounced mesoscale airflows (see Figs. 3.4b and 3.5b). In the convective region ($x = 20$ to 50 km in Fig. 4.4a), the tendency field shows RTF increases at middle to upper levels and FTR increases at low to midlevels, although it is hard to see in the tight contour lines (shown more clearly in Fig. 4.6a). In the trailing-stratiform region ($x = -90$ to 20 km in Fig. 4.4a) , the tendency shows a strong local RTF flow increase at upper levels, which results in a weakening of the diverging upper-level flow (see Fig. 3.4b), and a widespread FTR flow increase at midlevels, which implies the rearward extension and increased leaning back of the ascending FTR flow. At low levels, the net tendency in the stratiform region is to increase the RTF flow, inducing the downward penetration of the descending rear inflow.

Pressure-gradient force (in Fig. 4.4b) associated with the midlevel meso-γ-scale low strongly increases FTR flow in the convective region ($x = 20$ to 50 km) and the

forward part of the stratiform region ($x = -10$ to 20 km), thus driving the ascending FTR flow and transporting hydrometeors rearward to form the trailing-stratiform precipitation region. This intense increase of FTR flow (peak negative tendency -333 m s^{-1}h^{-1}), determined by the cloud model simulation with 1-km horizontal resolution, is an order of magnitude greater than that (-25 m s^{-1}h^{-1}; see Fig. 4b of Gao et al. 1990) produced by a mesoscale model simulation with 25-km horizontal resolution or that (-10 m s^{-1}h^{-1} ; see Fig. 7a of Gallus and Johnson 1992) determined from the sounding data with 80-km horizontal resolution. *The enhancement of the pressure-gradient force by a factor of 10–30 in association with the better-resolved convective-scale process (by the cloud model) indicates that convective-scale processes are dominant in the momentum generation by the 10-11 June squall line.*

Pressure-gradient force also produces gentle RTF increase throughout most of the stratiform region ($x = -90$ to -10 km in Fig. 4.4b) to slow down the ascending FTR flow. A weak FTR increase produced by pressure-gradient force is also found at low levels in the stratiform region ($x = -90$ to -60 km in Fig. 4.4b), which drives the low-level FTR flow beneath the intruding rear inflow. The simulated pressure-gradient force in the convective region agrees well with those obtained by Gao et al. (1990; see their Fig. 4b) and Gallus and Johnson (1992; see their Fig. 7a). However, their pressure-gradient force in the stratiform region is mostly FTR, opposite to our result (mostly RTF). Their analysis across the stratiform region may have been affected by the large-scale pressure gradient (associated with a shortwave trough-ridge system aloft; see Figs. 2b and 4b of Gao et al. 1990), which is not included in this cloud model simulation.

Total advection (Fig. 4.4c) shows strong increase of RTF flow in the convective region ($x = 20$ to 50 km), opposing the intense FTR increase produced by pressure-gradient force. Behind the forward part of the stratiform region ($x < -10$ km), total advection produces a FTR flow increase in middle to upper levels, thus inducing the rearward extension and horizontal tilting of the ascending FTR flow. In low levels, the increase of RTF flow by total advection reflects the downward penetration of the descending rear inflow.

4.3.4 Slowly decaying stage

Because of the assumed constant convectively favorable condition in the prestorm environment, the simulated storm only shows a slow trend of weakening or decay in the late stage (t = 12.5–13.5 h). The overall distribution of the momentum generation and advection processes during the slowly decaying stage (Fig. 4.5) exhibits a more weakly organized but qualitatively similar structure to that in the mature stage (Fig. 4.4).

4.4 Area-average momentum balances

Let [ ] represent an area average over the 300-km-wide area A where the squall line is embedded. It is given by

$$[(\ )] \equiv \frac{1}{L}\int_0^L (\ )\, dx \qquad (4.7)$$

Let $\langle\ \rangle_i$ represent an average over a subregion i of the total domain A. Applying [ ] to (4.5), we obtain

$$\left[\frac{\delta u_s}{\delta t}\right] = \sum_i \left(-\sigma_i \left\langle \overline{c_p \theta_{vo} \frac{\partial \pi}{\partial x}} \right\rangle_i - \sigma_i \left\langle \overline{u_s \frac{\partial u_s}{\partial x}} \right\rangle_i - \sigma_i \left\langle \overline{w \frac{\partial u_s}{\partial z}} \right\rangle_i + \sigma_i \left\langle \overline{D_u} \right\rangle_i \right) \qquad (4.8)$$

where the summation is over all the subregions represented in (4.1) (i represents the four regions FA, CV, SF, and RA). The factor σ_i is the fraction of the total domain A covered by subregion i.

The relative roles of the terms in (4.8) are qualitatively similar in each of the stages of the squall line's development. Therefore, for the remainder of the discussion in Chapter 4, we examine only the large-scale budget of the mature stage.

Figure 4.6a shows the convective-region contribution to the terms on the right-hand side of (4.8) for the mature stage (t = 10–11h). The pressure-gradient force (PGF) produces a strong FTR (negative) tendency in the lower and middle levels ($0 < z < 8.5$ km) and weak RTF (positive) tendency in upper levels ($z > 8.5$ km). This pressure-gradient force has a qualitatively similar profile to those of Gao et al. (1990; see their Fig. 9a) and Gallus and Johnson (1992; see their Fig. 15a), although their profiles remain negative above 320 mb (~8.5 km). Horizontal advection (HAD) is roughly out of phase with

vertical advection (VAD), consistent with Gao et al. (1990; see their Figs. 4a and 4c) and Caniaux et al. (1995; see their Fig. 21a). Subgrid-scale turbulent mixing (TRB) is the smallest effect. *The net tendency (TEN) is a small residual among other forcing terms*, and it is FTR (negative) in lower levels (below 4 km) and RTF (positive) at midlevels (4 km < z < 8 km).

The area-weighted u-momentum terms in the stratiform region (Fig. 4.6b) have similar magnitudes to their convective counterparts (Fig. 4.6a); however, their vertical profiles are quite different. The pressure-gradient force (PGF) in the stratiform region generates RTF tendency throughout the entire troposphere except at lower levels (below 2 km). Horizontal advection (HAD) oscillates in the vertical but again is strongly out of phase with vertical advection (VAD). Subgrid-scale turbulent mixing (TRB) is again the smallest term. The net tendency (TEN) in the stratiform region dominates over that in all the other subregions; thus, *calculation of the correct momentum tendency in the stratiform region is essential to computing the overall effect of the storm on the large-scale momentum field*. The net tendency in the stratiform region is RTF (positive) in lower (z < 2 km) and upper levels (z > 10 km), and FTR (negative) in between (2 km < z < 10 km), which is consistent with Gallus and Johnson (1992; see their Fig. 18a). This net tendency indicates the horizontal tilting of the ascending FTR flow and the downward penetration of the descending rear inflow in the stratiform region.

Figures 4.6c and 4.6d show the effects of the rear and forward anvil regions on the large-scale u-momentum tendency. Their effects on the large-scale tendency are generally less than those of the convective and stratiform regions. The curves in Figs. 4.6c–d generally show variations hovering around the zero-acceleration axis while the curves in Figs. 4.6a–b show much wider fluctuations. The contributions of net tendency (TEN) by the rear and forward anvil regions are not, however, negligible compared to the net tendency in the stratiform region. The rear anvil region contributes positive TEN at low levels, which reinforces that of the stratiform region. Both the rear and forward anvil regions contribute negative TEN between 7 and 10 km altitude, which reinforces the negative TEN at those levels in the stratiform region.

Figure 4.7 shows the large-scale u-momentum budget. The curve labeled TEN is the left-hand side of (4.8). The curves labeled PGF, HAD, VAD, and TRB are the four terms on the right-hand side of (4.8), in the order that they appear on the right of (4.8) and

after they are summed over the four subregions of the domain (FA, CV, SF, and RA). Figure 4.7 shows that, over the large-scale area A, pressure-gradient force (PGF) generates FTR tendency in low- to midlevels ($z < 6.5$ km) and RTF tendency above ($z > 6.5$ km). The vertical advection (VAD) increases RTF flow in low levels ($z < 4.5$ km) and FTR flow above ($z > 4.5$ km). The horizontal advection (HAD) produces an increase of RTF flow in upper levels ($z > 8$ km) and a weak increase of FTR flow in mid- to lower levels ($z < 8$ km). The net momentum tendency (TEN) over the large-scale area A is RTF in lower ($z < 3.5$ km) and upper levels ($z > 10.5$ km), and FTR in midlevels (3.5 km $< z <$ 10.5 km). This vertical profile is similar to that of the stratiform region (TEN curve in Fig. 4.6b). Figures 4.6 and 4.7 thus show, as anticipated above, that *the stratiform region determines the net momentum tendency of the large-scale area A.*

4.5 Impact of momentum flux on mean flow

We can rewrite the momentum equation in flux form by combining it with the mass-continuity equation. When we do this (in Section 4.6), we obtain terms involving the fluxes by both the mean flow and eddy motion. The large-scale mean flow then changes according to the convergence of these fluxes in concert with pressure-gradient force. Therefore, we will discuss the momentum flux and its impact on large-scale mean flow in this section.

4.5.1 Formulation of momentum flux

Means and perturbation quantities of a velocity component V ($V = u$ or w) are defined as

$$V = \overline{V} + V' \tag{4.9}$$

and

$$V = [V] + V^* \tag{4.10}$$

where $\overline{V}$ in (4.9) is the time average defined by (4.6), and $[V]$ in (4.10) is the spatial average defined by (4.7). In (4.6) and (4.7), $T = 1$ h for each of the three lifecycle stages of the storm, and $L = 300$ km for the large-scale area A in which the storm is embedded. Following Priestly (1949) for the decomposition of large-scale heat fluxes in general

circulations, we decompose the total vertical flux of storm-relative horizontal momentum $\rho_o[\overline{u_s w}]$ into three physically distinct parts,

$$\rho_o[\overline{u_s w}] = \rho_o[\overline{u_s}][\overline{w}] + \rho_o[\overline{u_s}^* \overline{w}^*] + \rho_o[\overline{u_s' w'}]$$ (4.11)

$$T_{ot} \qquad S_m \qquad S_e \qquad T_e$$

where ρ_o is the basic-state density, $\rho_o[\overline{u_s}][\overline{w}]$ is the momentum transport by steady mean flow (S_m), $\rho_o[\overline{u_s}^* \overline{w}^*]$ is the transport by standing eddies (S_e), and $\rho_o[\overline{u_s' w'}]$ is the transport by transient eddies (T_e).

4.5.2 Vertical profile of momentum flux over the large-scale area

Figure 4.8 shows each component of total momentum flux in (4.11) averaged temporally during the mature stage ($t = 10$–11 h) and spatially over the large-scale area A. In Fig. 4.8, the momentum transport by steady mean flow (S_m curve) prevails in middle to upper levels ($z > 6.5$ km) but the transport by standing eddies (S_e curve) dominates in low to midlevels ($z < 6.5$ km). *The transport by steady mean flow accounts for most of the total momentum transport in middle to upper levels*, indicating that airflow is "relatively homogeneous" in the middle to upper troposphere. On the other hand, *standing-eddy transport accounts for most of the total momentum transport in lower to middle levels*. Transport by transient eddies (T_e curve) is the smallest. The decomposition of total momentum flux into its three physically different modes for the 10-11 June squall line has not been shown before; however, similar results were found by Caniaux et al. (1995) for a tropical western Africa squall line with a broad trailing-stratiform precipitation region (see their Figs. 19 and 20).

The predominance of total momentum transport by the two-dimensional steady-state circulation [S_m and S_e in (4.11)] during the mature stage seems to justify the key assumptions of Moncrieff's (1992) idealized model: steady state and two dimensionality. Therefore, it may be appropriate to use Moncrieff's paradigm of the airflow associated with organized convection in a squall-type MCS, if the storm is similar to the simulated squall line. However, the simulation in this study is verified against the data for only that portion of the 10-11 June squall line that exhibited the most ideal two-dimensional structure within the larger storm system (see discussion in Sec. 3a of Biggerstaff and Houze 1993). In

portions of the storm better described by three-dimensional dynamics (Skamarock et al. 1994), the momentum budget may have different characteristics.

4.5.3 Contributions by storm subregions to momentum flux

Figure 4.9 shows the mature-stage vertical momentum flux by standing eddies [S_e in (4.11)]. The vertical convergence of this eddy flux has a strong impact on the large-scale momentum tendency (to be discussed in Section 4.6). The convective region (CV curve) contributes 65–75% of the total vertical momentum flux (Total curve). Because of the persistent upshear tilt of updrafts in the convective region, convection transports FTR momentum upward. Hence, the storm-relative momentum flux by standing eddies in the convective region is negative. Sounding data from the 10-11 June storm also indicated negative momentum fluxes over the convective region and the entire squall system (Gallus and Johnson 1992; see their Fig. 19). Normalized by areal fraction, their fluxes were weaker than ours (especially for the convective-region flux, which is weaker than ours by a factor of 4–10). Evidently, the sounding data cannot fully resolve the detailed convective-scale processes.

The stratiform region, forward anvil, and rear anvil (SF, FA, and RA curves in Fig. 4.9) contribute weakly to the standing-eddy momentum flux. Most is accounted for by the convective-region contribution. The direction of total vertical eddy flux of momentum is countergradient, increasing the wind shear of mean flow with time (not shown).

4.6 Large-scale momentum budget

4.6.1 Formulation of time- and space-averaged momentum budget

We now consider the momentum budget of large-scale area A by rewriting the time-averaged u-momentum equation (4.5) in flux form. Combining (4.5) with the anelastic mass continuity equation ($\nabla \cdot \rho_o \mathbf{v} = 0$, where $\mathbf{v}$ is the two-dimensional wind vector) and taking the large-scale average, we obtain

$$\left[\overline{\frac{\delta u_s}{\delta t}} \right] = -\left[\frac{\partial}{\partial x} (\overline{u_s}^2) \right] - \frac{1}{\rho_o} \frac{\partial}{\partial z} (\rho_o [\overline{u_s w}]) - \left[\overline{c_p \theta_{vo} \frac{\partial \pi}{\partial x}} \right] + [\overline{D_u}] \tag{4.12}$$

Neglecting the turbulence term $\left[\overline{D_u}\right]$, ignoring the transient eddy term T_e in (4.11), and substituting (4.11) into (4.12) leads to the time- and space-averaged momentum equation

$$\left[\overline{\frac{\delta u_s}{\delta t}}\right] \approx -\left[\frac{\partial}{\partial x}(\overline{u_s}^2)\right] - \frac{1}{\rho_o}\frac{\partial}{\partial z}(\rho_o[\overline{u_s}][\overline{w}]) - \left[\overline{c_p \theta_{vo}\frac{\partial \pi}{\partial x}}\right] - \frac{1}{\rho_o}\frac{\partial}{\partial z}(\rho_o[\overline{u_s^* w^*}]) \quad (4.13)$$

TEN   HMF   VMF   PGF   EFC

The term on the left of (4.13) is net momentum tendency (TEN), and terms on the right of (4.13) are horizontal flux convergence by mean flow (HMF), vertical flux convergence by mean flow (VMF), pressure-gradient force (PGF), and vertical flux convergence by standing eddies (EFC), respectively.

4.6.2 Pressure-gradient force

First consider the large-scale momentum change produced by the pressure-gradient force [PGF in (4.13)] during the mature stage ($t = 10$–11 h). Figure 4.10 displays the large-scale time- and area-averaged pressure-gradient force and its area-weighted subregional contributions. In the convective region (CV curve), the pressure-gradient force results in FTR tendency in the lower and middle levels ($z < 8$ km) and weak RTF tendency aloft ($z > 8$ km). However, pressure-gradient force in the stratiform region (SF curve) produces FTR tendency in the lower level ($z < 2$ km) and RTF tendency in the middle and upper levels ($z > 2$ km). Over the anvil regions (RA and FA curves), the tendency induced by pressure-gradient force is much weaker than that in the precipitation regions (CV and SF curves). Therefore, over the large-scale area A (Total curve), the convective region contributes most of the FTR pressure-gradient tendency at the lower and midlevels ($z < 6.5$ km), and the stratiform region contributes most of RTF pressure-gradient tendency at mid-to-upper levels ($z > 6.5$ km).

4.6.3 Vertical convergence of eddy flux

Figure 4.11 shows the vertical flux convergence of standing eddies [EFC in (4.13)] and its area-weighted subregional contributions. This figure clearly indicates the dominance of the convective-region contribution (CV curve) to the eddy-flux convergence over the large-scale area A (Total curve). In the convective region, eddy-flux convergence strongly increases RTF flow at low levels ($z < 3.5$ km) and FTR flow at midlevels ($3.5 < z$

< 9 km). Eddy-flux convergence in the stratiform region (SF curve) produces much weaker (by a factor of 3–4) momentum changes than in the convective region; the effect of stratiform-region eddy-flux convergence on the large-scale mean flow is to lower the midlevel (low-level) peak of FTR (RTF) increase produced by the convective region. The convergence of eddy flux associated with the descending rear inflow (near $z = 7$ km) in the rear anvil region (RA curve) results in an increase of RTF flow below ($z < 7$ km) and FTR flow aloft ($z > 7$ km). The eddy flux in the forward anvil region (FA curve) creates momentum changes at much lower levels (FA curve maximum at $z = 1.5$ km in Fig. 4.9), thus producing momentum change at lower levels (RTF increase for $z < 2$ km and FTR increase for 2 km $< z < 4$ km).

4.6.4 Total large-scale momentum tendency

Figure 4.12 shows the net momentum tendency over the large-scale area A and its different physical contributions [terms in (4.13)]. The vertical flux convergence by mean flow (VMF) and standing eddies (EFC) contribute large portions of the large-scale net momentum tendency (TEN) in (4.13). These curves are consistent with those in Fig. 4.7, which shows the same net tendency (TEN) as in Fig. 4.12 but subdivided according to the terms in the advective form of the momentum equation (4.8) instead of the flux form (4.13). VMF and EFC in (4.13) derive primarily from the vertical advection VAD in (4.8), which according to Fig. 4.7 is the dominant term in the advective form of the momentum equation. The horizontal flux convergence by mean flow (HMF) largely comes from the horizontal advection HAD in (4.8), and the vertical profile of HAD in Fig. 4.7 is similar to the profile of HMF in Fig. 4.12.

The flux form of the momentum budget (Fig. 4.12) shows that the eddy flux convergence (EFC) outweighs other terms at low and middle levels. It largely determines the sense of the overall tendency TEN, which is RTF at low levels ($z < 3$ km) and FTR at midlevels (3 km $< z < 10$ km). The pressure-gradient force (PGF) and horizontal flux convergence of mean flow (HMF) together account for the large-scale momentum tendency in upper levels ($z > 10.5$ km).

Figure 4.13 presents a summary of the processes affecting the large-scale momentum tendency produced by the simulated 10-11 June PRESTORM squall line. We will discuss this figure in the context of summary given below.

4.7 Summary

Since our model simulation of the 10-11 June 1985 squall line in PRE-STORM excludes the large-scale horizontal variation of the environment, the calculated momentum generation and transport are produced by the squall line alone (i.e., no large-scale forcing). The very high spatial and temporal resolution ($\Delta x = 1$ km, $\Delta t = 6$ s) of the cloud model provides detailed insight into the convective-scale processes within the system. These small-scale processes are essential in the momentum balance and transport for the 10-11 June storm. For example, the pressure-gradient tendency associated with the meso-γ-scale low within the convective region produces an increase of FTR flow that is a factor of 10–30 greater than that inferred from previous mesoscale budget studies.

When the momentum equation is written in flux form, by combining it with the continuity equation, we obtain terms involving the fluxes by the mean flow and eddy motion. Decomposition of total momentum flux into three physically distinct modes—transports by steady mean flow, standing eddies, and transient eddies—shows that in the middle to upper levels, the transport by steady mean flow contributes most of the total momentum flux, because airflow is relatively uniform at these levels. The transport by standing eddies explains most of the total momentum flux in low to middle levels. Transport by transient eddies is the least important momentum-transport process. The dominance of momentum transport by the two-dimensional steady-state circulation (mean flow plus standing eddies) is consistent with the key assumptions of Moncrieff's (1992) idealized model: steady state and two dimensional.

Figure 4.13b summarizes the momentum tendency over a 300-km-wide large-scale area containing the squall-line system. At lower levels (0–4 km) and upper levels (10–14 km), the net tendency is positive (increasing RTF flow), while at midlevels (4–10 km), the net tendency is negative (increasing FTR flow). Figure 4.13a shows how much each of the four horizontal subregions of the squall line (forward anvil, convective region, stratiform region, rear anvil) contributes to the net momentum tendency over the large-scale area. The arrows in Fig. 4.13 are drawn from the curves in Figs. 4.6, 4.7, 4.9, 4.10, 4.11, and 4.12.

The arrows in Fig. 4.13a show how much each of the processes represented by the terms on the right-hand side of Eq. (4.13) contributes to the net momentum tendency in

Fig. 4.13b, according to altitude and subregion of the storm. The strongest contributions are from the convective and stratiform precipitation zones. The arrows show, however, that no single process or any one subregion of the storm dominates the net momentum tendency over the large-scale area. The contribution from the convective region dominates at low levels, both the convective and stratiform regions contribute significantly to net momentum tendency at midlevels, and the contribution from the stratiform region is essential at upper levels.

Figure 4.13a further shows that the net momentum tendency over the large-scale area (Fig. 4.13b) is the result of competing processes; *the net tendencies are a delicate imbalance of strong terms of opposite sign.* In particular:

- At low levels (0–4 km), the net RTF tendency (Fig. 4.13b) is the result of a competition of two processes in the convective region (Fig. 4.13a). The forward-directed tendency by the standing-eddy flux convergence, which transports low-level (midlevel) FTR (RTF) momentum upward (downward) in the convective updrafts (downdrafts), slightly outweighs the rearward-directed pressure-gradient tendency produced by the meso-γ-scale low under the sloping updrafts (Fig. 3.7b).

- At midlevels (4–10 km), all four subregions contribute to the net FTR tendency shown by the middle box in Fig. 4.13b. The leading process in producing the net FTR tendency is the eddy-flux convergence in the convective region and, to some extent, in the rear anvil region (Fig. 4.13a). The pressure-gradient tendencies (FTR in the convective region and RTF in the stratiform region) tend to cancel out. Vertical flux by the mean flow is not negligible at these levels.

- At upper levels (10–14 km), the convective region (Fig. 4.13a) contributes very little to the overall momentum tendency (Fig. 4.13b). The dominant process is the RTF tendency in the stratiform region produced by the mesohigh aloft centered at 12 km (Fig. 3.7b).

These results show that computations of the large-scale momentum tendency produced by a squall line with a trailing-stratiform region must take into account the internal structure of the storm. All the terms in Eq. (4.13) are significant, and all of the subregions (horizontal and vertical) of the storm contribute uniquely to the net momentum tendency. The contributions by standing eddies and by pressure gradients (convective-scale and

mesoscale) are both large and tend to work in opposite directions so that the resulting net momentum tendency is a small residual between these large terms, which behave differently in each region of the storm. Thus, there appear to be no short cuts to the parameterization of momentum tendencies produced by mesoscale convective systems. Except for transient eddies, which do not produce a strong effect, all the processes of momentum generation and flux are important, and their relative importance varies with both altitude and from one subregion of the storm to the next. While this complexity presents a significant and daunting challenge for parameterizing momentum tendencies by squall lines in large-scale prediction and climate models, the well-defined and repeatable structure of this type of storm increases the tractability of the problem.

Table 4.1 Fractions of the 300-km-wide large-scale area A in Fig. 3.4 covered by subregions in three lifecycle stages of the simulated squall line.

Stages	Convective Precipitation	Stratiform Precipitation	Rear Anvil	Forward Anvil
Initial	0.10	0.10	0.37	0.43
Mature	0.10	0.33	0.24	0.33
Decaying	0.10	0.43	0.20	0.27
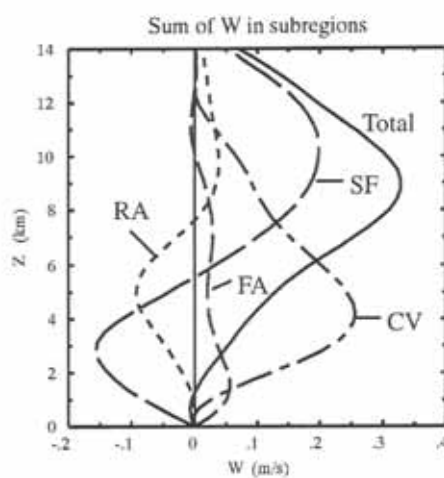
Fig. 4.1 Vertical velocity [$I = w$ in (4.2)] averaged over the large–scale area A (Total curve) and its contributions by convective region (CV curve; $\sigma_{CV}<I>_{CV}$), stratiform region (SF curve; $\sigma_{SF}<I>_{SF}$), rear anvil region (RA curve; $\sigma_{RA}<I>_{RA}$), and forward anvil region (FA curve; $\sigma_{FA}<I>_{FA}$) during the mature stage ($t = 10$–11 h).
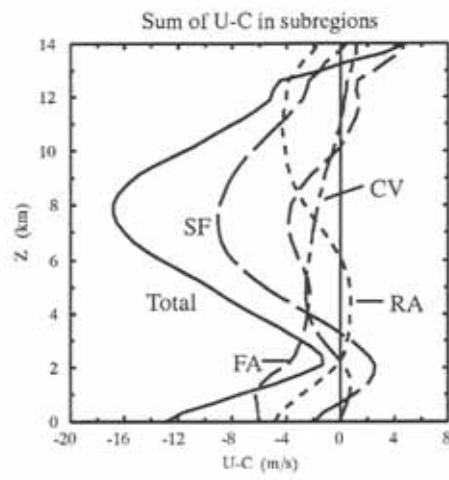
Fig. 4.2 Same as Fig. 4.1 except for the storm–relative horizontal wind [$I = u–c$ in (4.2)] during the mature stage ($t = 10–11$ h).
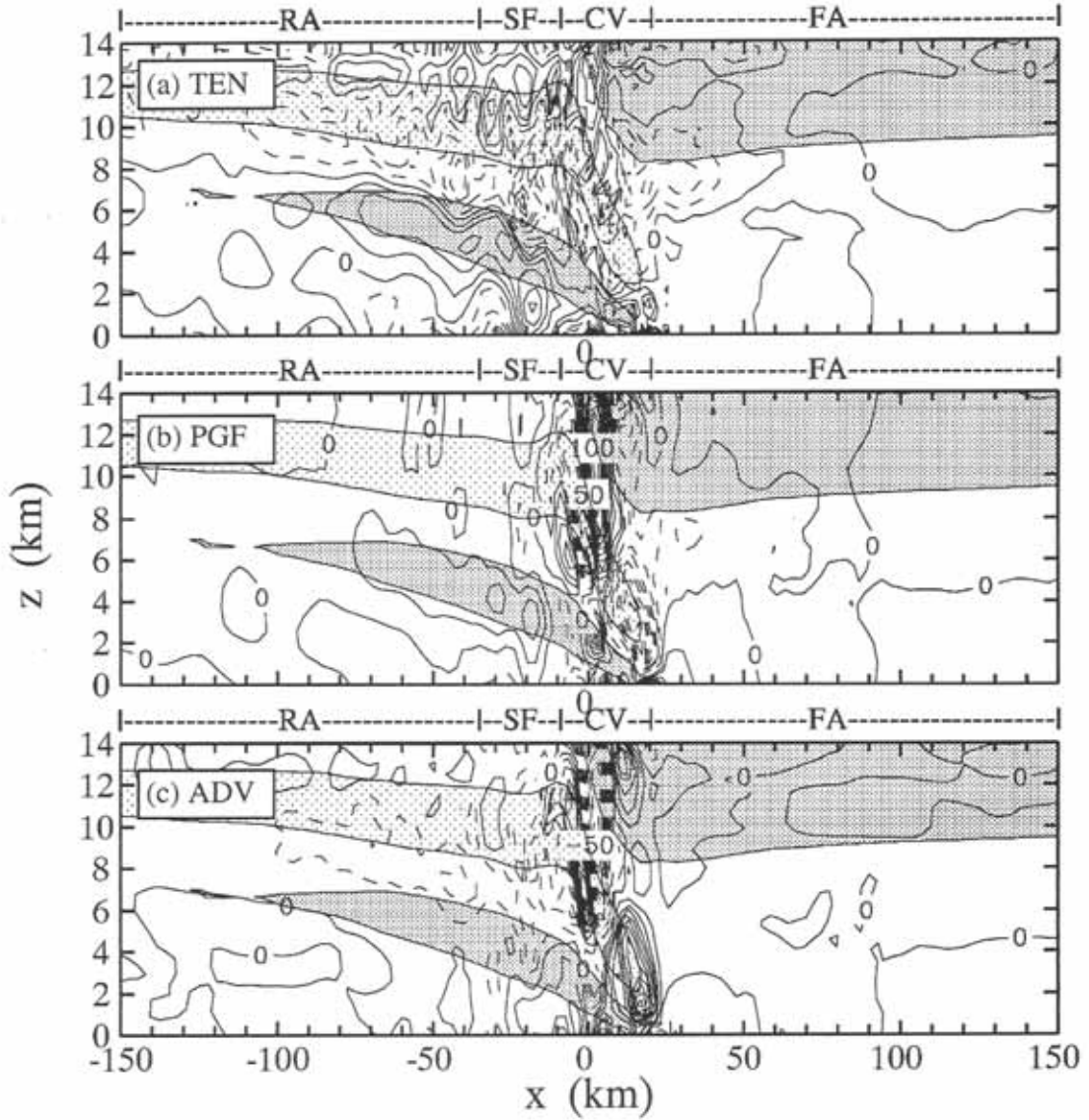
Fig. 4.3 One–hour–averaged fields of (a) net tendency (TEN), (b) pressure–gradient force (PGF), and (c) total advection (ADV) in u–momentum equation (4.5) during the initial stage ($t = 7.5$–8.5 h) of the storm. Contour interval is 5 m s^{-1} h^{-1} in (a) and 10 m s^{-1} h^{-1} in (b)–(c). Positive (RTF) tendency is in solid lines and negative (FTR) tendency is dashed. RTF flow greater than 3 m s^{-1} is heavily shaded, and FTR flow less than –18 m s^{-1} is lightly shaded. Regions of convective precipitation (CV), stratiform precipitation (SF), rear anvil (RA), and forward anvil (FA) are shown in the bar above.
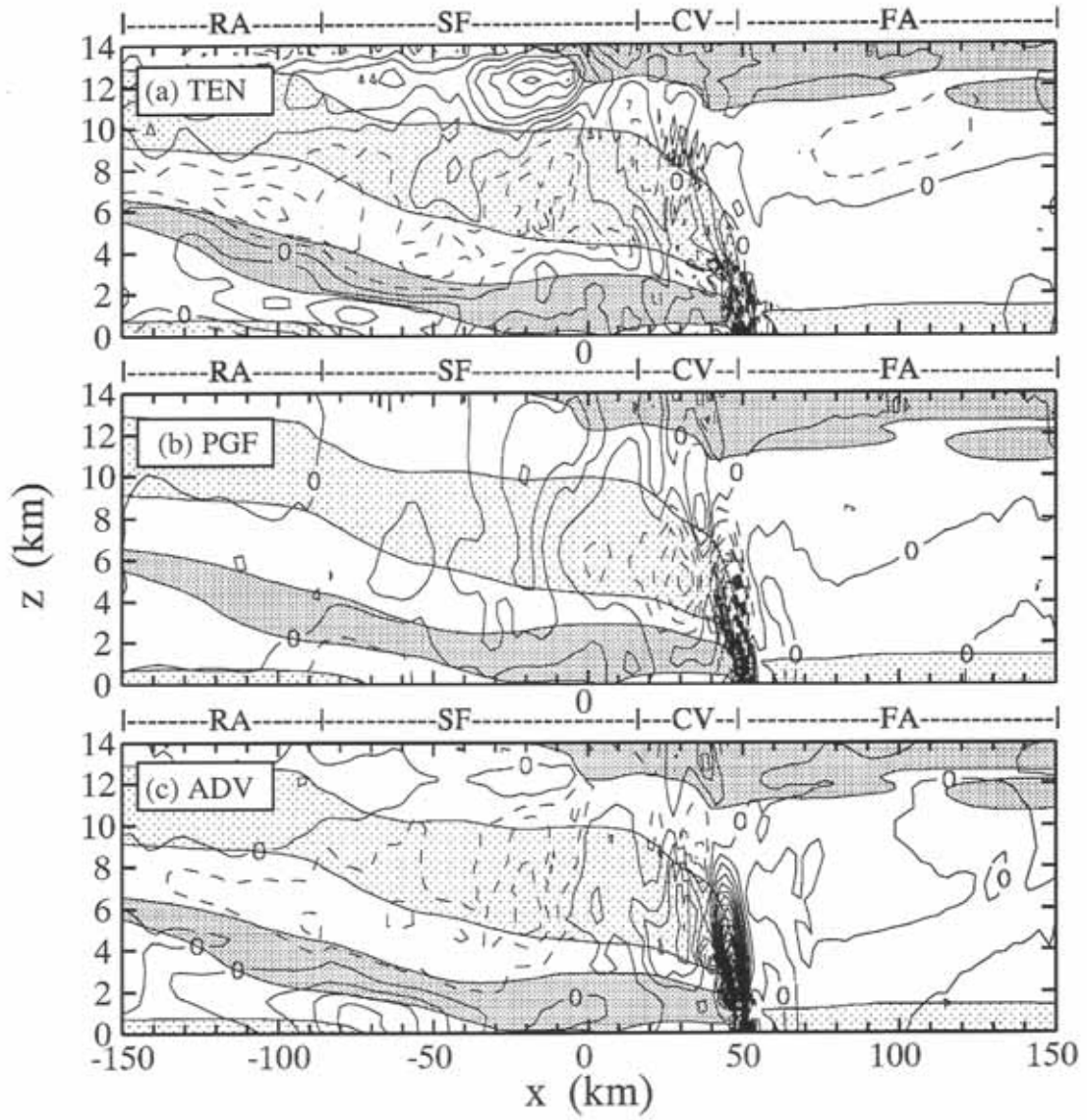
Fig. 4.4 Same as Fig. 4.3 except for terms in u–momentum equation (4.5) averaged in the mature stage ($t = 10$–11 h).
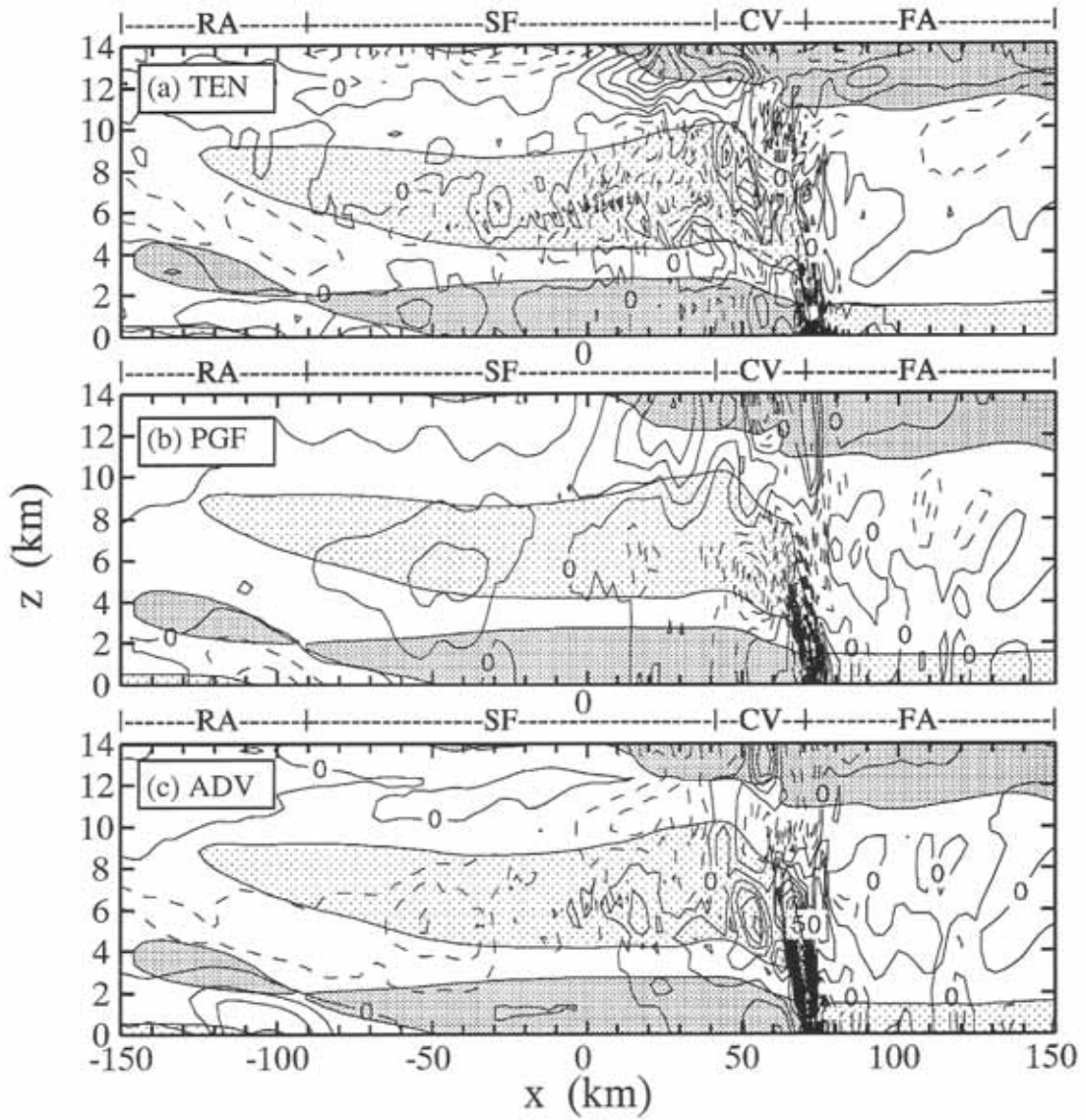
Fig. 4.5 Same as Fig. 4.3 except for terms in u–momentum equation (4.5) averaged in the slowly decaying stage ($t = 12.5$–13.5 h).
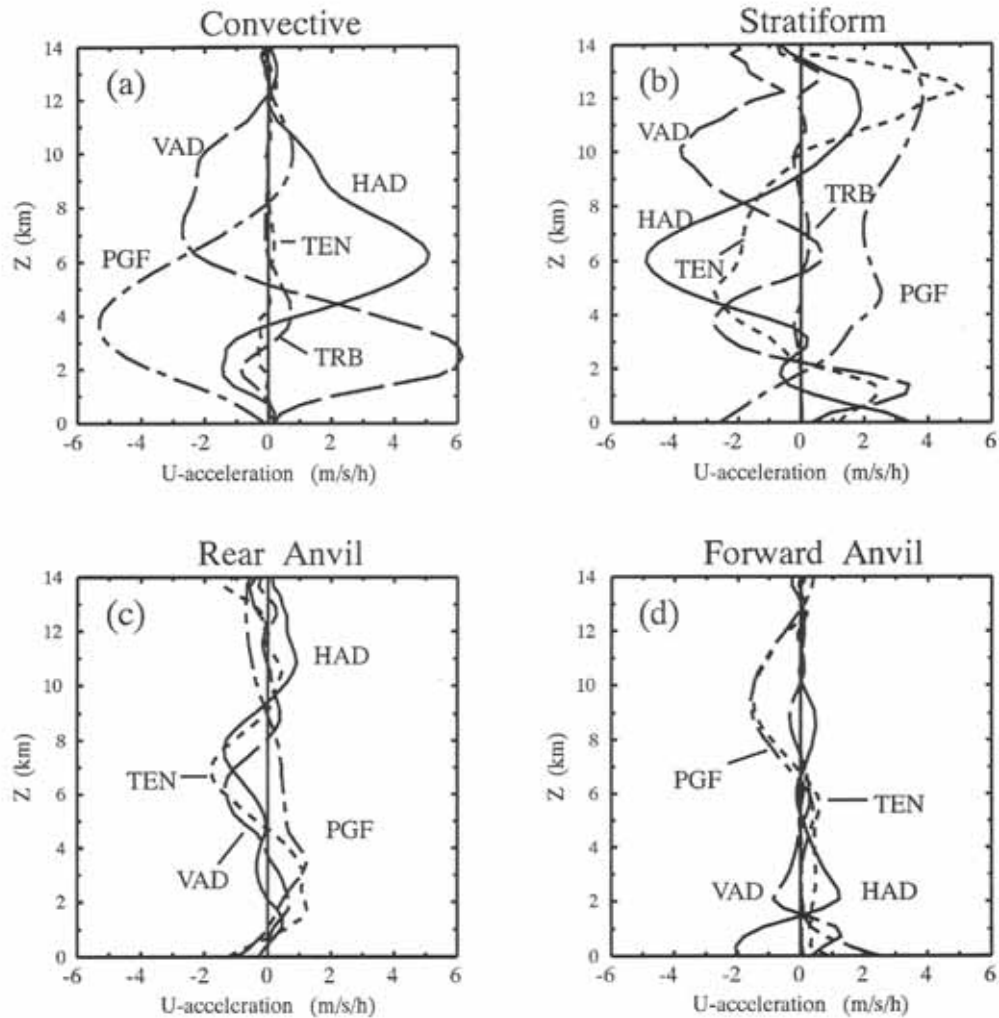
Fig. 4.6 Area–weighted net tendency (TEN), horizontal advection (HAD), vertical advection (VAD), pressure–gradient force (PGF), and turbulent mixing (TRB) in u–momentum equation (4.8) over regions of (a) convective precipitation, (b) stratiform precipitation, (c) rear anvil, and (d) forward anvil during the mature stage ($t = 10$–11 h). Positive acceleration is rear–to–front (RTF) and negative acceleration is front–to–rear (FTR).
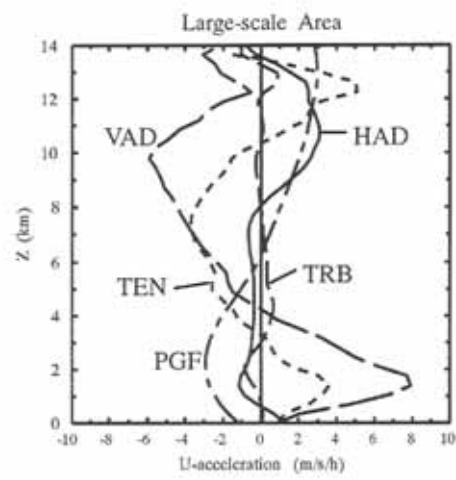
Fig. 4.7 Same as Fig. 4.6 except for terms in u–momentum equation
(4.8) over the large–scale area A during the mature stage ($t = 10$–11 h).
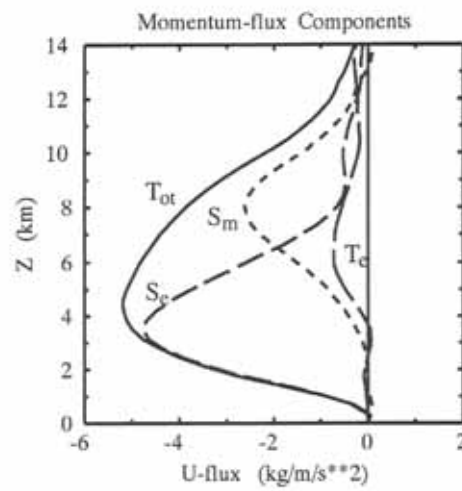
Fig. 4.8 Total vertical flux of storm–relative momentum (T_{ot}) and its three components—the transports by the steady mean flow (S_m), standing eddies (S_e), and transient eddies (T_e) in (4.12)—over the large–scale area A during the mature stage ($t = 10$–11 h).
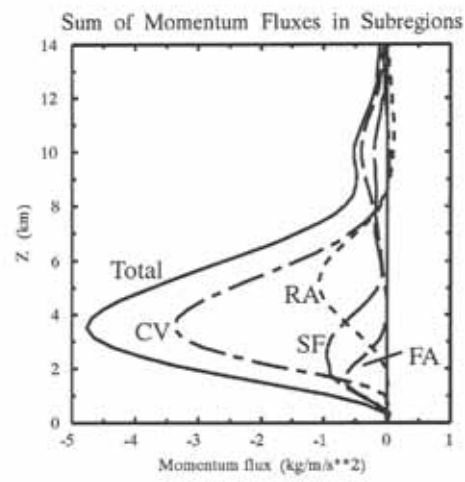
Fig. 4.9 Same as Fig. 4.1 except for the momentum flux by standing eddies [S_e in (4.12)] during the mature stage ($t = 10$–11 h).
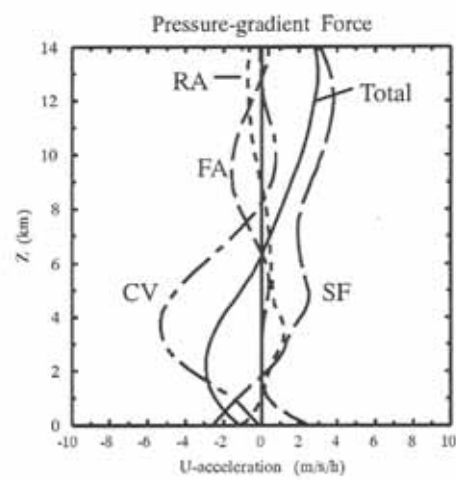
Fig. 4.10 Same as Fig. 4.1 except for the presure–gradient force [PGF in (4.13)] during the mature stage ($t = 10$–11 h).
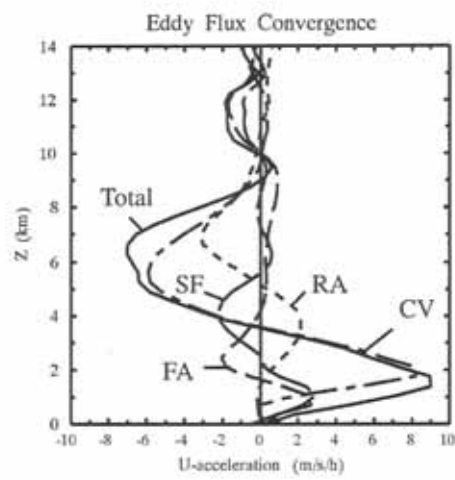
Fig. 4.11 Same as Fig. 4.1 except for the vertical flux convergence of standing eddies [EFC in (4.13)] during the mature stage ($t = 10-11$ h).
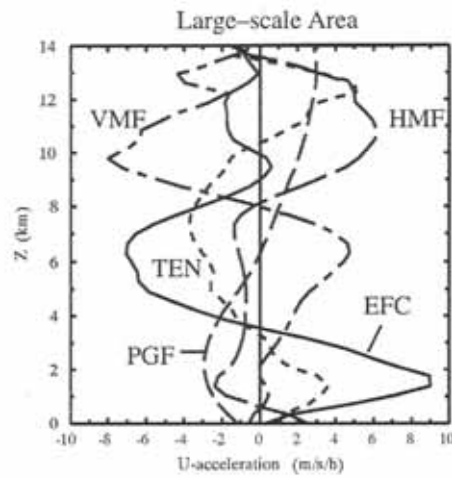
Fig. 4.12 Momentum tendency of large–scale area A by terms in
(4.13)—horizontal flux convergence by mean flow (HMF), vertical
flux convergence by mean flow (VMF), pressure–gradient force
(PGF), vertical flux convergence by standing eddies (EFC), and net
tendency (TEN)—during the mature stage ($t = 10$–11 h).
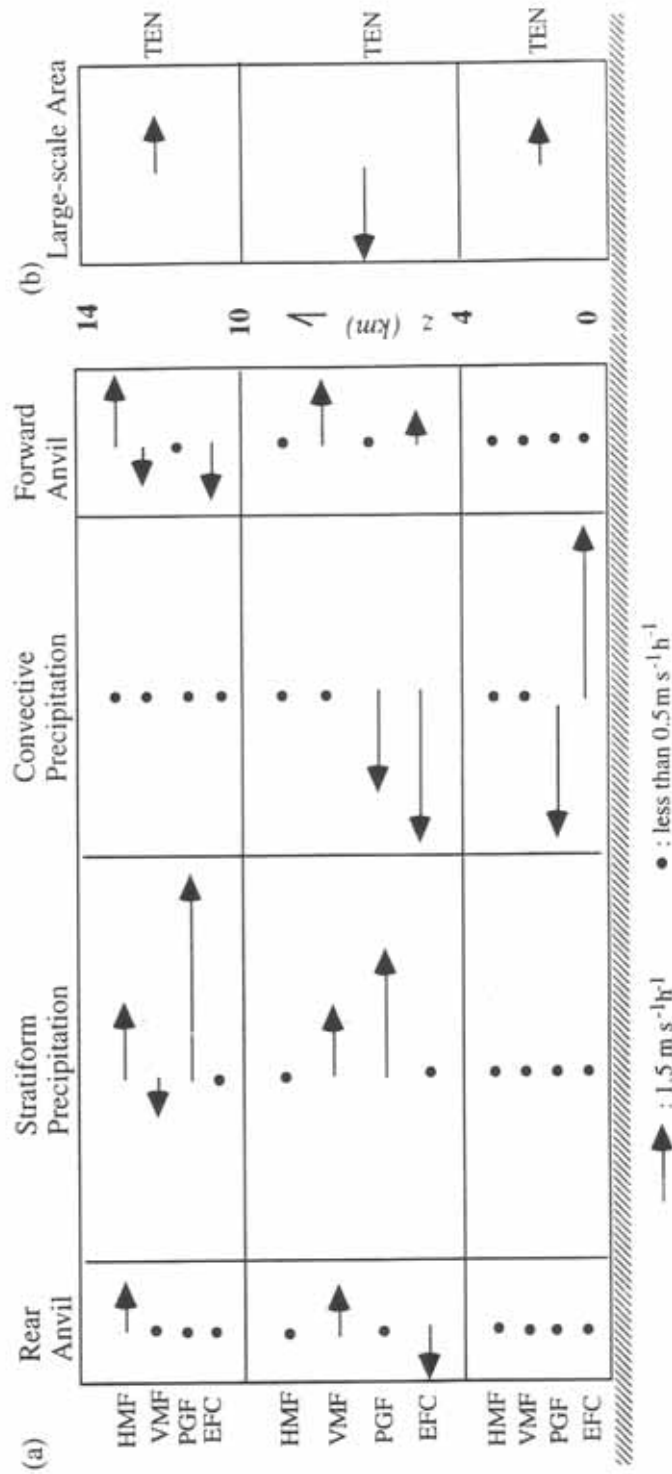
Fig. 4.13 (a) A block diagram showing the balance of momentum–budget terms in (4.13) over four subregions of a large–scale area during the mature stage of the 10–11 June 1985 squall line. Rightward–pointing arrow is for positive (rear–to–front) u–tendency and left-ward–pointing arrow is for negative (front–to–rear) u–tendency. The length of arrow is proportional to the layer–averaged tendency produced by each budget term. A dot is for acceleration less than 0.5 m s^{-1} h^{-1}. (b) is the same as (a) except for the net momentum tendency, the term on the left–hand side of (4.13), over a 300–km–wide large–scale area.

CHAPTER 5

CONCLUSIONS AND SUGGESTIONS FOR FURTHER RESEARCH

Two-dimensional and three-dimensional simulations of the 10-11 June 1985 PRE-STORM squall line with a high-resolution nonhydrostatic model suggest that the multicellular structure of the storm may be associated with gravity waves generated by convection. The convective cells arise as gravity waves are forced by continuous strong low-level convergence at the storm's gust front. The waves propagate to both sides of the gust front. The stronger westward (front-to-rear) mode dominates at the mature stage of the squall line. Continuous low-level updraft is generated at the nose of the cold pool, which propagates at the speed of a density current. Updraft cells periodically break away from this persistent low-level gust-front updraft and move at phase speeds of their associated gravity waves, not at the surrounding airflow speeds as implied by the traditional multicell model.

Linear theory shows that the multicellular structure of the squall line is associated with vertically trapped gravity waves in the troposphere. The waves become trapped in the mid-to-upper troposphere because of the strong decrease of Scorer parameter with height produced by the strong storm-generated vertical wind shear and reduced static stability aloft. Waves are trapped in lower levels because of the rigid ground. The basic characteristics of these trapped tropospheric gravity waves are wavelengths of 16–20 km, storm-relative phase speeds of 20–25 m s^{-1}, and periods of 11–17 min, which are consistent with the generation periods of precipitation cells at the mature stage in the leading portion of the storm. In the trailing-stratiform region, these tropospheric gravity waves become more diffuse with weaker amplitudes, and their wavelengths become longer (25–35 km) with greater storm-relative phase speeds (30–40 m s^{-1}), as described by the dispersion relationship of internal gravity waves.

These tropospheric gravity waves differ from disturbances above the tropopause, which are mechanically forced by convective cells impinging on the tropopause. These waves in the lower stratosphere have the structure of vertically propagating (rather than trapped) gravity waves.

The rear inflow plays a crucial role in supplying potentially cold and dry midlevel air from the environment to aid in the production of the convective and mesoscale downdrafts. Different configurations of the rear inflow (descending or elevated) can increase or decrease the leading-edge updraft and the storm strength, by producing different sign of additional vorticity source in the horizontal-vorticity balance near the gust front.

Seven two-dimensional experimental simulations of the 10-11 June squall line show that the rear inflow and related aspects of storm structure are sensitive to hydrometeor types, ice-phase microphysics, and the midlevel environmental humidity. Without ice-phase microphysics, the model cannot produce realistic air motions or precipitation in the stratiform region. With the occurrence of heavy hailstones, there is no enhanced rear-to-front flow at the back edge of the storm, because of the weak midlevel mesolow in the narrow stratiform region. The structure and strength of the descending rear inflow and the mesoscale downdraft are more sensitive to evaporation than to other latent cooling processes. Latent cooling by melting snow does not initiate the mesoscale downdraft; however, it accounts for at least 25% of the strength of the maximum of rear-to-front flow at the back edge of the storm during the mature stage and enhances the strength of the mesoscale downdraft by 22%. Mesoscale downdraft is initiated above the 0°C level by sublimational cooling. The mesoscale model experiments of Braun (1995) shows that sublimation also increases the intensity of rear-to-front flow at the back edge of the storm. With the environmental midlevel moisture reduced by half, mesoscale downdrafts are 22% stronger, but the maximum of rear-to-front flow at the back edge of the system reaches only 38% of its mature-stage intensity, as a result of a more vertically upright storm orientation, and hence the resultant weaker mesolow. These results indicate that the descending rear inflow is in part a dynamical response to the latent cooling processes in the trailing stratiform region of a squall-line type mesoscale convective system.

Two-dimensional numerical simulation results are also used to study the momentum budget of the 10-11 June storm. The intense pressure gradient associated with the meso-γ-scale low in the convective region, which produces the ascending front-to-rear (FTR) flow of the storm, is 10-30 times stronger than that calculated in previous mesoscale budget studies. This result indicates the importance of convective-scale processes in the generation and transport of momentum in the storm. Advection slows

down the ascending FTR flow. Upward slope of the ascending FTR flow and downward penetration of descending rear-to-front (RTF) flow result from advection in the stratiform part of the storm.

A decomposition of total momentum flux into three physically distinct modes— mean flow, standing eddies, and transient eddies—shows that the momentum transport by mean flow contributes most of the total momentum transport in middle to upper levels. In low to midlevels, the transport by standing eddies is most significant. Transport by transient eddies is the least important. The two-dimensional steady-state circulation thus dominates the total momentum flux by the squall-line system in its mature stage.

The net momentum tendency over a 300-km-wide large-scale area where the squall line is embedded is the combined result of processes occurring primarily in the precipitation regions of the storm (both convective and stratiform). Pressure-gradient force together with the vertical flux convergence by standing eddies determine most of the large-scale momentum tendency. At low levels, these processes are significant only in the convective region, where eddy flux convergence (mostly as the result of downdrafts) produces RTF flow, which is largely but not completely offset by the pressure-gradient force in the FTR direction. At midlevels, significant processes occur in both the convective and stratiform regions; pressure-gradient forces that are important in the convective and stratiform regions are offsetting, and the vertical convergence of standing eddy fluxes in the convective region dominates and produces a net FTR momentum tendency. At upper levels, processes in the convective region are unimportant, and the RTF-directed horizontal pressure-gradient force in the stratiform region dominates.

Several unanswered questions remain from this dissertation study and deserve further research in the future:

- What are the dynamical or microphysical factors determining the gravity-wave oscillation periods and wavelengths? Spectral analysis of the model output may be necessary to obtain the dominant periods/wavelengths and to understand the wave-to-wave nonlinear interaction.

• Can we simulate the storm's precipitation structure realistically without artificially tuning microphysical parameters (i.e., turning off hail generation processes after the initial stage)? A more robust microphysical scheme is needed.

• How representative is the 10-11 June squall line compared to other leading-line trailing-stratiform squall lines in other geographical locations? Results based on current 10-11 June case should be compared with results from other squall-line cases.

• How does the microphysics-radiation interaction affect the mass, moisture, heat, and momentum budgets of the large-scale environment in which the squall line is embedded? A radiation parameterization scheme should be included in the model in order to have a complete understanding of the effects of a mature squall line on its surrounding environment.

REFERENCES

Alexander, M. J., J. R. Holton, and D. R. Durran, 1995: The gravity wave response above deep convection in a squall line simulation. *J. Atmos. Sci.*, **52**, 2212–2226.

Augustine, J. A., and E. J. Zipser, 1987: The use of wind profilers in a mesoscale experiment. *Bull. Amer. Meteor. Soc.*, **68**, 4–17.

Barnes, G. M., and K. Sieckman, 1984: The environment of fast- and slow-moving tropical mesoscale convective cloud lines. *Mon. Wea. Rev.*, **112**, 1782–1794.

Biggerstaff, M. I., and R. A. Houze, Jr., 1991a: Kinematic and precipitation structure of the 10-11 June 1985 squall line. *Mon. Wea. Rev.*, **119**, 3034–3065.

———, and ———, 1991b: Midlevel vorticity structure of the 10-11 June 1985 squall line. *Mon. Wea. Rev.*, **119**, 3066–3079.

———, and ———, 1993: Kinematics and microphysics of the transition zone of the 10-11 June 1985 squall line. *J. Atmos. Sci.*, **50**, 3091–3110.

Bluestein, H. B., and M. H. Jain, 1985: Formation of mesoscale lines of precipitation: Severe squall lines in Oklahoma during spring. *J. Atmos. Sci.*, **42**, 1711–1732.

Braun, S. A., 1995: *Multiscale process interactions associated with a midlatitude squall line*. Ph.D. dissertation. University of Washington, 194 pp.

———, and R. A. Houze, Jr., 1994a: The transition zone and secondary maximum of radar reflectivity behind a midlatitude squall line: Results retrieved from Doppler radar data. *J. Atmos. Sci.*, **51**, 2733–2755.

———, and ———, 1994b: The heat and potential vorticity budgets of a midlatitude squall line. Preprints, *Sixth Conf. on Mesoscale Processes*, Portland, Amer. Meteor. Soc., 335–338.

———, and ———, 1995a: Diagnosis of hydrometeor profiles from area-mean vertical velocity data. *Quart. J. Roy. Meteor. Soc.*, **121**, 23–53.

———, and ———, 1995b: Melting and freezing within a midlatitude mesoscale convective system. *Quart. J. Roy. Meteor. Soc.*, **121**, 55–77.

———, and ———, 1995c: The heat budget of a midlatitude squall line and implications for potential vorticity production. *J. Atmos. Sci.*, conditionally accepted.

Bretherton, F. P., 1966: The propagation of groups of internal gravity waves in a shear flow. *Quart. J. Roy. Meteor. Soc.*, **92**, 466–480.

Brown, J. M., 1979: Mesoscale unsaturated downdrafts driven by rainfall evaporation: A numerical study. *J. Atmos. Sci.*, **36**, 313–338.

Browning, K. A., 1962: Cellular structure of convective storms. *Meteor. Mag.*, **91**, 341–350.

——, 1977: The structure and mechanisms of hailstorms. *Hail: A Review of Hail Science and Hail Suppression*, (G. B. Foote and C. A. Knight, Eds.), American Meteorological Society, Boston, 1–43.

——, J. C. Fankhauser, J.-P. Chalon, P. J. Eccles, R. C. Strauch, F. H. Merrem, D. J. Musil, E. L. May, and W. R. Sand, 1976: Structure of an evolving hailstorm. Part V: Synthesis and implications for hail growth and hail suppression. *Mon. Wea. Rev.*, **104**, 603–610.

Byers, H. R., and R. R. Braham, Jr., 1949: *The Thunderstorm.* Washington, D. C., U. S. Govt. Printing Office, 287 pp.

Caniaux, G., J.-P. Lafore, and J.-L. Redelsperger, 1995: A numerical study of the stratiform region of a fast-moving squall line. Part II: Relationship between mass, pressure, and momentum fields. *J. Atmos. Soc.*, **52**, 331–352.

Chalon, J.-P., J. C. Fankhauser, and P. J. Eccles, 1976: Structure of an evolving hailstorm. Part I: General characteristic and cellular structure. *Mon. Wea. Rev.*, **104**, 564-575.

Chin, H.-N. S., 1994: The impact of the ice phase and radiation on a midlatitude squall line system. *J. Atmos. Sci.*, **51**, 3320–3343.

Chong, M., P. Amayenc, G. Scialom and J. Testud, 1987: A tropical squall line observed during the COPT 81 experiment in West Africa. Part I: kinematic structure inferred from dual-Doppler radar data. *Mon. Wea. Rev.*, **115**, 670–694.

Churchill, D. D., and R. A. Houze, Jr., 1984: Development and structure of winter monsoon cloud clusters on 10 December 1978. *J. Atmos. Sci.*, **41**, 933–960.

Cunning, J. B., 1986: The Oklahoma-Kansas Preliminary Regional Experiment for STORM-Central. *Bull. Amer. Meteor. Soc.*, **67**, 1478–1486.

Doty, K. G., and D. J. Perkey, 1993: Sensitivity of trajectory calculations to the temporal frequency of wind data. *Mon. Wea. Rev.*, **121**, 387–401.

Droegemeier, K. K., and R. B. Wilhelmson, 1985: Three-dimensional numerical modeling of convection produced by interacting thunderstorm outflows. Part I: Control simulation and low-level moisture variations. *J. Atmos. Sci.*, **42**, 2381-2403.

Dudhia, J. M., and M. W. Moncrieff, 1987: A numerical simulation of quasi-stationary tropical convective bands. *Quart. J. Roy. Meteor. Soc.*, **113**, 929–967.

——, ——, and D. W. K. So, 1987: The two-dimensional dynamics of West African squall lines. *Quart. J. Roy. Meteor. Soc.*, **113**, 121–146.

Durran, D. R., 1989: Improving the anelastic approximation. *J. Atmos. Sci.*, **46**, 1453–1461.

———, 1990: Mountain waves and downslope winds. *Atmospheric Processes over Complex Terrain* (W. Blumen, Ed.), American Meteorological Society, Boston, 59–81.

———, and J. B. Klemp, 1982: On the effects of moisture on the Brunt-Väisälä frequency. *J. Atmos. Sci.*, **39**, 2152-2158.

Foote, G. B., and H. W. Frank, 1983: Case study of a hailstorm in Colorado. Part III: Airflow from triple-Doppler measurements. *J. Atmos. Sci.*, **40**, 686-707.

Fovell, R. G., and Y. Ogura, 1988: Numerical simulation of a midlatitude squall line in two dimensions. *J. Atmos. Sci.*, **45**, 3846–3879.

———, and ———., 1989: Effects of vertical wind shears on numerically simulated multicell storm structure. *J. Atmos. Sci.*, **46**, 3144–3176.

———, and P. S. Dailey, 1995: The temporal behavior of numerically simulated multicell-type storm. Part I: Modes of behavior. *J. Atmos. Sci.*, **52**, 2073–2095.

———, D. Durran, and J. R. Holton, 1992: Numerical simulations of convectively generated stratospheric gravity waves. *J. Atmos. Sci.*, **49**, 1427–1442.

Fritsch, J. M., and C. F. Chappell, 1980: Numerical prediction of convectively driven mesoscale pressure system. Part I: Convective parameterization. *J. Atmos. Sci.*, **37**, 1722–1733.

———, R. J. Kane, and C. R. Chelius, 1986: The contribution of mesoscale convective weather systems to the warm-season precipitation in the U.S. *J. Climate Appl. Meteor.*, **25**, 1333–1345.

Fujita, T. T., 1955: Results of detailed synoptic studies of squall lines. *Tellus*, **7**, 405–436.

———, W. L. Ecklund, and D. A. Carter, 1989: Convection waves observed using a VHF wind-profiling Doppler radar during the PRE-STORM experiment. Proceeding, *24th Conf. on Radar Meteor.*, Tallahassee, Fla., 705–708.

Gallus, W. A. Jr., and R. H. Johnson, 1991: Heat and moisture budget of an intense midlatitude squall line. *J. Atmos. Sci.*, **48**, 122-146.

———, and ———, 1992: The momentum budget of an intense midlatitude squall line. *J. Atmos. Sci.*, **49**, 422–450.

———, and ———, 1995a: The dynamics of circulations within the trailing stratiform region of squall lines. Part I: The 10-11 June PRE-STORM system. *J. Atmos. Sci.*, **52**, 2161–2187.

———, and ———, 1995b: The dynamics of circulations within the trailing stratiform region of squall lines. Part II: Influence of the convective line and ambient environment. *J. Atmos. Sci.*, **52**, 2188–2211.

Gamache, J. F., and R. A. Houze, Jr., 1982: Mesoscale air motion associated with a tropical squall line. *Mon. Wea. Rev.*, **110**, 118–135.

———, and ———, 1985: Further analysis of the composite wind and thermodynamic structure of the 12 September GATE squall line. *Mon. Wea. Rev.*, **113**, 1241–1259.

Gao, K., D.-L. Zhang, M. W. Moncrieff and H.-R. Cho, 1990: Mesoscale momentum budget in a midlatitude squall line: A numerical case study. *Mon. Wea. Rev.*, **118**, 1011-1028.

Gill, A. E., 1982: *Atmosphere-Ocean Dynamics*. Academic Press, 662 pp.

Hamilton, R. A., and J. W. Archbold, 1945: Meteorology of Nigeria and adjacent territory. *Quart. J. Roy. Meteor. Soc.*, **83**, 303–314.

Hane, C. E., 1973: The squall line thunderstorm: Numerical experimentation. *J. Atmos. Sci.*, **30**, 1672–1690.

Hauf, T., 1993: Aircraft observation of convection waves over southern Germany—a case study. *Mon. Wea. Rev.*, **121**, 3282–3290.

Hauser, D., and P. Amayenc, 1986: Retrieval of cloud water and water vapor contents from Doppler radar data in a tropical squall line. *J. Atmos. Sci.*, **43**, 823–838.

Heymsfield, G. M., and S. Schotz, 1985: Structure and evolution of a severe squall line over Oklahoma. *Mon. Wea. Rev.*, **113**, 1563–1589.

Holton, J. R., 1992: *An Introduction to Dynamic Meteorology*, Academic Press, 3rd ed, 507 pp.

Houze, R. A., Jr., 1977: Structure and dynamics of a tropical squall line system. *Mon. Wea. Rev.*, **105**, 1540–1567.

———, 1982: Cloud clusters and large-scale vertical motions in the tropics. *J. Meteor. Soc. Jap.*, **60**, 396–410.

———, 1989: Observed structure of mesoscale convective systems and implications for large-scale heating. *Quart. J. Roy. Meteor. Soc.*, **115**, 425–461.

———, 1993: *Cloud Dynamics*. Academic Press, 573 pp.

———, and E. N. Rappaport, 1984: Air motions and precipitation structure of an early summer squall line over the eastern tropical Atlantic. *J. Atmos. Sci.*, **41**, 553–574.

———, B. F. Smull and P. Dodge, 1990: Mesoscale organization of springtime rainstorms in Oklahoma. *Mon. Wea. Rev.*, **118**, 613-654.

————, S. A. Rutledge, M. I. Biggerstaff, and B. F. Smull, 1989: Interpretation of Doppler weather radar displays of midlatitude mesoscale convective systems. *Bull. Amer. Meteor. Soc.*, **70**, 608–619.

Johnson, R. H., and P. J. Hamilton, 1988: The relationship of surface pressure features to the precipitation and airflow structure of an intense midlatitude squall line. *Mon. Wea. Rev.*, **116**, 1444–1472.

————, W. A. Gallus, and M. D. Vescio, 1990: Near-tropopause vertical motions within the trailing stratiform region of a midlatitude squall lines. *J. Atmos. Sci.*, **47**, 2200–2210.

Klemp, J. B., and R. B. Wilhelmson, 1978: The simulation of three-dimensional convective storm dynamics. *J. Atmos. Sci.*, **35**, 1070–1096.

Kuettner, J. P., P. A. Hilderbrand, and T. L. Clark, 1987: Convection waves: Observations of gravity wave systems over convectively active boundary layers. *Quart. J. Roy. Meteor. Soc.*, **113**, 445–467.

Lafore, J.-P., and M. W. Moncrieff, 1989: A numerical investigation of the organization and interaction of the convective and stratiform regions of tropical squall lines. *J. Atmos. Sci.*, **46**, 521–544.

Leary, C. A., and R. A. Houze, Jr., 1979: Melting and evaporation of hydrometeors in precipitation from anvil clouds of deep tropical convection. *J. Atmos. Sci.*, **36**, 669–679.

————, and ————, 1980: The contribution of mesoscale motions to the mass and heat fluxes on an intense tropical convective system. *J. Atmos. Sci.*, **37**, 784–796.

LeMone, M. A., 1983: Momentum flux by a line of cumulonimbus. *J. Atmos. Sci.*, **40**, 1815-1834.

————, and M. W. Moncrieff, 1994: Momentum and mass transport by convective bands: Comparisons of highly idealized dynamical models to observations. *J. Atmos. Sci.*, **51**, 281–305.

————, G. M. Barnes and E. J. Zipser, 1984: Momentum flux by lines of cumulonimbus over tropic oceans. *J. Atmos. Sci.*, **40**, 1815-1834.

Ligda, M. G. H., 1956: The radar observations of mature prefrontal squall lines in the midwestern United States. *VI Congress of Organisation Scientifique et Technique Internationale du Vol a Volie (OSTIV)*, St-Yan, France, 6-14 July, Publication IV.

Lighthill, J., 1978: *Waves in Fluid.* Cambridge University Press, 504 pp.

Lin, Y. L., R. D. Farley, and H. D. Orville, 1983: Bulk parameterization of the snow field in a cloud model. *J. Climate Appl. Meteor.*, **22**, 1066–1092.

Lindzen, R. S., 1974: Wave-CISK in the tropics. *J. Atmos. Sci.*, **31**, 156–179.

————, and H.-L. Kuo, 1969: A reliable method for the numerical integration of a large class of ordinary and partial differential equations. *Mon. Wea. Rev.*, **97**, 732–734.

————, and K.-K. Tung, 1976: Banded convective activity and ducted gravity waves. *Mon. Wea. Rev.*, **104**, 1602-1617.

Ludlam, F. H., 1963: Severe local storms: a review. *Meteor. Monogr.*, **5**, American Meteorological Society, Boston, 1-30.

Marwitz, J. D., 1972: The structure and motion of severe hailstorms. Part II: Multicell storms. *J. Appl. Meteor.*, **11**, 180–188.

Moncrieff, M. W., 1981: A theory of organized steady convection and its transport properties. *Quart. J. Roy. Meteor. Soc.*, **107**, 29-50.

————, 1992: Organised mesoscale convective systems: archetypal dynamical models, mass and momentum flux theory, and parameterization. *Quart. J. Roy. Meteor. Soc.*, **118**, 819-850.

————, and M. J. Miller, 1976: The dynamics and simulation of tropical cumulonimbus and squall lines. *Quart. J. Roy. Meteor. Soc.*, **102**, 373–394.

Newton, C. W., 1950: Structure and mechanisms of the prefrontal squall line. *J. Meteor.* **7**, 210–222.

————, 1963: Dynamics of severe convective storms. In *Severe Local Storms*, Meteor. Monogr., **5**, American Meteorological Society, Boston, 33–58.

————, and J. C. Fankhauser, 1975: Movement and propagation of multicellular convective storms. *Pure Appl. Geophys.*, **113**, 747–764.

Nicholls, M. E., 1987: A comparison of the results of a two-dimensional numerical simulation of a tropical squall line with observations. *Mon. Wea. Rev.*, **115**, 3055–3077.

————, and M. J. Weissbluth, 1988: A comparison of two-dimensional and quasi-three-dimensional simulation of a tropical squall line. *Mon. Wea. Rev.*, **116**, 2437–2452.

————, R. H. Johnson, and W. R. Cotton, 1988: The sensitivity of two-dimensional simulations of tropical squall lines to environmental profiles. *J. Atmos. Sci.*, **45**, 3625–3649.

Ogura, Y., and M. T. Liou, 1980: The structure of a midlatitude squall line. *J. Atmos. Sci.*, **37**, 553–567.

Orlanski, I., 1975: A rational subdivision of scales for atmospheric processes. *Bull. Amer. Meteor. Soc.*, **56**, 527–530.

Pedgley, D. E., 1962: A meso-synoptic analysis of the thunderstorms on 28 August 1958. *Brit. Meteor. Off., Geophy. Mem.*, **106**, 74 pp.

Potter, B. E., 1991: Improvement to a commonly used cloud microphysical bulk parameterization. *J. Appl. Meteor.*, **30**, 1040-1042.

Powers, J. G., 1994: *Numerical model investigations of mesoscale gravity waves.* Ph.D. dissertation, University of Washington, 268 pp.

Priestly, C. H. B., 1949: Heat transport and zonal stress between latitudes. *Quart. J. Roy. Meteor. Soc.*, **75**, 28–40.

Redelsperger, J.-L., and J.-P. Lafore, 1988: A three-dimensional simulation of a tropical squall line: convective organization and thermodynamic vertical transport. *J. Atmos. Sci.*, **45**, 1334–1356.

Rotunno, R., J. B. Klemp, and M. L. Weisman, 1988: A theory for strong, long-lived squall lines. *J. Atmos. Sci.*, **45**, 463–485.

Roux, F., 1988: The West African squall line observed on 23 June 1981 during COPT 81: Kinematic and thermodynamics of the convective region. *J. Atmos. Sci.*, **45**, 406–426.

———, J. Testud, M. Payen, and B. Pinty, 1984: West African squall line thermodynamic structure retrieved from dual-Doppler radar observations. *J. Atmos. Soc.*, **41**, 3104–3121.

Rutledge, S. A., and R. A. Houze, Jr., 1987: A diagnostic modeling study of the trailing stratiform region of a midlatitude squall line. *J. Atmos. Sci.*, **44**, 2640–2656.

———, ———, M. I. Biggerstaff, and T. Matejka, 1988: The Oklahoma-Kansas mesoscale convective system of 10-11 June 1985: Precipitation structure and single-Doppler radar analysis. *Mon. Wea. Rev.*, **116**, 1409–1430.

Sanders, F., and K. A. Emanuel, 1977: The momentum budget and temperature evolution of a mesoscale convective system. *J. Atmos. Sci.*, **34**, 322–330.

Sawyer, J. S., 1960: Numerical calculation of the displacements of a stratified airstream crossing a ridge of small height. *Quart. J. Roy. Meteor. Soc.*, **86**, 326-345.

Schlesinger, R. E., 1973: A numerical model of deep moist convection: Part (I): Comparative experiments for variable ambient moisture and wind shear. *J. Atmos. Sci.*, **30**, 835–856.

Schneider, E. K., and R. S. Lindzen, 1976: A discussion of the parameterization of momentum exchange by cumulus convection. *J. Geophys. Res.*, **81**, 3158-3161.

Scorer, R. S., 1949: Theory of waves in the lee of mountains. *Quart. J. Roy. Meteor. Soc.*, **75**, 41–56.

Skamarock, W. C., M. L. Weisman, and J. B. Klemp, 1994: Three-dimensional evolution of simulated long-lived squall lines. *J. Atmos. Sci.*, **51**, 2563–2584.

Smull, B. F., and R. A. Houze, 1985: A midlatitude squall line with a trailing region of stratiform rain: radar and satellite observations. *Mon. Wea. Rev.*, **113**, 117–133.

——, and ——, 1987a: Dual-Doppler radar analysis of a midlatitude squall line with a trailing region of stratiform rain. *J. Atmos. Sci.*, **44**, 2128–2148.

——, and ——, 1987b: Rear inflow in squall lines with trailing stratiform precipitation. *Mon. Wea. Rev.*, **115**, 2869–2889.

Srivastava, R. C., T. J. Matejka, and T. J. Lorello, 1986: Doppler radar study of the trailing anvil region associated with a squall line. *J. Atmos. Sci.*, **43**, 356–377.

Stevens, D. E., R. S. Lindzen and L. J. Shapiro, 1977: A new model of tropical waves incorporating momentum mixing by cumulus convection. *Dyn. Atmos. Oceans.*, **1**, 365-425.

Szeto, K. K., and H.-R. Cho, 1994: A numerical investigation of squall lines. Part II: The mechanics of evolution. *J. Atmos. Sci.*, **51**, 425–433.

Takeda, T., 1971: Numerical simulation of a precipitating convective cloud: The formation of a "long-lasting" cloud: *J. Atmos. Sci.*, **28**, 350–376.

Tao, W.-K., and J. Simpson, 1989: Modeling study of a tropical squall-type convective line. *J. Atmos. Sci.*, **46**, 177–202.

——, ——, and S.-T. Soong, 1991: A numerical study of a squall line over the Taiwan Strait during TAMEX IOP 2. *Mon. Wea. Rev.*, **119**, 2699–2723.

——, ——, C.-H. Sui, B. Ferrier, S. Lang, J. Scale, M. D. Chou, and K. Pickering, 1993: Heating, moisture and water budgets of tropical and midlatitude squall lines: Comparisons and sensitivity to longwave radiation. *J. Atmos. Sci.*, **50**, 673–690.

——, J. R. Scala, B. Ferrier, and J. Simpson, 1995: The effects of melting processes on the development of squall lines in the tropics and midlatitudes. *J. Atmos. Sci.*, **52**, 1934–1948.

Thorpe, A. J., M. J. Miller, and M. W. Moncrieff, 1982: Two-dimensional convection in non-constant shear: A model for mid-latitude squall lines. *Quart. J. Roy. Meteor. Soc.*, **108**, 739–762.

Weisman, M. L., 1992: The role of convectively generated rear-inflow jets in the evolution of long-lived mesoconvective systems. *J. Atmos. Sci.*, **49**, 799–814.

——, and J. B. Klemp, 1982: The dependence of numerically simulated convective storms on wind shear and buoyancy. *Mon. Wea. Rev.*, **110**, 504–520.

——, and ——, 1984: The structure and classification of numerically simulated convective storms in directionally varying wind shears. *Mon. Wea. Rev.*, **112**, 2479–2498.

———, and ———, 1986: Characteristics of convective storms. *Mesoscale Meteorology and Forecasting* (P. S. Ray, Ed.), American Meteorological Society, Boston, 331–358.

———, and ———, and R. Rotunno, 1988: Structure and evolution of numerically simulated squall lines. *J. Atmos. Sci.*, **45**, 1990–2013.

Wilhelmson, R. B., and Y. Ogura, 1972: The pressure perturbation and the numerical modeling of a cloud. *J. Atmos. Sci.*, **29**, 1295–1307.

———, C.-S. Chen, 1982: A simulation of the development of successive cells along a cold outflow boundary. *J. Atmos. Sci.*, **39**, 1466–1483.

Yang, M.-J., and R. A. Houze, Jr., 1992: A numerical study of the momentum budget of a squall line. *Preprints, 11th International Conf. on Clouds and Precipitation*, Montreal, Canada, Amer. Meteor. Soc., 719–722.

———, and ———, 1995a: Multicell squall line structure as a manifestation of vertically trapped gravity waves. *Mon. Wea. Rev.*, **123**, 641–661.

———, and ———, 1995b: Sensitivity of squall-line rear inflow to ice microphysics and environmental humidity. *Mon. Wea. Rev.*, in press.

———, and ———, 1995c: Momentum budget of a midlatitude squall-line as indicated by a high-resolution numerical model. *J. Atmos. Sci.*, submitted.

Yoshizaki, M., 1986: Numerical simulations of tropical squall-line clusters: Two-dimensional model. *J. Meteor. Soc. Japan*, **64**, 469–491.

Zhang, D.-L., and K. Gao, 1989: Numerical simulation of an intense squall line during the 10-11 June 1985 PRE-STORM. Part II. Rear inflow, surface wake lows and stratiform precipitation. *Mon. Wea. Rev.*, **117**, 2067–2094.

———, ———, and D. B. Parsons, 1989: Numerical simulation of an intense squall line during the 10-11 June 1985 PRE-STORM. Part I. Model verification. *Mon. Wea. Rev.*, **117**, 960–994.

Zipser, E. J., 1969: The role of organized unsaturated convective downdrafts in the structure and rapid decay of an equatorial disturbance. *J. Appl. Meteor.*, **8**, 799 814.

———, 1977: Mesoscale and convective-scale downdrafts as distinct components of squall-line circulation. *Mon. Wea. Rev.*, **105**, 1568-1589.

APPENDIX

DERIVATION OF THE GOVERNING EQUATION (2.13)

In order to simplify the mathematical expression, we use a subscript x as a partial differentiation with respect to x, i.e., $\frac{\partial}{\partial x}(\ ) \rightarrow (\ )_x$, and also use this short-hand notation T such that $\frac{\partial}{\partial T}(\ ) = (\frac{\partial}{\partial t} + \overline{U}\frac{\partial}{\partial x})(\ ) \rightarrow (\ )_T$. Subtracting $(\frac{\partial}{\partial z} + \Gamma)(2.7)$ from $\frac{\partial}{\partial x}(2.8)$, we can eliminate $\tilde{\pi}$ between (2.7) and (2.8).

$$\tilde{w}_{xT} - \tilde{\theta}_x - \tilde{u}_{zT} - \tilde{w}_z\overline{U}_z - \tilde{w}\overline{U}_{zz} - \Gamma\tilde{u}_T - \Gamma\tilde{w}\overline{U}_z = 0 \tag{A1}$$

Adding $\frac{\partial}{\partial x}(2.9)$ to $\frac{\partial}{\partial T}(A1)$, we can eliminate $\tilde{\theta}$.

$$\tilde{w}_{TxT} - \tilde{u}_{TzT} - (\tilde{w}_{Tz} + \Gamma\tilde{w}_T)\overline{U}_z - \tilde{w}_T\overline{U}_{zz} - \Gamma\tilde{u}_{TT} + N^2\tilde{w}_x - \tilde{Q}_x = 0 \tag{A2}$$

Taking $\frac{\partial}{\partial x}(A2)$, we can eliminate $\tilde{u}$ with the aid of (2.12) to yield a single equation for $\tilde{w}$.

$$\tilde{w}_{TTxx} + \tilde{w}_{TTzz} - \tilde{w}_{Tx}\overline{U}_{zz} - (\Gamma^2 + \Gamma_z)\tilde{w}_{TT} - 2\Gamma\overline{U}_z\tilde{w}_{Tx} + N^2\tilde{w}_{xx} - \tilde{Q}_{xx} = 0 \tag{A3}$$

(A3) is the same as (2.13) after converting short-hand notations to their original mathematical expressions.

VITA

Ming-Jen Yang was born 7 July 1964 in Taipei, Taiwan. From 1982 to 1986, he attended National Taiwan University, where he received a B.S. in Atmospheric Sciences, and had the highest 4-year-averaged GPA for undergraduate major in atmospheric sciences (still holding the record now). From 1986 and 1988, he joined the Taiwanese Air Force to perform his mandatory military service as a weather officer. In October 1988, he was awarded an overseas graduate fellowship from the Ministry of Education of Taiwan government. In September 1989, he entered the graduate program in Atmospheric Sciences at the University of Washington. In July 1990, he married to Kuan-Mei Lu. On July 31, 1995, his son, Eric Yang, was born in Seattle. After finishing his Ph.D. in August 1995, he will continue to work in Atmospheric Sciences Department at the University of Washington as a Post-doctoral Research Associate.

PUBLICATIONS

1992

Yang, M.-J. and R. A. Houze, Jr., 1992a: A three-dimensional simulation of the 28 June 1989 storm in the North Dakota Thunderstorm Project. *The Third International Workshop of Cloud Modeling*, Toronto, Canada, World Meteorological Organization.

Yang, M.-J. and R. A. Houze, Jr., 1992b: A numerical study of the momentum budget of a squall line. *Preprints, 11th International Conf. on Clouds and Precipitation*, Montreal, Canada, Amer. Meteor. Soc., 719-722.

1993

Durran, D. R., M.-J. Yang, D. N. Slinn and R. G. Brown, 1993: Toward more accurate wave-permeable boundary conditions, *Mon. Wea. Rev.*, **121**, 604-620.

1994

Yang, M.-J., and R. A. Houze, Jr., 1994: Multicell squall line structure as a manifestation of vertically trapped gravity waves. *Preprints, Sixth Conference on Mesoscale Processes*, Portland, Amer. Meteor. Soc., 619–622.

1995

Yang, M.-J., and R. A. Houze, Jr., 1995a: Multicell squall line structure as a manifestation of vertically trapped gravity waves. *Mon. Wea. Rev.*, **123**, 641-661.

Yang, M.-J., and R. A. Houze, Jr., 1995b: Sensitivity of squall-line rear inflow to ice microphysics and environmental humidity. *Mon. Wea. Rev.*, accepted.

Braun, S. A., R. A. Houze, Jr., and M.-J. Yang, 1995: Comments on "The impact of the ice phase and radiation on a midlatitude squall line system." *J. Atmos. Sci.*, conditionally accepted.

Yang, M.-J., and R. A. Houze, Jr., 1995c: Momentum budget of a midlatitude squall line as indicated by a high-resolution numerical mode. *J. Atmos. Sci.*, submitted.